Universitetet
i Stavanger

**FACULTY OF SCIENCE AND TECHNOLOGY**

# MASTER'S THESIS

| | |
|---|---|
| Study programme/specialisation:<br>Master of Science in Petroleum Engineering - Reservoir Engineering | Spring semester, 2017<br><br>Open/~~Restricted~~ |
| Author: Eirik Brødremoen Lund | …………………………………………<br>(signature of author) |
| Programme coordinator: Professor II Leif Larsen, UiS<br><br>Supervisor: Senior Research Engineer Anton Shchipanov, IRIS | |
| Title of master's thesis:<br><br>Evaluating Flowing Conditions of Faults and Fractures from Well Testing and Interpretation: A Study Based on Reservoir Simulation | |
| Credits: 30 ECTS | |
| Keywords: PTA, Stress-dependent permeability, reservoir simulation, dynamic reservoir, dynamic fault, reservoir simulation, geomechanics | Number of pages: 60<br><br>+ supplemental material/other: 28<br><br>Stavanger, June 15$^{th}$/2017<br>date/year |

Title page for Master's Thesis
Faculty of Science and Technology

# Evaluating Flowing Conditions of Faults and Fractures from Well Testing and Interpretation: A Study Based on Reservoir Simulation

By

**Eirik Brødremoen Lund**

Thesis submitted in fulfilment of
the requirements for the degree of
Master of Science
(MSc)

Supervisors:

Senior Research Engineer
Anton Shchipanov

Professor II
Leif Larsen

International Research Institute of Stavanger

The University of Stavanger,
Faculty of Science and Technology

FACULTY OF SCIENCE AND TECHNOLOGY
DEPARTMENT OF PETROLEUM ENGINEERING
2017

## Summary

The scope of the thesis was inspired by the studies of $CO_2$ storage in saline aquifers containing faults conducted at IRIS within the ENOS project[1]. In storage site evaluations, assessing and preventing leakage from the injection site is a necessary component. Many saline aquifers contain faults, which can act as sealing boundaries or as reservoir fluid conductors if reactivated, e.g. due to $CO_2$ injection and reservoir pressure buildup. Evaluation and monitoring of flowing conditions on faults are therefore crucial for preventing or limiting $CO_2$ leakage from injection sites.

Fluid production and injection in porous rocks cause changes of pore pressure and in-situ effective stresses, having an impact on rock permeability and reservoir features like faults and fractures. In reservoir simulation, such dynamic reservoir behaviour may be addressed via introducing stress-dependent functions for permeability and fault and fracture conductivities. In general, a coupling between reservoir flow simulators and geomechanical modelling is necessary to address the changes of the pore pressure and the effective stresses interconnected via stress-dependent reservoir properties. However, such a coupling is time-consuming, so the conventional approach is to assume these properties to be pressure-dependent and ignore total reservoir stress change. Using analytical geomechanics to relate effective stress changes to pressure changes may work as an alternative approximation located between the extreme approaches described above.

The first part of the thesis focuses on the comparison of different models to account for geomechanical effects based on the uniaxial strain approximation relating pressure and stress changes. This results in different pressure functions: (1) ignoring total stress changes, and accounting for (2) local and (3) global stress changes. Conventional uncoupled reservoir simulators have functionality for implementing the models (1) and (2), but cannot cover the model (3). A research code for simulating 1D radial single-phase flow with stress-dependent permeability and all three models implemented has been developed in MS Excel VBA and tested via comparison with the Eclipse simulator for the models (1) and (2). Using the code, all three models have been compared for different boundary conditions showing what applying the models (1) and (2) give upper and lower limits for stress and permeability forecasts, while the model (3) forecast is located in between. This argues that using the models (1) and (2) in reservoir simulations can help to cover the whole uncertainty range for effects related to geomechanics at given geomechanical parameters and under the assumptions mentioned above.

A single well water injection into a saline aquifer near a fault was numerically simulated and studied in the second part of the thesis. The study employed a combination of analytical and numerical simulations in Saphir and Eclipse. A possibility of detecting fault reactivation from interpreting well injection and shut-in pressure transients has been confirmed. Here, reactivation of initially sealing fault (with zero permeability along and across the fault) was related with intensive reversible growth of permeability along the fault after a threshold pressure. Pressure

Transient Analysis (PTA) of simulated pressure responses has illustrated the possibility to detect fault reactivation from both injection and shut-in responses, whilst the combination of interpreting both responses gives the most reliable detection. It was also observed in the simulations that the intensity of permeability increase along the fault seems to have a minor impact on the pressure derivative for chosen fault orientation with respect to the well. Therefore, monitoring pressure transient response during injection in site operations can give a good indication of fault reactivation. A comparison of two cases with fault reactivation by the models (1) and (2) applied to a fault permeability function (e.g. evaluated from laboratory experiments) has illustrated a possible uncertainty range related with to description of geomechanical effects in reservoir simulations.

The results of this thesis will be used in further activities within the framework of the ENOS project[1] at IRIS. The results of this reservoir simulation study and outcomes of PTA for faulted reservoirs would help in the development of a PTA-based methodology for the monitoring of dynamic fault behaviour at pilot injection sites around Europe.

[1] ENOS (Enabling Onshore $CO_2$ Storage). The project is funded by the European Union's Horizon 2020 research and innovation programme under grant agreement No. 653718. www.enos-project.eu

## Acknowledgements

I would like to thank my supervisor Senior Research Engineer Anton Shchipanov at IRIS, for suggesting this topic of investigation of the present thesis. His patience, knowledge, and support are greatly appreciated.

I would also like to thank my supervisor Professor II Leif Larsen at the University of Stavanger for great assistance and advice.

Finally, I would like to thank my fellow students for fruitful discussions throughout our studies in Stavanger and Adelaide.

# Contents

## List of figures

## List of tables

# 1 Introduction

Traditionally, reservoir engineering has related to the production of hydrocarbon and groundwater hydrology. This area now has new applications with the entry of Geological Carbon Storage (GCS), which includes, among others, the storage of $CO_2$ in saline aquifers.

Many of these saline aquifer systems contain large- and/or small-scale faults, which may act as sealing boundaries. Reactivation of these faults by fluid injection or extraction, which changes the geomechanical stress-state, may impair the structural integrity of the aquifer system and cause fluid-seep to overlying formations or to the surface. Monitoring the dynamic reservoir behaviour is therefore key to ensure structural integrity and safe $CO_2$ storage and -EOR.

Much research has been done in the field of dynamic fault behaviour and induced seismicity during fluid injection (Kim, 2013; Kulikowski, Amrouch, & Cooke, 2016; Majer et al., 2007; Mazzoldi, Rinaldi, Borgia, & Rutqvist, 2012; Rutqvist, Cappa, Rinaldi, & Godano, 2014a, 2014b), although little has been done regarding its effect on pressure transient response and Pressure Transient Analysis (PTA). The results of this thesis will, therefore, help in the monitoring of dynamic fault behaviour during fluid injection utilising Pressure Transient Analysis (PTA)

## 1.1 Objectives

The present study employs a combination of analytical and numerical simulation models for Pressure Transient Analysis (PTA) for evaluation and characterisation of pressure (or in a more general sense, stress-) sensitive and dynamic reservoirs. The primary objectives of the study are:

- Assembling synthetic segment reservoir models with and without faults and simulating fluid flow and well tests
- Studying sensitivity of pressure transient responses to pressure- (stress-) dependent properties of the matrix and the fault
- Analysing the effect of stress-dependent permeability of the matrix and dynamic fault behaviour on pressure transient response

## 1.2 Scope

Following the set objectives of this thesis, the study is divided into the following tasks:

1. Building a 1D, radial, single-phase reservoir flow research code using MS Excel VBA, with availability to account for changing total stress, and stress-dependent permeability assuming uniaxial deformation
2. Setting up a single well reservoir model, containing a dynamic fault using Schlumberger Eclipse E100 reservoir flow simulator
3. Analysis of pressure transient behaviour controlled by pressure- and stress-sensitive permeability and dynamic fault behaviour

# 2 Theory

This chapter explains some of the necessary theoretical background for this work. It starts with basic subjects regarding PTA, like the pressure diffusivity equation, different types of well tests, different flow regimes and briefly talks about analysis of pressure transient response. It then moves on to briefly discuss fractured and faulted reservoirs and finally explains some concepts regarding geomechanics. These last sections include both basic geomechanical considerations, the effective stress concept, fault reactivation, stress-dependent permeability, dynamic reservoir behaviour and finally talks about PTA for stress-sensitive and dynamic reservoirs. This to give some background info relevant to the work done in Chapters 3 and 4.

## 2.1 Flow in porous media

The main controlling equation for flow in porous media is the radial diffusivity equation, (2.1).

$$\frac{1}{r}\frac{\partial}{\partial r}\left(r\frac{\partial P}{\partial r}\right)=\frac{\varphi\mu c}{k}\frac{\partial P}{\partial t} \tag{2.1}$$

This equation assumes constant permeability, fully penetrating well, homogeneous and isotropic media, among others (Bourdet, 2002; Horne, 1995). For practical purposes of well test interpretation, it is not necessary to understand the process of solution of the pressure diffusivity equation. Solutions of the diffusivity equation have been developed for a variety of reservoir configurations (Horne, 1995).

## 2.2 Types of well tests

### *2.2.1 Drawdown and buildup testing*

The ideal drawdown test is started from an initially static, stable, and shut-in well. The well is opened to flow, preferably at a constant rate, and the downhole wellbore pressure is measured as the transient propagates through the reservoir.

The drawdown test is normally followed by a buildup test. After ideally obtaining a constant production rate, the well is shut either by using a downhole shut-in tool or shutting the well head. As the wellbore pressure increases, it is measured and recorded for further analysis.

### 2.2.2 *Injection and falloff testing*

Injection testing is conceptually the same as a drawdown test. Instead of flow from the reservoir into the well, the flow is directed from the well into the reservoir. An advantage is that injection rates are more easily controlled than production rates, due to multiphase effects and dynamic reservoir behaviour. If the necessary adjustments are made for the direction of flow, the equations established for production wells are also applicable for injecting wells (Samaniego V, Brigham, & Miller, 1977). The falloff test measures the pressure decline at the wellbore following an injection test, i.e. after the well is shut.

### 2.2.3 *Interference and pulse testing*

In interference testing, one well is the active well (either injecting, producing, etc.) and another well, idle and a distance away, observes the pressure response generated by the active well. Since this test monitors pressure changes a distance away from the active well, it can be useful for the characterisation of reservoir properties over a greater distance, i.e. well to well properties (Horne, 1995).

Pulse testing is a part of interference testing. One well produces in short “bursts”, whilst an idle well, some distance away, records the pressure response. The advantage of pulse testing versus regular interference tests is that a series of flow disturbances are produced which gives rise to diagnostic pressure response that can more easily be distinguished from noise (Johnson, Greenkorn, & Woods, 1966).

## 2.3 Flow regimes

There are several main flow regimes encountered during pressure transient testing. The transient flow period is characterised by that the pressure transient migrating outwards from the well is yet to encounter any boundaries. A clear transient period is needed for good estimates of reservoir properties, such as the permeability thickness product (Bourdet, 2002; Horne, 1995).

In an ideal case, under a closed drainage scenario (either constant pressure or closed boundaries) one of two flow regimes may occur. Pseudo-steady state flow occurs when the outer boundaries are closed, and the pressure declines uniformly throughout the reservoir. In the other case, when the outer boundaries are of constant pressure, the static pressure at the boundary does not decline, and the pressure at every point in the reservoir remains constant, i.e. steady state flow (Bourdarot, 1998; Chaudhry, 2004).

## 2.4 Wellbore storage and skin

The early time response of a pressure transient test may be distorted by phenomena such as wellbore storage and skin. Since fluid withdrawal occurs at the wellhead, instead of directly at the sandface, there is a time-lag between the opening of the wellhead and constant mass rate from the formation. The time lag occurs because of compressibility of the fluid in the well, and storage capacity of the wellbore, i.e. wellbore storage (Bourdarot, 1998; V. F. Samaniego & Villalobos, 2003). This effect can be avoided or minimised when using a downhole shut-in tool and -pressure gauges.

In addition, the wellbore region may also be damaged or otherwise perform worse than ideal conditions. This gives rise to a region of higher pressure drop near well, and the concept of damaged zone or skin zone. For the case of stimulated wells, e.g. acid or hydraulic fracture stimulation, this pressure drop is lower than for an unstimulated well (Bourdarot, 1998).

## 2.5 Analysis

For a thorough review of the analysis methods for geological aspects, dual-porosity, -permeability, hydraulically fractured wells, etc., the reader is referred to books by Horne (1995), Bourdarot (1998) and Bourdet (2002).

### *2.5.1 Semi-log analysis*

The slope of the pressure data points during the infinite acting period, IARF, is characteristic of the reservoir, i.e. of its rock properties like permeability. When the pressure transient reaches an unconformity, like a boundary, the trend of the data is characteristic of the type of boundary, i.e. constant pressure, closed or mixed boundary conditions (Bourdet, 2002; Horne, 1995).

### *2.5.2 Log-log analysis*

By matching the pressure transient response, on a log-log scale, with a dimensionless theoretical curve, also known as a type curve, parameters such as skin factor, formation conductivity, and wellbore storage coefficient can be obtained (Bourdet, 2002). These type curves are solutions of the pressure diffusivity equation, mentioned in Section 2.1, that are used to infer unknown reservoir parameters by type curve matching the reservoir pressure response, i.e. inverse problem solving (Horne, 1995).

With the pressure derivative approach to analysis, by employing the natural logarithm, the pressure derivative can be expressed as follows on a log-log plot

$$\Delta P' = \frac{dP}{dln\Delta t} = \Delta t \frac{dP}{d\Delta t} \tag{2.2}$$

This is the so-called “Bourdet Derivative”. One of the major advantages of the pressure derivative response is that it is more sensitive to minor changes in pressure, which is not detected by regular log-log analysis, like minor increase or decrease in wellbore pressure (Bourdet, 2002).

## 2.6 Faulted and fractured reservoirs

Faults are a result of plate tectonics. As the earth's tectonic plates move relative to each other, stress builds in the rock. If this stress exceeds the rock's threshold for strain, the energy that has been building up in the rock body is released and focused along a specific plane (Skinner, Porter, & Park, 2004):

Based on the fault movement, the type of fault can be categorised into three groups (Skinner et al., 2004):

a) Normal faults: Occur generally in places where the lithosphere is stretched, therefore they are a major structural part of sedimentary rift basins. Most of the active normal faults dip at steeper angles than 50°
b) Strike-slip faults: Mainly horizontal offset, and very little vertical offset. A special type of strike-slip faults are transform faults, where these faults form plate boundaries
c) Thrust faults: These are reverse faults, and frequently dominate collision mountain belt structures. Normally of low dip angles

The different fault movements are shown in Figure 2.1 below:

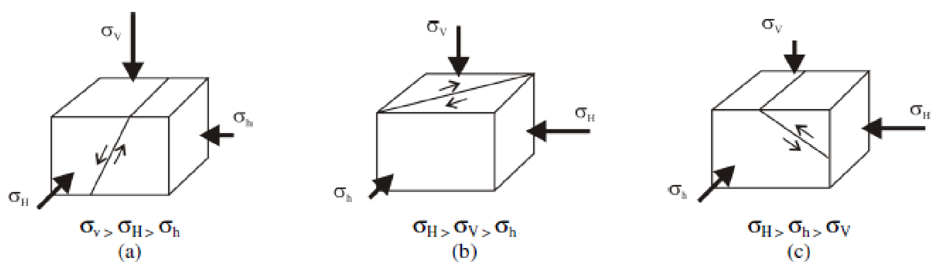


*Figure 2.1 Andersons fault scheme. a) Normal fault, b) Strike-slip fault, c) Thrust fault. From Nacht, De Oliveira, Roehla, & Costa (2010)*

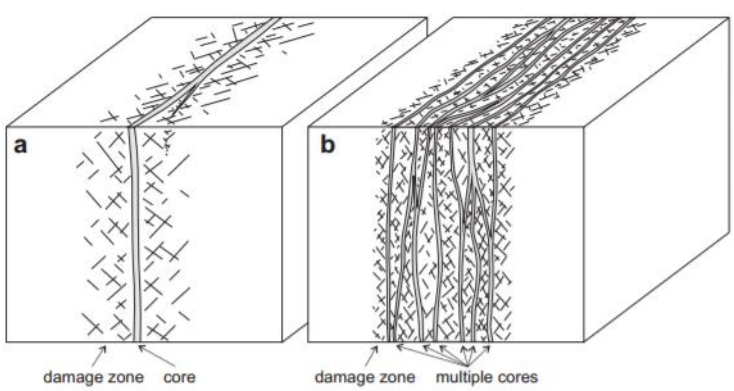


*Figure 2.2 Faulted Rock body a) single fault core b) multiple fault cores. From Faulkner et al. (2010).*

Faults generally consist of three zones; one or more principal stress zones, located within a fault core which are surrounded by a zone of fractures, and faults (damaged zone) (Shipton, Soden, Kirkpatrick, Bright, & Lunn, 2006) as shown in Figure 2.2.

The damaged zone around large faults represents the accommodation of strain. It is the product of fault propagation, displacement and linking processes operating over the lifetime of a fault zone. The damaged zone usually consists of fractures with widely different lengths and other subsidiary faults (Faulkner et al., 2010). Its size is dependent on several parameters such as lithology, deformation conditions and strain distribution between the footwall and hanging wall (Knipe, Jones, & Fisher, 1998).

Every geological formation is fractured to some extent because of stress triggered by the overburden, fluid pressure, tectonic forces, etc. Faults and fractures can act as both conduits for hydrocarbon migration and create traps and barriers. Therefore, these have a significant effect on reservoir performance and behaviour (Committee on Fracture Characterization and Fluid Flow, 1996; Pei, Paton, Knipe, & Wu, 2015). Fractures occur at a broad range of size, from microscopic to continental fractures (Kuchuk, Biryukov, & Fitzpatrick, 2015).

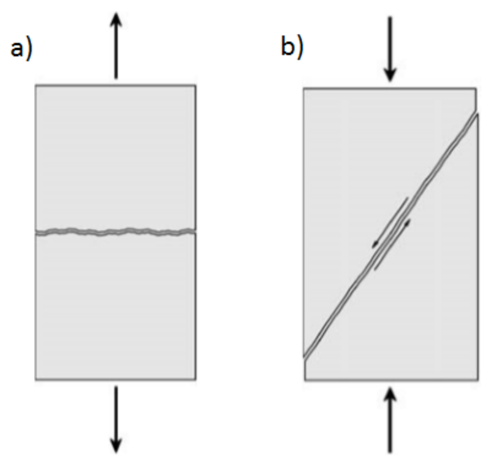


*Figure 2.3 a) Tensile failure, b) Shear failure. From Fjær, Holt, Raaen, Risnes, & Horsrud (2008).*

Fractures are similar to faults, as a discontinuity in the rock media. Whilst faults are the result of shear failure, fractures are a result of tensile failure. Tensile failure takes place when the effective tensile stress exceeds the tensile strength of the sample. The tensile strength is the critical limit of tensile stress along some plane in the sample (Fjær et al., 2008). Tensile and shear failure are illustrated in Figure 2.3 a) and b).

## 2.7 Geomechanics and stress sensitive formation

It has long been recognised that porous media are not always non-deformable and rigid (F. Samaniego & Cinco-Ley; Samaniego V et al., 1977; Zhang & Ambastha, 1994). Basic geomechanical aspects, dynamic reservoirs and the challenges this gives for PTA are discussed in the following sections.

### *2.7.1 Basic geomechanics*

The three-dimensional (x,y,z) stress-state of any material can be described by a 3x3 stress tensor, consisting of three normal stress and six shear stress components, $\sigma$ and $\tau$ respectively.

$$\begin{pmatrix} \sigma_x & \tau_{xy} & \tau_{xz} \\ \tau_{yx} & \sigma_y & \tau_{yz} \\ \tau_{zx} & \tau_{zy} & \sigma_z \end{pmatrix}_R \tag{2.3}$$

The expression above, Equation (2.3), gives a complete description of the stress state at the arbitrary point R. Through symmetry, the number of independent components in the tensor can be reduced to six, where $\tau_{xy} = \tau_{yx}, \tau_{xz} = \tau_{zx}$ and $\tau_{zy} = \tau_{yz}$ (Fjær et al., 2008), which results in the stress tensor (2.3), when assuming no rotational forces, becoming:

$$\begin{pmatrix} \sigma_x & \tau_{xy} & \tau_{xz} \\ \tau_{xy} & \sigma_y & \tau_{yz} \\ \tau_{xz} & \tau_{yz} & \sigma_z \end{pmatrix}_R \tag{2.4}$$

The coordinate system can be oriented in such a way that the x- and y-axes are parallel to the first and second principal axes, which gives rise to Mohr's circle (Fjær et al., 2008). Mohr's circle describes the stress-state at any point P by the Equations (2.5) and (2.6).

$$\sigma = \frac{1}{2}(\sigma_1 + \sigma_2) + \frac{1}{2}(\sigma_1 - \sigma_2)cos2\theta \tag{2.5}$$

$$\tau = -\frac{1}{2}(\sigma_1 - \sigma_2)sin2\theta \tag{2.6}$$

These equations give rise to Figure 2.4 a) below, with $\theta$ and the direction of $\tau$ and $\sigma$ shown in Figure 2.4 b).

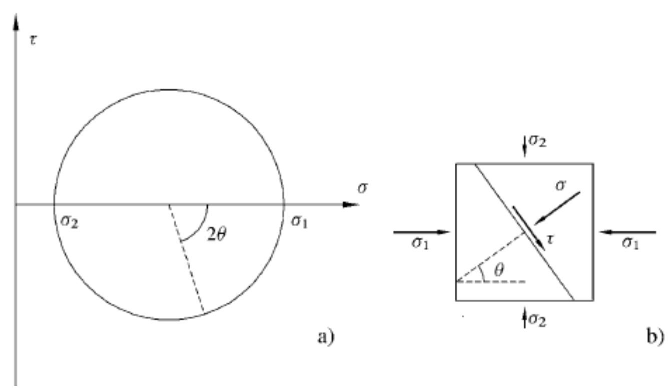


*Figure 2.4 Mohr's circle in two dimensions. From Fjær et al. (2008).*

This concept may be expanded into three dimensions, where a point R having the principle stress tensor given by Equation (2.7):

$$\begin{pmatrix} \sigma_1 & 0 & 0 \\ 0 & \sigma_2 & 0 \\ 0 & 0 & \sigma_3 \end{pmatrix}_R \tag{2.7}$$

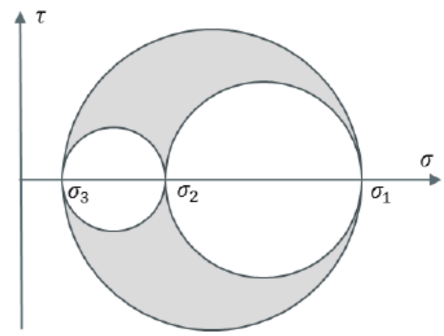


*Figure 2.5 Mohr's circle in three dimensions. From Fjær et al. (2008).*

The stress state is then described by a combination of circles (Fjær et al., 2008) as in Figure 2.5. Any possible stress state at point P is either located at one of the circles' circumferences or the grey area shown.

### *2.7.2 Effective stress concept*

Fluid withdrawal from or fluid injection into the reservoir respectively decreases or increases the pore pressure, and in turn, changes the effective stress. A lowering of pore pressure, and subsequent increase of effective stress, reduces total porosity and permeability. The effective stress abides by Equation (2.8).

$$\sigma' = \sigma - \alpha P_{pore} \tag{2.8}$$

$$\sigma = \frac{1}{3}(\sigma_1 + \sigma_2 + \sigma_3) \tag{2.9}$$

Changing the pore pressure, by depletion or injection of pore fluids, results in the effective stress changing. If the differences between $\sigma_1$, $\sigma_2$ and $\sigma_3$ are unaffected by changes in pore pressure, the area of the circle spanning $\sigma_1$ to $\sigma_3$ does not change, but is moved left or right depending on how the pore pressure changes, Figure 2.6a). Another case is when depletion or injection of fluids in the subsurface changes not only the effective stresses, but also the total stresses (Fjær et al., 2008), i.e. the differences between $\sigma_1$, $\sigma_2$ and $\sigma_3$. In this case, the area encapsulated by the Mohr's circle changes accordingly, Figure 2.6b).

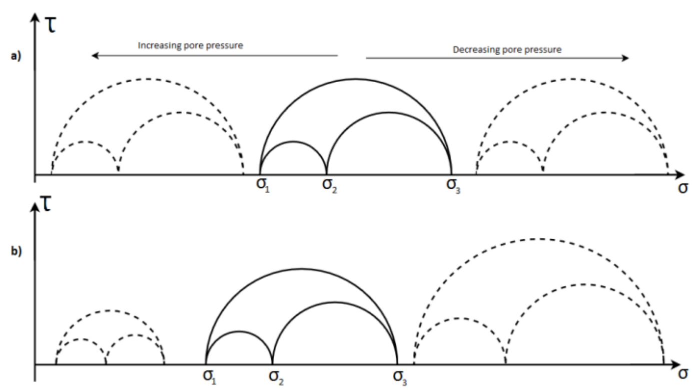


*Figure 2.6 Mohr's circle, changing pore pressure. a) no change in total stresses, b) changing stress state. By Eirik B. Lund from Rutqvist, Birkholzer, Cappa, & Tsang (2007).*

For the implementation of reservoir geomechanics into flow simulation, the correct procedure is coupling with a rock geomechanics model. Settari, Bachman, & Walters (2005) made use of the effective stress formulation to approximate effects of geomechanics in conventional flow simulation, i.e. without geomechanical coupling. Model (1), Section 2.7.2.1, assumes constant mean total stress, whilst the latter two models (2) and (3), Sections 2.7.2.2 and 2.7.2.3 respectively, assume changing total mean stress with respect to changing local or global, i.e. average, reservoir pressure respectively and uniaxial deformation of individual grid blocks.

#### 2.7.2.1 Model (1): Non-correcting model

In this model, it is assumed that the total stress is constant, regardless of reservoir pressure, i.e. $\sigma_m = \sigma_m^0$ and the effective stress is given by

$$\sigma_m' = \sigma_m^0 - \alpha P_{pore} \tag{2.10}$$

$$\sigma_m^0 = \frac{1}{3}(\sigma_1 + \sigma_2 + \sigma_3) \tag{2.11}$$

Reservoir permeability then becomes a function of only local reservoir pressure, $\Delta\sigma_m = 0$ and $k = f(P)$.

#### 2.7.2.2 Model (2): Local correction model

The uniaxial deformation concept can be applied locally if each grid cell deforms independently of the other grid cells. The vertical stress $\sigma_V$ remains constant and the horizontal stresses change by (Settari et al., 2005):

$$\Delta\sigma_h = \Delta\sigma_H = \Delta P\alpha\frac{1-2\nu}{1-\nu} = \Delta P\eta \tag{2.12}$$

If the grid cell pressure changes by $\Delta P$ from $P^0$ to $P$, the effective stress changes from $\sigma_m' = \sigma_m^0 - \alpha P$ to:

$$\sigma_m' = \sigma_m^{0\,\prime} + \frac{2}{3}\eta\Delta P - \alpha P \tag{2.13}$$

This results in the reservoir permeability becoming a function of only local pressure, i.e. $k = f(P)$ with $\Delta\sigma_m = f(\Delta P)$.

#### 2.7.2.3 Model (3): Global correction model

In this model, if the average pressure changes from $P_{avg}^0$ to $P_{avg}$ by the amount of $\Delta P_{avg}$, and the vertical stress $\sigma_V$ remains constant, the horizontal stress changes by Equation (2.14) (Settari et al., 2005):

$$\Delta\sigma_h = \Delta\sigma_H = \Delta P_{avg}\alpha\frac{1-2\nu}{1-\nu} = \Delta P_{avg}\eta \tag{2.14}$$

This is according to uniaxial deformation, i.e. free vertical deformation, whilst horizontal deformation = 0. Then the effective stress changes by Equation (2.15):

$$\sigma_m' = \sigma_m^{0\,\prime} + \frac{2}{3}\eta\Delta P_{avg} - \alpha P_{pore} \tag{2.15}$$

The reservoir permeability becomes a function of local and average pressure, i.e. $k = f(P, P_{avg})$ with $\Delta\sigma_m = f(\Delta P, \Delta P_{avg})$.

### 2.7.3 *Reactivation of faults*

Several authors have investigated the effects which fluid injection into a rock body have on fault reactivation (e.g. (Gan & Elsworth, 2014; Nacht et al., 2010; Rutqvist et al., 2014a, 2014b; Rutqvist, Rinaldi, Cappa, & Moridis, 2013)).

As shown in Figure 2.6, injection (or production) of pore fluids changes the reservoir stress-state, by altering the effective stress, following Equation (2.8). Reactivating flow barriers, such as faults, threatens the structural integrity of the rock body. In the case of injection, fault reactivation may cause fluid-seep to the overlying formation or surface. As the differential stress increases, the shear stress acting on the fault plane may exceed the shear strength of the formation and cause reactivation and fault slippage at a shear stress level where it previously was stable (Nacht et al., 2010; Zoback & Zinke, 2002). This condition may be expressed as a linear Mohr-Coulomb criterion (Choi, Skurtveit, Bohloli, & Grande, 2015) given by Equation (2.16) and shown in Figure 2.7. Figure 2.7 shows a critically stress rock sample, i.e. shear stress, $\tau$, equal to the critical shear stress, $\tau_{crit}$. Any lowering of the effective normal stress, $(\sigma_n - P_{pore})$ would lead to tensile failure or fault reactivation.

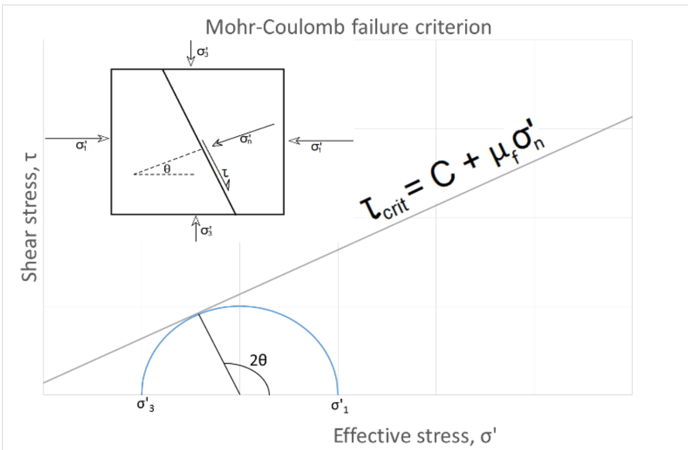


*Figure 2.7 Mohr' circle with failure criterion. By Eirik B. Lund, from Fjær et al. (2008).*

$$\tau_{crit} = C + \mu_f(\sigma_n - P_{pore}) = C + \mu_f \sigma_n' \qquad (2.16)$$

### 2.7.4 *Relevant stress components*

Different aspects of any rock body may be affected by different stress components, either $\sigma_h$, $\sigma_H$ or $\sigma_V$, or a combination of these.

The matrix is generally affected by changing all components of the stress field, i.e. $\sigma_H$, $\sigma_h$ and $\sigma_V$. Its ability to maintain porosity and permeability at changing stress state is affected by the fluid pressure within the pores.

In the rock body, the direction of least mechanical support is the direction of $\sigma_h$. Because of this, fractures generally propagate in the direction normal to $\sigma_h$, i.e. in the direction of $\sigma_H$, and the fracture aperture, permeability and porosity are more affected by the magnitude of the effective minimum horizontal stress, $\sigma_h - P_{pore}$ (Shchipanov, Kollbotn, Surguchev, & Thomas, 2010).

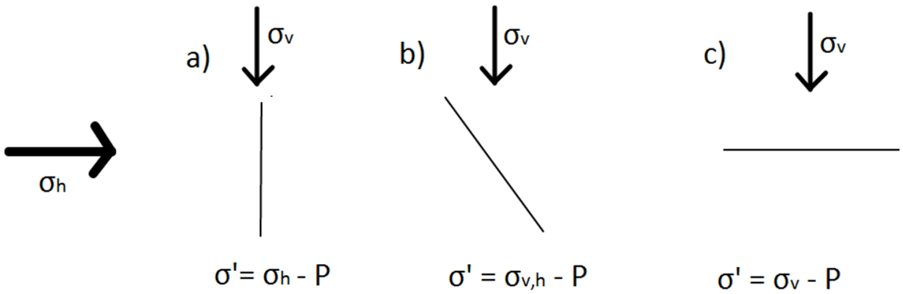


*Figure 2.8 Fault angle vs. relevant stress components. The direction of $\sigma_H$ is normal to $\sigma_h$*

With regards to faults, depending its angle compared to the direction of $\sigma_V$, different stress components may be relevant to the effective stress acting on the fault plane, and fault stability. If the fault plane is parallel to the vertical stress, the effect of $\sigma_V$ is minor compared to the horizontal component. The lower the fault plane angle, compared to the normal plane of $\sigma_V$, the more its properties and stability are governed by changing vertical stress, as shown in Figure 2.8 above. The relevant effective stress then becomes less a function of horizontal stress, and more a function of vertical stress, $\sigma_V$ for increasingly horizontal faults.

#### *2.7.5 Stress-dependent permeability*

Permeability is very sensitive to changes in pore pressure for fractured rock systems and tight formations (Vairogs, Hearn, Dareing, & Rhoades, 1971; Vairogs & Rhoades, 1973). This results in a strongly nonlinear diffusivity equation (Pedrosa, 1986).

A method of accounting for pressure sensitive formation is the pseudo pressure formulation, given in Equation (2.17). It incorporates pressure dependent characteristics, of both fluid and rock formation. This is the approach of Raghavan et al. (1972) and Samaniego et al. (1977) among others.

$$m(P) = \int_{P_m}^{P} \frac{\rho(P)k(P)}{[1-\varphi(P)]\mu(P)} dP \qquad (2.17)$$

Another method of accounting for compressible formation is to define the permeability modulus, $\gamma$. It accounts for the stress-sensitivity of the permeability (Yilmaz, Nur, & Nolen-Hoeksema, 1991) as the compressibilities, $c_r$ and $c_l$, account for stress sensitivity of the porosity, $\varphi$, and the fluid density, $\rho$ (Zhang & Ambastha, 1994), respectively. The correlations between permeability modulus, permeability, pressure and effective stress are shown in Equations (2.18) and (2.19).

$$\gamma = \frac{1}{k}\frac{dk}{dP} \tag{2.18}$$

$$\gamma = -\frac{1}{k}\frac{dk}{d\sigma'} \tag{2.19}$$

These are the correlations used to simulate the cases of stress-dependent matrix permeability and dynamic fault behaviour in this thesis.

### *2.7.6 Dynamic reservoir behaviour in stress sensitive formations*

The problem of including geomechanics in reservoir simulations is caused by several factors (Shchipanov et al., 2010):

i) Lack of input data for geomechanical modelling
ii) Modelling of both reservoir and overburden rocks
iii) Coupling reservoir and geomechanical numerical simulators

Several authors have worked on coupled flow/geomechanics models to tackle fluid flow in deformable formation for dual porosity and fractured systems (Bagheri & Settari, 2005; Bagheri & Settari, 2008 and references therein).

Bagheri and Settari (2005) developed a coupling of fluid flow equations and the deformation of fractured media. Their approach allowed for multiple fractures of any direction (any dip and strike angles), but only parallel to the coordinate axes. The same authors, (Bagheri & Settari, 2008), later considered variable full tensor permeability in their geomechanical model.

### *2.7.7 Pressure Transient Analysis for stress-sensitive reservoirs*

Stress-sensitive permeability changes the nature of the pressure transient response, compared to the response usually observed during PTA for constant permeability systems. It can, however, be interpreted from PTA, because of this major influence on the pressure transients.

The presence of such stress-sensitive permeability can be determined by the following nature of the pressure transient response (Adams, 1983; Ostensen, 1986; Pinzon, Chen, & Teufel, 2001; Shchipanov, Kollbotn, Berenblyum, & Surguchev, 2011; Shchipanov et al., 2010 and references therein):

i) Lack of infinite acting radial flow regime
ii) Time and rate dependent logarithmic derivatives of pressure transients
iii) Inconsistent results between drawdown and buildup, or injection and falloff tests
iv) Unusual value of skin
v) Rate-sensitive skin

During pressure transient testing of stress-sensitive formation, the key is to understand the effect of the stress-dependent permeability to determine the impact of the permeability relationship on pressure transient response. Since the radial flow period may be hidden by changing permeability effects, it is important to understand how changing permeability alter the pressure response to accurately estimate reservoir parameters. Pinzon, Chen & Teufel (2000) showed that for radial flow, the pressure derivative showed increasing slope for drawdown and decreasing slope for buildup in case of stress-sensitive formation.

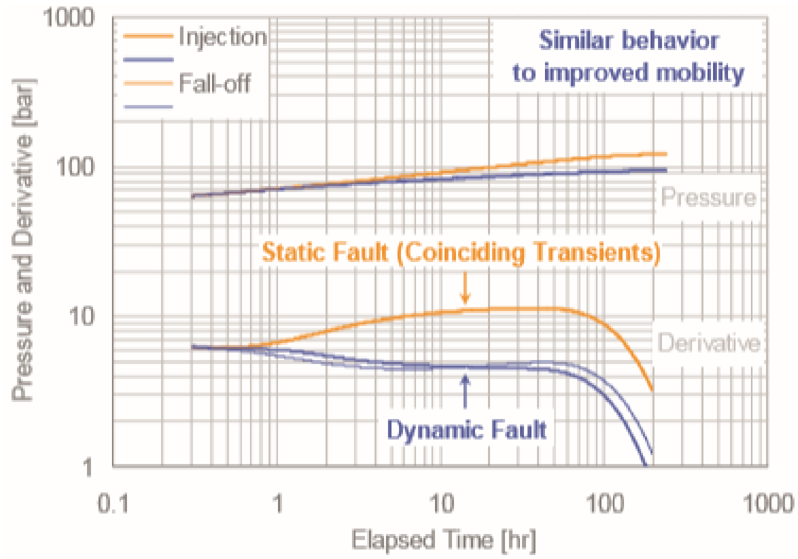


*Figure 2.9 Dynamic fault signature in synthetic pressure derivative response (Shchipanov et al., 2011).*

Another indication of the presence of stress-sensitive properties, matrix, fractures, faults etc. of the tested formation is non-coinciding pressure derivative curves (Shchipanov et al., 2011), as shown in Figure 2.9. This can help in distinguishing dynamic reservoir features from static high conductivity zones.

# 3 Pressure Diffusivity in Stress-sensitive Reservoirs, A General Study

To consider stress-dependent permeability, of an otherwise homogeneous medium, an Implicit pressure solver was created, using MS Excel VBA, with derivations given in Appendix A. These derivations have a basis in the book by Abou-Kassem, Farouq Ali & Islam (2006). The grid is represented by $n_r$ cylinder sections, each of volume $\left(r_{i+\frac{1}{2}}^2 - r_{i-\frac{1}{2}}^2\right)\pi h$.

***Table 3.1 Implicit pressure solver parameters***

| | Value | Unit |
|---|---|---|
| **Well** | | |
| Wellbore pressure | 0.1 | m |
| Skin factor | 0 | |
| **Fluid** | | |
| Water viscosity | 1 | cP |
| Water compressibility | 2E-4 | $bar^{-1}$ |
| Formation volume factor | 1 | $m^3/Sm^3$ |
| **Reservoir** | | |
| External reservoir radius | 100 | m |
| Permeability | 300 | mD |
| Thickness | 100 | m |
| Porosity | 0.3 | |
| Rock compressibility | 3E-6 | $bar^{-1}$ |
| Initial reservoir pressure | 200 | bara |
| **Geomechanics** | | |
| Permeability modulus | 1E-3 | $bar^{-1}$ |
| Poisson's ratio | 0.29 | |
| Biot's constant | 1 | |
| Initial total reservoir stress | 500 | bara |
| **Boundary conditions** | | |
| Outer pressure | 200 | bara |
| Inner pressure | 225 | bara |
| Outer rate | 0 | $m^3/day$ |
| Inner rate | 500 | $m^3/day$ |

Explicit models may have time step restrictions. As a first attempt, an explicit model was attempted. This model was quickly disregarded, because of the instability of the model at time steps > 1 second. **Table 3.1** shows the well, fluid, reservoir and geomechanical parameters used for simulation. It also shows the boundary conditions used for the different runs.

## 3.1 General matrix form

Because of the instability of the explicit scheme, an implicit scheme was created. The pressure of each grid cell was calculated by using the Thomas Algorithm (Aziz & Settari, 1979; Lee, 2011) on the resulting tri-diagonal matrix solution, shown in Equation (3.1)

$$\begin{bmatrix} b_1 & c_1 & & & \\ \ddots & \ddots & & & \\ a_i & b_i & c_i & & \\ & \ddots & \ddots & c_{n_r-1} & \\ & & a_{n_r} & b_{n_r} & \end{bmatrix} \begin{bmatrix} P_1^{n+1} \\ \vdots \\ P_i^{n+1} \\ \vdots \\ P_{n_r}^{n+1} \end{bmatrix} = \begin{bmatrix} d_1 \\ \vdots \\ d_i \\ \vdots \\ d_n \end{bmatrix} \; or \; [A]\cdot\vec{P} = \vec{d} \qquad (3.1)$$

The pressure, $\vec{P}$, is calculated by Equation (3.2), where coefficients $c_i'$ and $d_i'$ are given by Equations (3.3) and (3.4)

$$P_{n_r}^{n+1} = d_{n_r}'$$
$$P_i^{n+1} = d_i' - c'_i P_{i+1}^{n+1} \; ; i = n_r - 1, n_r - 2, \dots, 1 \qquad (3.2)$$

$$c_i' = \begin{cases} \dfrac{c_i}{b_i}; i = 1 \\ \dfrac{c_i}{b_i - a_i c'_{i-1}}; i = 2, 3, \dots, n_r - 1 \end{cases} \tag{3.3}$$

$$d_i' = \begin{cases} \dfrac{d_i}{b_i}; i = 1 \\ \dfrac{d_i - a_i d'_{i-1}}{b_i - a_i c'_{i-1}}; i = 2,3, .., n_r \end{cases} \tag{3.4}$$

Cases of both linear, i.e. constant permeability, and non-linear, stress-sensitive permeability, pressure diffusivity were run. The stress-pressure relations are those taken from the paper by Settari et al. (2005) given in Sections 2.7.2.1 through 2.7.2.3.

## 3.2 Implicit pressure solver

This section summarises the results from the Implicit pressure solver created in this thesis. The macro used for solving the matrix in Equation (3.1), is shown in Appendix B. All results are compared with its appropriate Eclipse model, except for the global correction model. This is because it uses average reservoir pressure as the driver for stress and permeability change, which is not available for testing in Eclipse. The Eclipse verification code was provided by Anton Shchipanov (2017) and modified to accommodate for pressure-dependent permeability and constant pressure inner and outer boundaries. The verification model can be found in Appendix C.

The main objective of the comparison of the different models is to understand the effect each model's pressure-stress formulation has on permeability, and in effect the difference between the models.

Four sets of boundary conditions were tested:

1) The combination of constant injection rate and closed outer boundary, $Q_{const} = 500 \frac{m^3}{day}$ and $Q_{out} = 0 \frac{m^3}{day}$
2) The combination of constant injection rate and constant pressure outer boundary, $Q_{const} = 500 \frac{m^3}{day}$ and $P_{bound,o} = 200\ bara$
3) The combination of constant pressure inner and outer boundary, $P_{bound,i} = 225\ bara$ and $P_{bound,o} = 200\ bara$
4) The combination of constant pressure inner boundary and closed outer boundary, $P_{bound,i} = 225\ bara$ and $Q_{out} = 0 \frac{m^3}{day}$

The macro is verified against Eclipse for wellbore pressure, $P(r = r_w, t)$ and pressure distribution, $P(r, t)$ for all combinations of boundary conditions and pressure-stress models (1) and (2). The constant permeability case, of constant rate inner boundary and closed outer boundary is compared with an analytical model created using Kappa Saphir.

The derivative of $\Delta P$ with respect to $\Delta t$, $\Delta P'$, is plotted for the case of constant rate inner boundary- and closed outer boundary condition for all cases of pressure-stress model. The cases of constant, either inner, outer or both, pressure conditions showed derivatives equal to zero, i.e. constant wellbore pressure, from early time steps, and are therefore not shown. Note that the graphs with legend "Bourdet derivative" are wellbore pressure results from the Implicit pressure solver, and derivated using the Bourdet derivative mentioned in Section 2.5.2. The graphs noted "Kappa derivative" are derivatives calculated using Kappa Saphir. Graphs with legend of "Implicit P.S." are wellbore pressures originating from the Implicit pressure solver.

### 3.2.1 *Constant injection rate and closed outer boundary*

#### *3.2.1.1 <u>Verification of models</u>*

For verification of the numerical models, the wellbore pressure, $P(r = r_w, t)$, and pressure distribution, $P(r, t)$, are used. For the case of constant permeability, an analytical model is used to compare with the two numerical models.

##### *3.2.1.1.1 Constant permeability*

The Implicit pressure solver was first run for the case of constant permeability. For verification with analytical and numerical models, the wellbore pressure, $P(r = r_w, t)$, is used. As shown in Figure 3.1, the wellbore pressure for all three models are almost equal, with only a slight delay of the Implicit pressure solver.

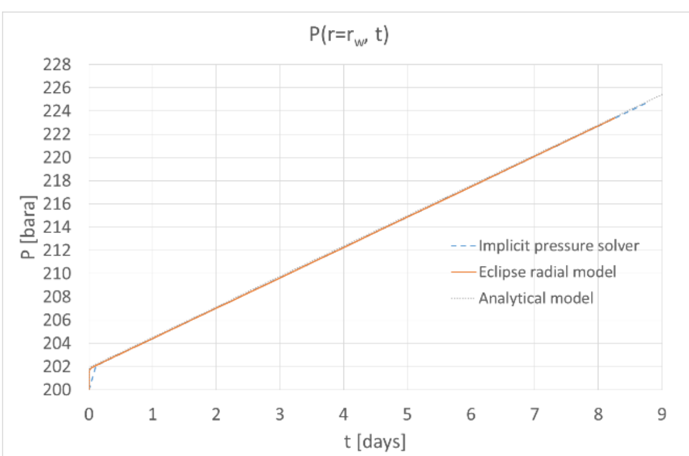


*Figure 3.1 Wellbore pressure, constant permeability case. Implicit pressure solver, Eclipse and Analytical model comparison.*

*3.2.1.1.2 No correction for stress change, $\Delta\sigma_m = 0$*

The model responses for $\Delta\sigma_m = 0$, i.e. no change in total stress with pressure change, are shown below in Figure 3.2. Comparison of the wellbore pressure, shown in Figure 3.2 a), shows that the wellbore pressure of the two models are almost equal, with only the Eclipse model giving slightly higher wellbore pressure than the Implicit pressure solver. Another step taken to verify the pressure response of the Implicit pressure solver, is the pressure distribution in the reservoir at various times, as shown in Figure 3.2b) below:

a) b)

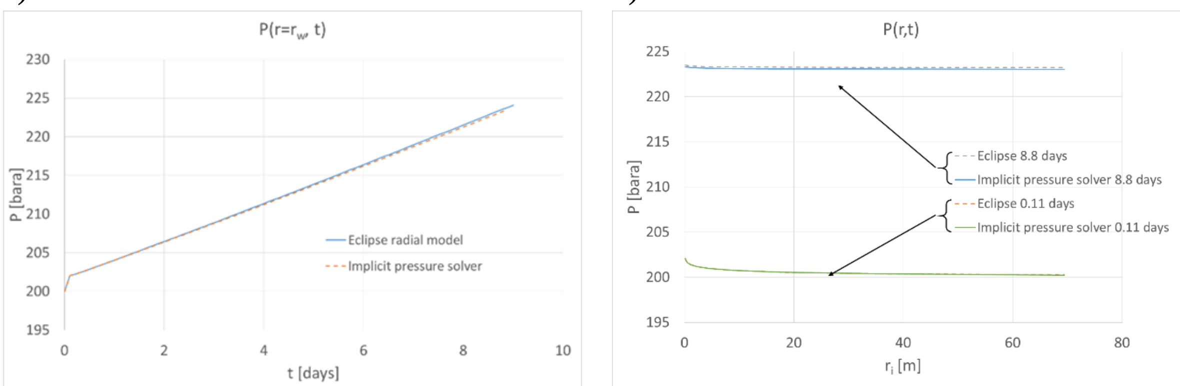


*Figure 3.2 Implicit pressure solver vs. Eclipse. a) Wellbore pressure and b) Pressure distribution. $\Delta\sigma_m = 0$*

*3.2.1.1.3 Local pressure correction model, $\Delta\sigma_m = f(\Delta P)$*

The model responses for $\Delta\sigma_m = f(\Delta P)$, i.e. a function of local pressure change, agree well between the two numerical models shown in Figure 3.3. The model response of wellbore pressure from the Implicit pressure solver is only slightly smaller than that of the Eclipse radial model, Figure 3.3a). Another step taken for verification, is comparing the $P(r,t)$ model responses. As shown in Figure 3.3b) below, $P(r,t)$ for both numerical models are almost equal.

a) b)

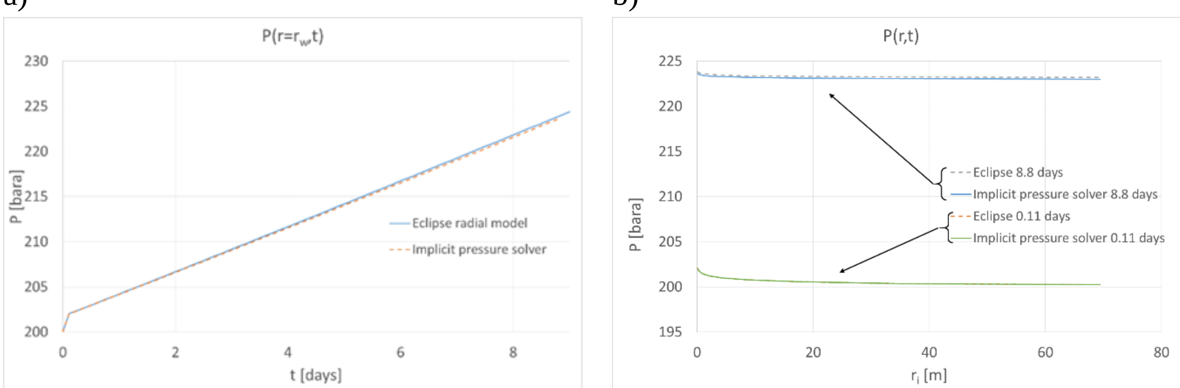


*Figure 3.3 Implicit pressure solver vs. Eclipse. a) Wellbore pressure and b) Pressure distribution. $\Delta\sigma_m = f(\Delta P)$*

*3.2.1.1.4 Global pressure correction model,* $\Delta\sigma_m = f(\Delta P, \Delta P_{avg})$

Because of not being able to include the average reservoir pressure as the driver for pressure-dependent permeability in Eclipse, the Implicit pressure solver with the global pressure-stress correction cannot be compared with an Eclipse model. The results of this single simulation model are shown in Figure 3.4 a) and b) below.

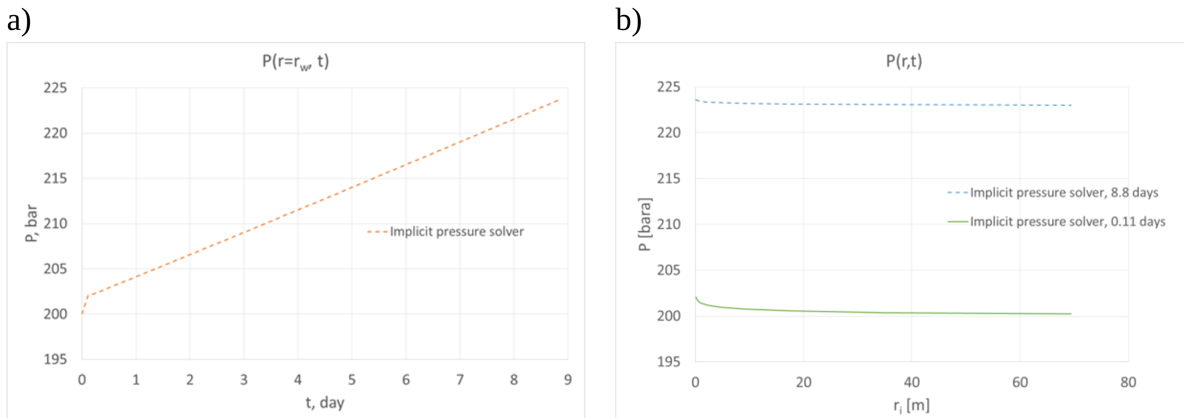


*Figure 3.4 Implicit pressure solver vs. Eclipse. a) Wellbore pressure and b) Pressure distribution.* $\Delta\sigma_m = f(\Delta P, \Delta P_{avg})$

*3.2.1.2* *<u>Derivative response</u>*

For the case of constant permeability, the Bourdet derivative deviates slightly from the derivatives calculated using Saphir, up to ~1 day of injection. From 1 day and until the end of injection the derivatives coincide. For the stress-dependent permeability cases, marked No correction, Local correction and Global correction, all three derivatives coincide, except at time step 1, i.e. after 0.11 days of injection. As the outer boundary is closed, the derivative increases as is expected. These results are shown in Figure 3.5 a) through d).

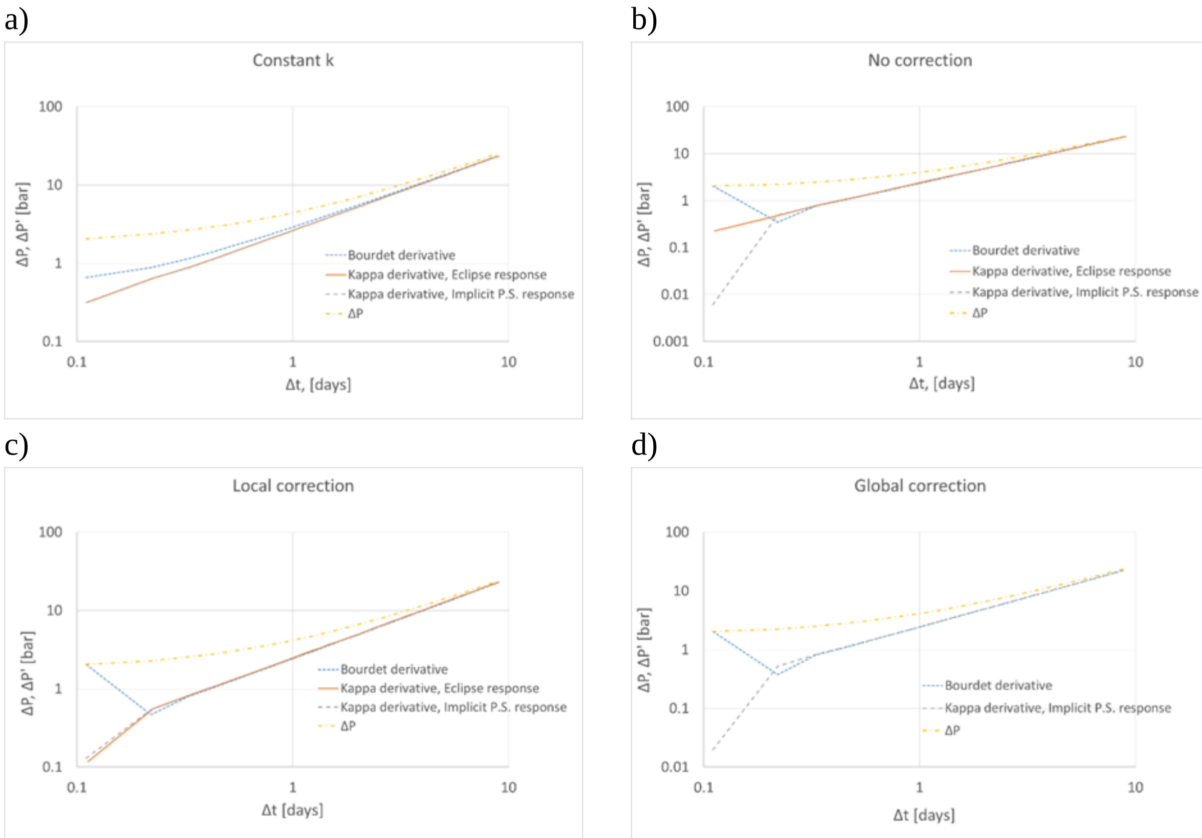


*Figure 3.5 Pressure derivative and $\Delta P$, for constant injection rate and closed outer boundary. a) constant permeability, b) no correction pressure-stress model, c) local correction pressure-stress model, d) global correction pressure-stress model.*

### 3.2.1.3 <u>Model comparison</u>

This section regards comparison of pressure and permeability distribution between the three pressure-stress models used in the Implicit pressure solver. The pressure distribution, $P(r,t)$ was plotted for two time steps, and is given in Figure 3.6 below.

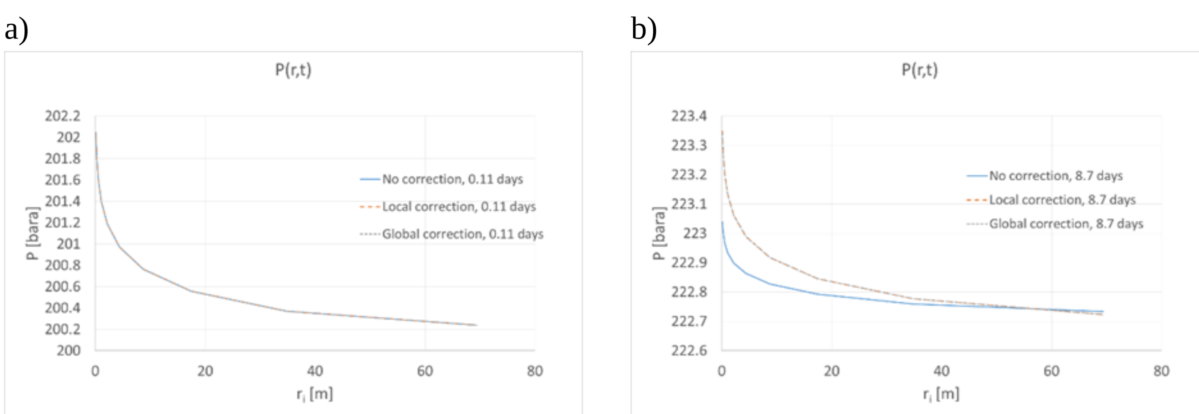


*Figure 3.6 Comparison of reservoir pressure distribution, pressure-stress models a) after 0.11 days b) after 8.7 days*

The resulting permeability distribution of the three models, from the pressures in Figure 3.6, were also plotted. As shown above, $P(r,t)$ is not greatly affected by the different stress model, but gives quite different permeability distribution shown in Figure 3.7 below.

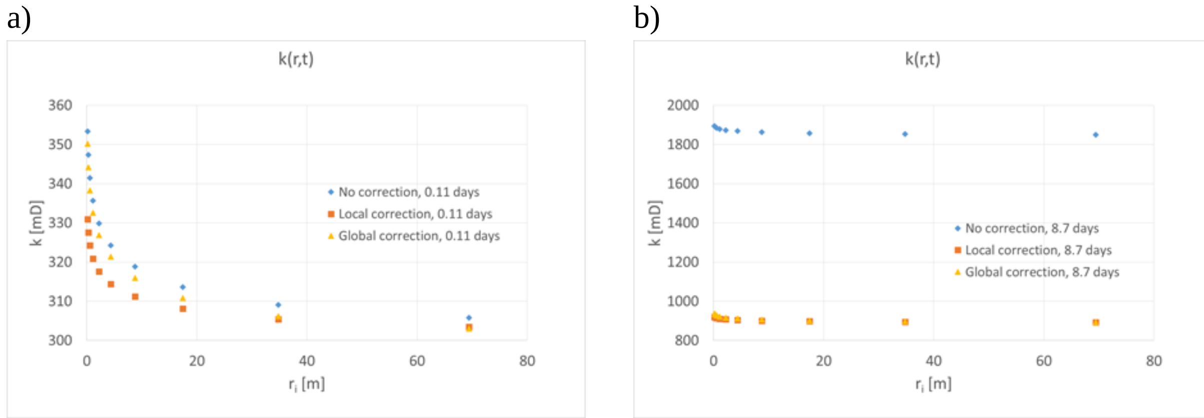


*Figure 3.7 Comparison of reservoir permeability distribution of the pressure-stress models a) after 0.11 days b) after 8.7 days*

As observed in Figure 3.7, the permeability given by the model not accounting for mean stress change with pressure is consistently higher than that of the models accounting for mean total stress change. Of these latter models, the one correcting for average pressure change, i.e. $k\left(\Delta\sigma_m = f\left(\Delta P, \Delta P_{avg}\right)\right)$, is larger than that correcting for local pressure change, $k\left(\Delta\sigma_m = f(\Delta P)\right)$, i.e.:

$$k(\Delta\sigma_m = 0) > k\left(\Delta\sigma_m = f(\Delta P)\right) > k\left(\Delta\sigma_m = f\left(\Delta P, \Delta P_{avg}\right)\right) \quad (3.5)$$

### *3.2.2 Constant injection rate and constant pressure outer boundary*

#### *3.2.2.1 <u>Verification of models</u>*

For this case of boundary conditions, the pressure distribution equilibrated quite early, in < 1 day. Because of this, $P(r,t)$ and $k(r,t)$ are plotted for earlier times than for the previous set of boundary conditions, more exactly at times 0.11 days and 1.0 days after the start of injection.

##### *3.2.2.1.1 Constant permeability*

The Implicit pressure solver was run for the case of constant permeability. As seen in Figure 3.8 a) below, the wellbore pressure coincides well between the Implicit pressure solver and Eclipse. The same is true for the pressure distribution, $P(r,t)$, which is shown in Figure 3.8 b).

a) b)

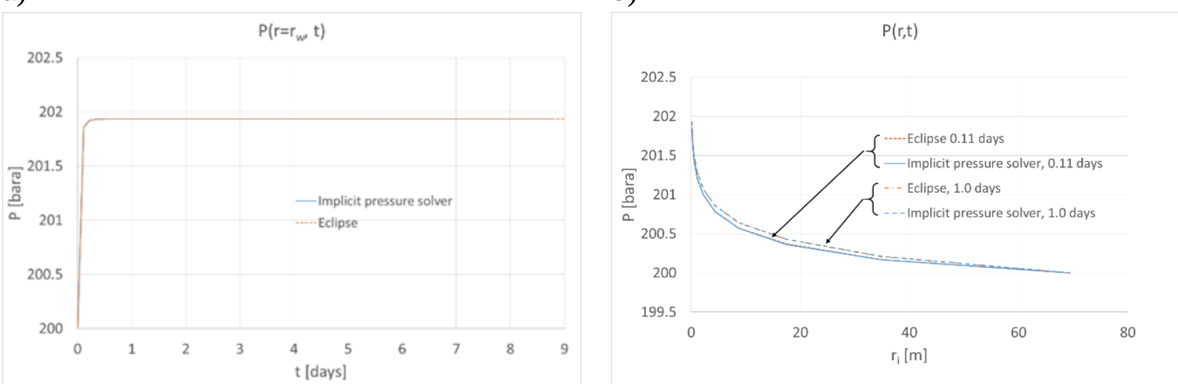


*Figure 3.8 Implicit pressure solver vs. Eclipse. a) Wellbore pressure and b) Pressure distribution. Constant permeability*

##### *3.2.2.1.2 No correction for stress change, $\Delta\sigma_m = 0$*

The pressure responses for the model assuming no correction of mean total stress are shown below. The wellbore pressure from both the Eclipse model and the Implicit pressure solver are almost equal, see Figure 3.9 a) below. The pressure distribution at given times are shown in Figure 3.9b).

a) b)

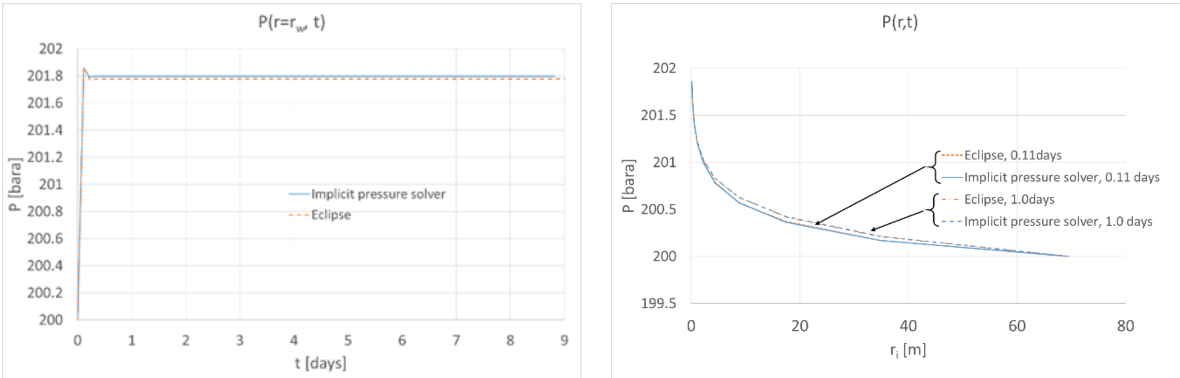


*Figure 3.9 Implicit pressure solver vs. Eclipse. a) Wellbore pressure and b) Pressure distribution. $\Delta\sigma_m = 0$*

### 3.2.2.1.3 Local pressure correction model, $\Delta\sigma_m = f(\Delta P)$

The wellbore pressure responses of both numerical models agree well, as is shown in Figure 3.10 a). The same can be seen for the pressure distribution, $P(r,t)$ in Figure 3.10 b).

a) b)

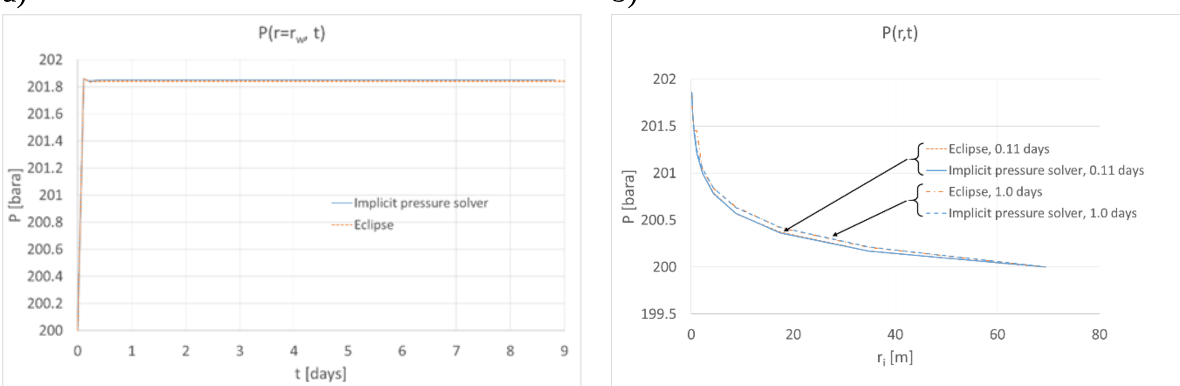


*Figure 3.10 Implicit pressure solver vs. Eclipse. a) Wellbore pressure and b) Pressure distribution. $\Delta\sigma_m = f(\Delta P)$*

### 3.2.2.1.4 Global pressure correction model, $\Delta\sigma_m = f(\Delta P, \Delta P_{avg})$

Because of not being able to use average reservoir pressure as the driver for permeability change in Eclipse, the results of the Implicit pressure solver cannot be compared with numerical results from Eclipse. The results of this single simulation are shown below in Figure 3.11 a) and b).

a) b)

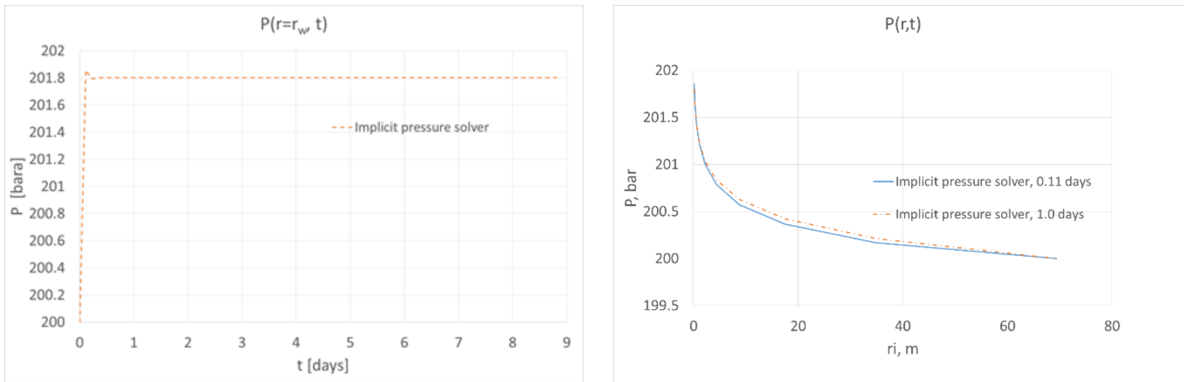


*Figure 3.11 Implicit pressure solver vs. Eclipse. a) Wellbore pressure and b) Pressure distribution. $\Delta\sigma_m = f(\Delta P, \Delta P_{avg})$*

### 3.2.2.2 Derivative response

For the case of constant injection rate and constant outer pressure, the wellbore pressure increases slightly above the outer boundary pressure, i.e. 200 bara. As the wellbore pressure becomes constant, the derivatives approach 0.

### 3.2.2.3 Model comparison

The pressure, $P(r,t)$, and permeability, $k(r,t)$, are plotted for two time steps to show the difference between the permeabilty generated by the different models at similar pressures. The pressure distribution, $P(r,t)$ is plotted for two time steps, and is given in Figure 3.12 below.

a) b)

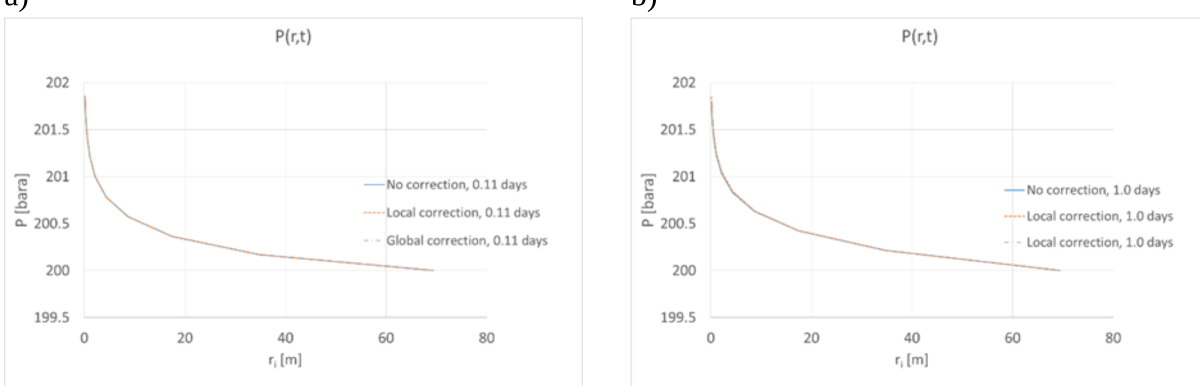


*Figure 3.12 Comparison of P(r,t) at a) 0.11days, b) 1.0 days*

As can be seen in Figure 3.12, the $P(r,t)$ curves coincide for all the tested times. Because the pressure of each individual grid block is quite close to the initial reservoir pressure, < 2 bara higher, the grid block permeability resulting from each model does not show an enormous difference. The resulting permeability distribution in the cells are shown in Figure 3.13b), which shows a maximum permeability difference of ~25 mD in the highest-pressure zone.

a) b)

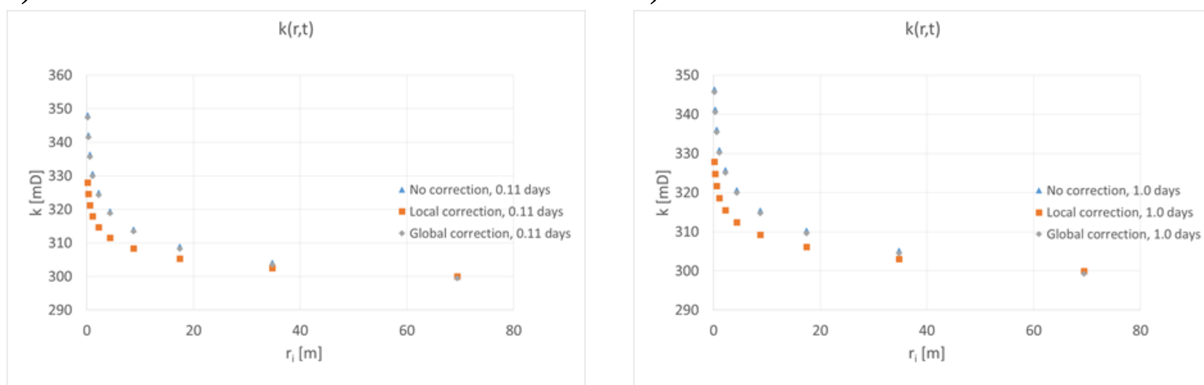


*Figure 3.13 Comparison of k(r,t) at a) 0.11days, b) 1.0 days*

From Figure 3.13, it is evident that the model correcting for local pressure stress-correction gives the lowest permeability, whilst the non-correcting model gives the highest permeability value, i.e. the same result as for the other set of boundary conditions, see Equation (3.6).

$$k(\Delta\sigma_m = 0) > k\big(\Delta\sigma_m = f(\Delta P)\big) > k\left(\Delta\sigma_m = f\big(\Delta P, \Delta P_{avg}\big)\right) \tag{3.6}$$

### ***3.2.3 Constant inner pressure and constant outer pressure***

#### *3.2.3.1 <u>Verification of models</u>*

As for the previously simulated boundary conditions, the wellbore pressure, and the pressure distribution are used for verification between the Implicit pressure solver and Eclipse for the different pressure-stress models. The time steps used for verification of the models are the same as for the case of constant injection rate and outer constant pressure boundary condition since the reservoir reaches pressure equilibrium in < 1 day of injection.

##### *3.2.3.1.1 Constant permeability*

The Implicit pressure solver was run for the case of constant permeability. As shown in Figure 3.14 a) below the wellbore pressure of the Implicit pressure solver is equal to the Eclipse response. As for the pressure distribution, Figure 3.14 b), the Implicit pressure solver overestimates the pressure by ~10bara in the inner grid blocks, i.e. grid blocks 2 through 9, after one day of injection. The source of this difference is not known at this point.

a) b)

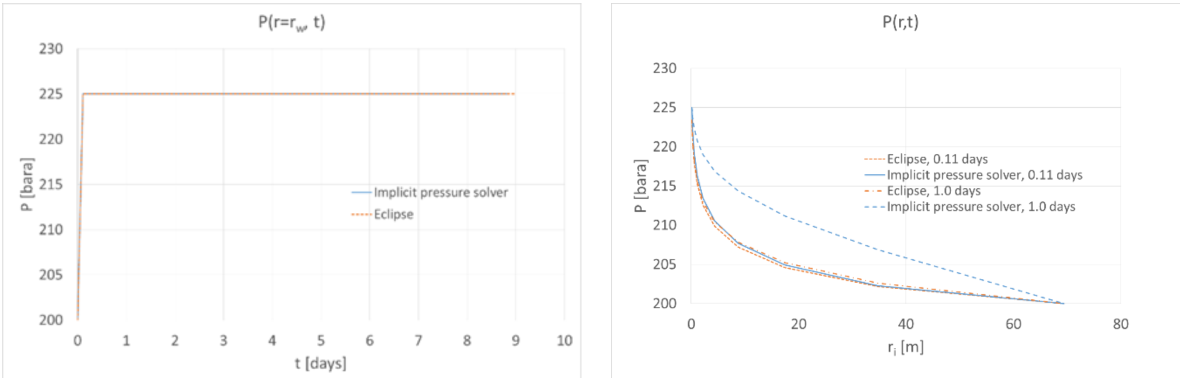


*Figure 3.14 Implicit pressure solver vs. Eclipse. a) Wellbore pressure and b) Pressure distribution. Constant permeability.*

### *3.2.3.1.2 No correction for stress change,* $\Delta\sigma_m = 0$

The model response of both the Implicit pressure solver and Eclipse are shown in Figure 3.15 a) and b) below. The wellbore pressure fits exactly between the Implicit pressure solver and Eclipse, whilst the Implicit pressure solver gives a slightly higher pressure of each grid block.

a) b)

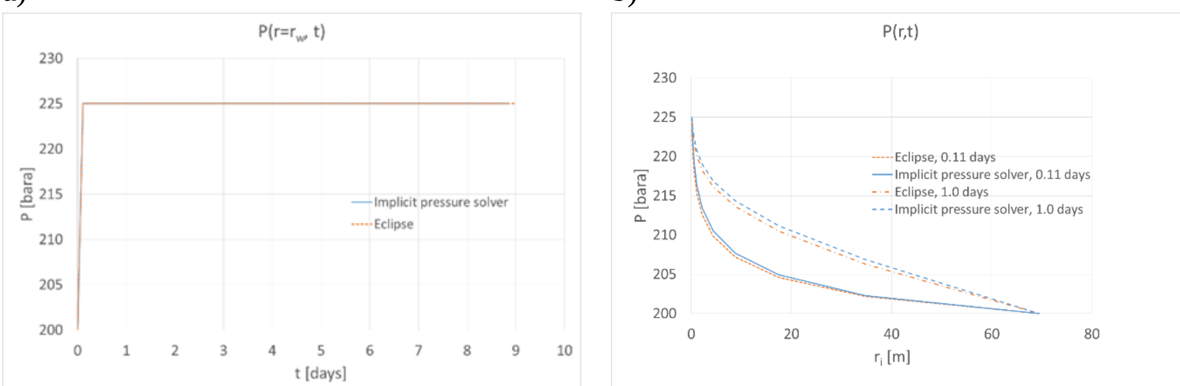


*Figure 3.15 Implicit pressure solver vs. Eclipse. a) Wellbore pressure and b) Pressure distribution.* $\Delta\sigma_m = 0$

### *3.2.3.1.3 Local pressure-correction model,* $\Delta\sigma_m = f(\Delta P)$

In the case of this pressure-stress correction model the Implicit pressure solver and Eclipse give the same wellbore pressure, Figure 3.16 a), and similar reservoir pressure distribution, Figure 3.16 b), in the case of the local pressure-stress correction.

a) b)

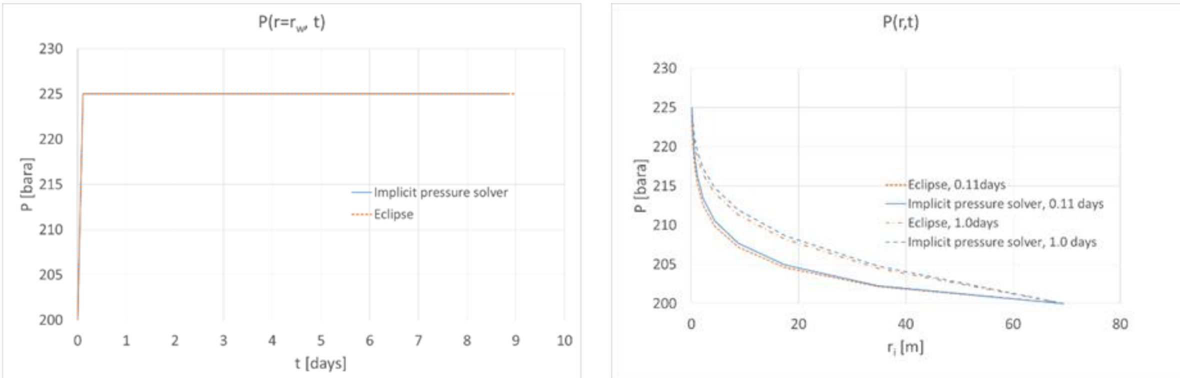


*Figure 3.16 Implicit pressure solver vs. Eclipse. a) Wellbore pressure and b) Pressure distribution. $\Delta\sigma_m = f(\Delta P)$.*

*3.2.3.1.4 Global pressure-correction model,* $\Delta\sigma_m = f(\Delta P, \Delta P_{avg})$

As before, Eclipse is not able to apply average reservoir pressure as the driver of permeability change, therefore the only available results come from the Implicit pressure solver. Wellbore pressure and the pressure distribution are plotted in Figure 3.17 a) and b) respectively below.

a) b)

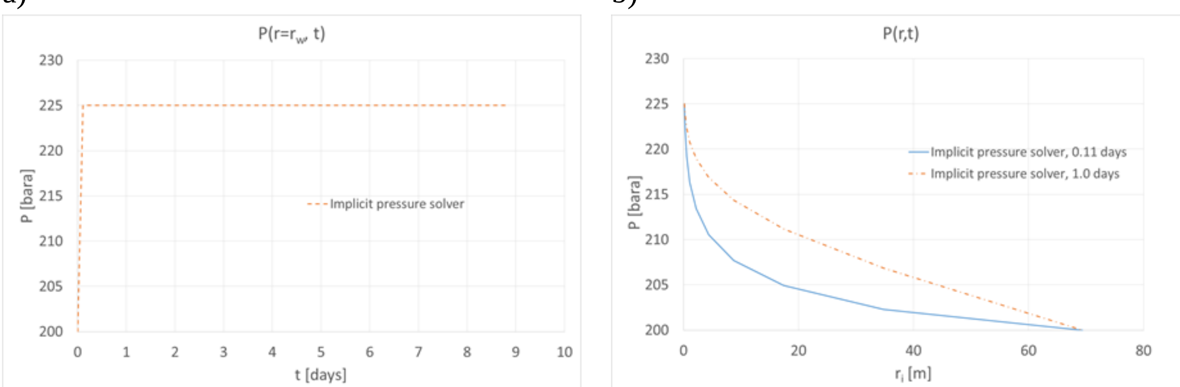


*Figure 3.17 Implicit pressure solver vs. Eclipse. a) Wellbore pressure and b) Pressure distribution. $\Delta\sigma_m = f(\Delta P, \Delta P_{avg})$*

*3.2.3.2 <u>Derivative response</u>*

Since the wellbore pressure is equal to 225 bara for all times, the derivative is zero for the entire length of the injection period, regardless of pressure-stress model, and is therefore not plotted.

#### 3.2.3.3 <u>Model comparison</u>

Pressure and permeability distribution of the reservoir are compared in the current section. The pressure distribution is plotted for a series of time steps, and given in Figure 3.18 below:

a) b)

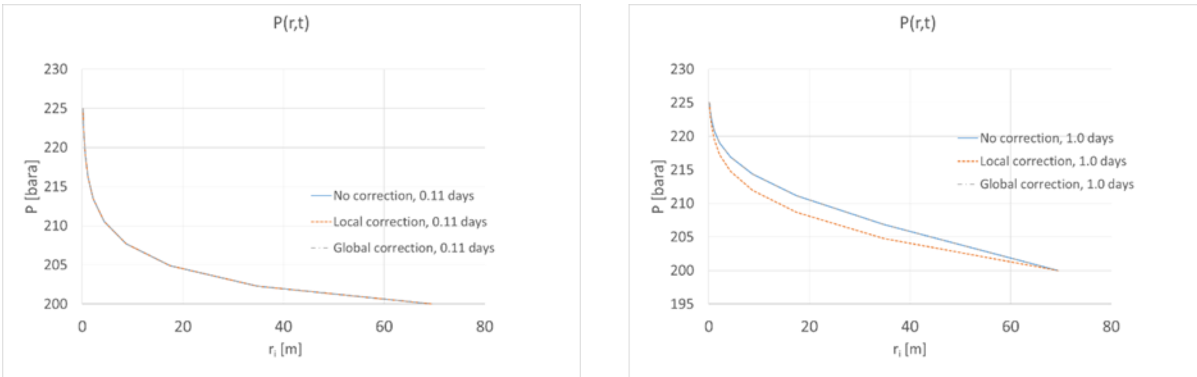


*Figure 3.18 Pressure distribution, comparison of pressure-stress models, at a) 0.11 days, b) 1.0 days of injection*

As can be seen, the stress model correcting for local pressure change gives a lower pressure in each of the inner grid cells, for all times.

As shown in Figure 3.18, the pressure distribution of the radial reservoir is similar, but has quite a major difference in resulting permeability, shown in Figure 3.19.

a) b)

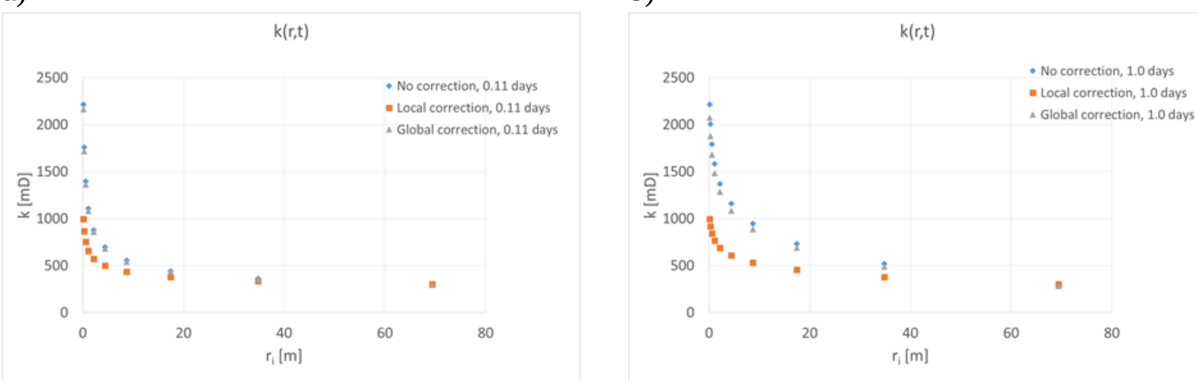


*Figure 3.19 Permeability of grid blocks, comparison of pressure-stress models at a) 0.11 days, b) 1.0 days of injection.*

As for the previous two sets of boundary conditions, the local pressure correction model gives the lowest permeability compared to the other two pressure-stress models, as shown in Figure 3.19 above, i.e.:

$$k(\Delta\sigma_m = 0) > k\big(\Delta\sigma_m = f(\Delta P)\big) > k\left(\Delta\sigma_m = f\big(\Delta P, \Delta P_{avg}\big)\right) \qquad (3.7)$$

### 3.2.4 *Constant inner pressure and closed outer boundary*

#### *3.2.4.1 Verification of models*

For verification of the numerical models, the wellbore pressure and the pressure distribution is used. For this set of boundary conditions, the pressure distribution is plotted for the same time steps as the two previous sets of boundary conditions, i.e. after 0.11 and 1.0 days of injection.

##### *3.2.4.1.1 Constant permeability*

Eclipse and the Implicit pressure solver were run for the case of constant permeability. The plots of wellbore pressure and pressure distribution are shown in Figure 3.20 a) and b) respectively. The wellbore pressure of both numerical models increases to 225 bara during the first time-step, i.e. before 0.11 days of injection. The pressure distribution is almost equal between the models, see Figure 3.20 b).

a) b)

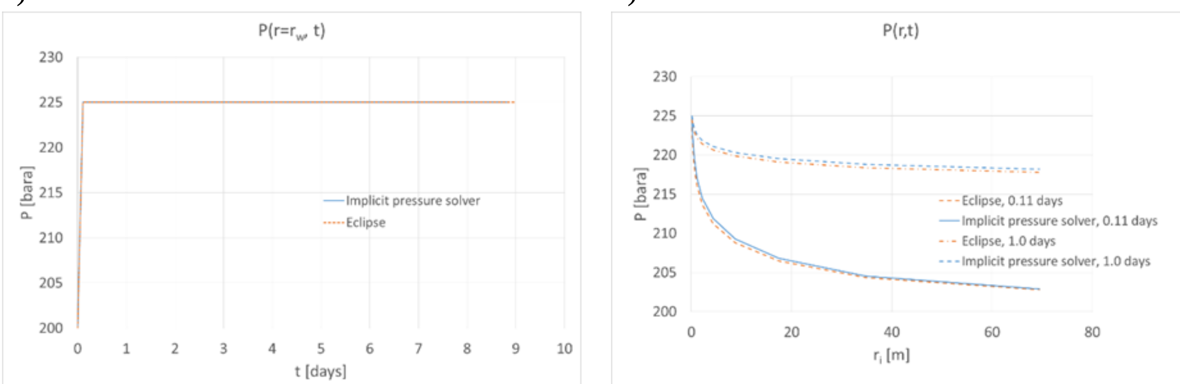


*Figure 3.20 Implicit pressure solver vs. Eclipse. a) Wellbore pressure and b) Pressure distribution. Constant permeability.*

##### *3.2.4.1.2 No correction for stress change, $\Delta\sigma_m = 0$*

The pressure responses for the models assuming no change in total stress with pressure are shown below in Figure 3.21 a) and b). As for the other cases of constant inner pressure, the wellbore pressure equals 225 bara from the first time-step to the end of the simulation. $P(r,t)$ agree well for all plotted times.

a) b)

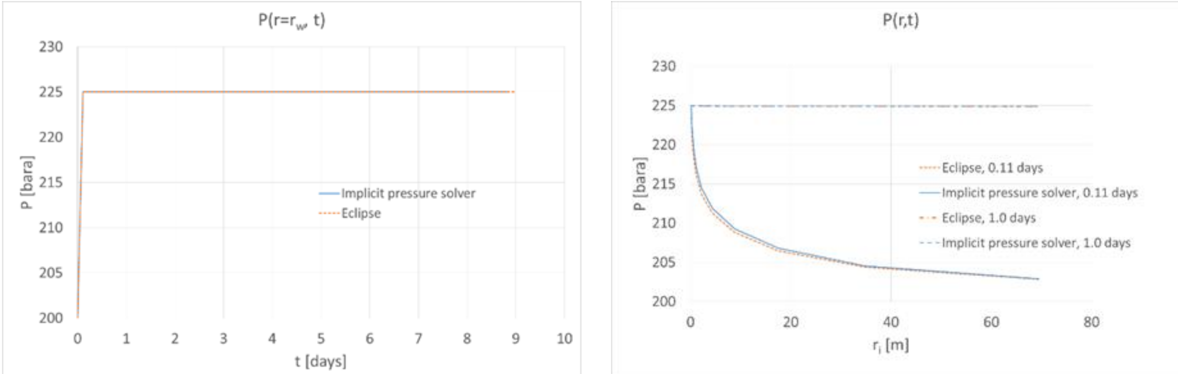


*Figure 3.21 Implicit pressure solver vs. Eclipse. a) Wellbore pressure and b) Pressure distribution.* $\Delta\sigma_m = 0$

### 3.2.4.1.3 *Local pressure correction model,* $\Delta\sigma_m = f(\Delta P)$

For this pressure-stress model, the plots of wellbore pressure and pressure distribution are shown in Figure 3.22 a) and b) respectively. The wellbore pressures of both models are equal to 225 bara from 0.11 days of injection and onwards, whilst the Implicit pressure solver estimates higher pressures for all other grid cells for the plotted times, Figure 3.22 b).

a) b)

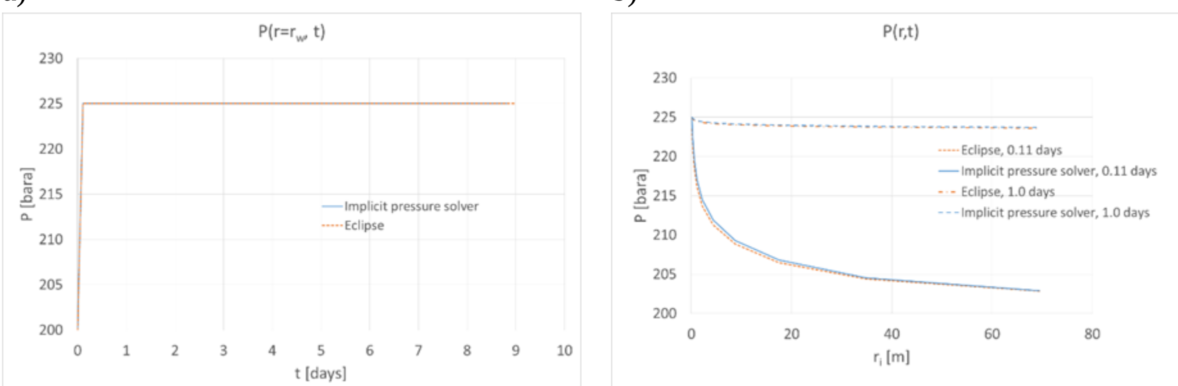


*Figure 3.22 Implicit pressure solver vs. Eclipse. a) Wellbore pressure and b) Pressure distribution.* $\Delta\sigma_m = f(\Delta P)$

### 3.2.4.1.4 *Global pressure correction model,* $\Delta\sigma_m = f(\Delta P, \Delta P_{avg})$

Average pressure cannot be used as a driver of permeability change in Eclipse. Therefore, the only values of wellbore pressure and pressure distribution are those of the Implicit pressure solver. These are given in Figure 3.23 a) and b) respectively.

a) b)

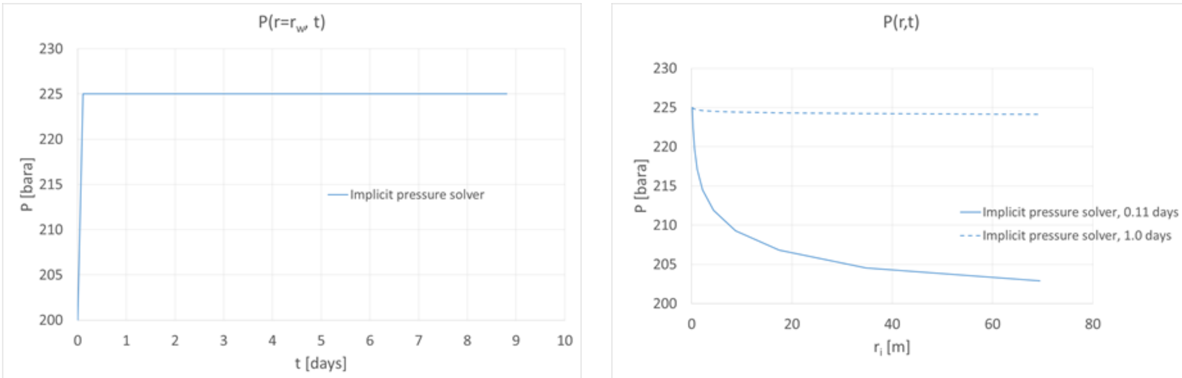


*Figure 3.23 Implicit pressure solver vs. Eclipse. a) Wellbore pressure and b) Pressure distribution. $\Delta\sigma_m = f(\Delta P, \Delta P_{avg})$*

### 3.2.4.2 Derivative response

Since constant wellbore pressure is established in the first time-step of both Eclipse and the Implicit pressure solver, all derivatives are zero and therefore not plotted.

### 3.2.4.3 Model comparison

The pressure, $P(r,t)$, and permeability, $k(r,t)$, are plotted for two time steps to show the difference between the permeabilty generated by the different models at similar pressures. $P(r,t)$ is plotted for the time steps mentioned in Section 3.2.4 and given in Figure 3.24 below.

a) b)

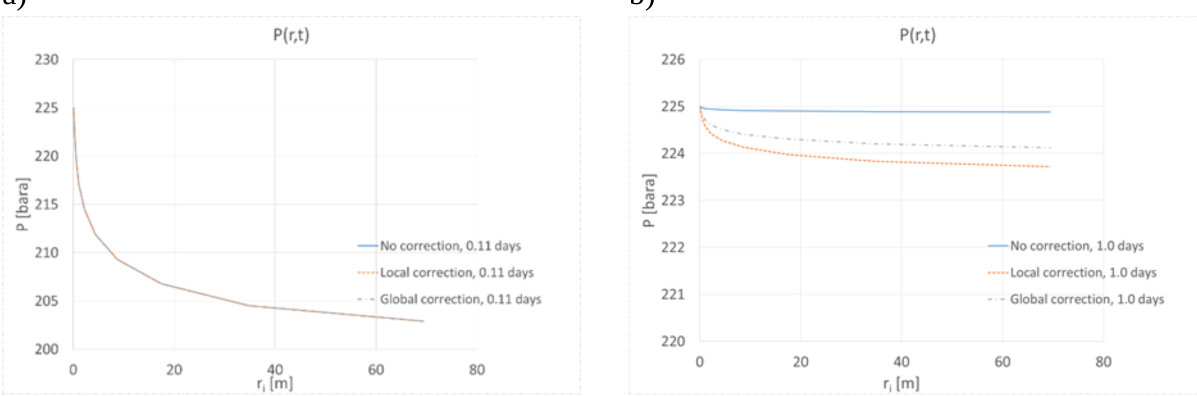


*Figure 3.24 Comparison of pressure distribution, all pressure-stress models. a) at 0.11 days, b) 1.0 days of injection.*

As shown in Figure 3.24, the $P(r,t)$ curves for the local correction gives the lowest values for all tested times.

The resulting permeability of the pressure distribution for the three pressure-dependent permeability models is given in Figure 3.25 below. As is the case for all the other tested combinations of boundary conditions, the non-correcting model yields the largest permeability, whilst the global pressure-stress correction yields the smallest permeability, i.e.:

$$k(\Delta\sigma_m = 0) > k\big(\Delta\sigma_m = f(\Delta P)\big) > k\left(\Delta\sigma_m = f\big(\Delta P, \Delta P_{avg}\big)\right) \tag{3.8}$$

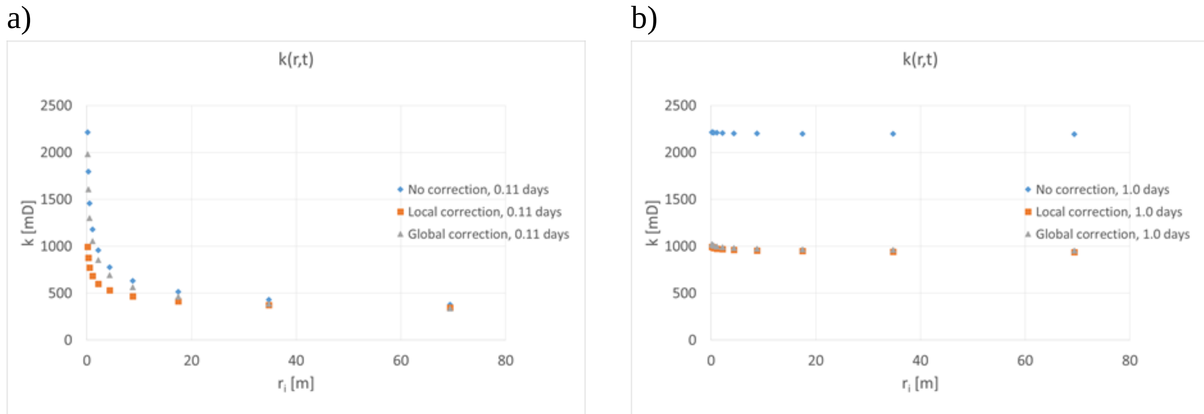


*Figure 3.25 Permeability comparison of the three pressure-stress models. a) at 0.11 days, b) 1.0 days of injection.*

### 3.2.5 *Model comparison*

Because the reservoir pressure development is slightly different for each pressure-stress model, a direct comparison of the models is made, i.e. permeability results compared at the same pressures, Figure 3.26. The values of the geomechanical parameters used in this comparison are the same as those given in **Table 3.1**, but the permeability multiplier is extended to cover a larger range than achieved in simulations with the Implicit pressure solver.

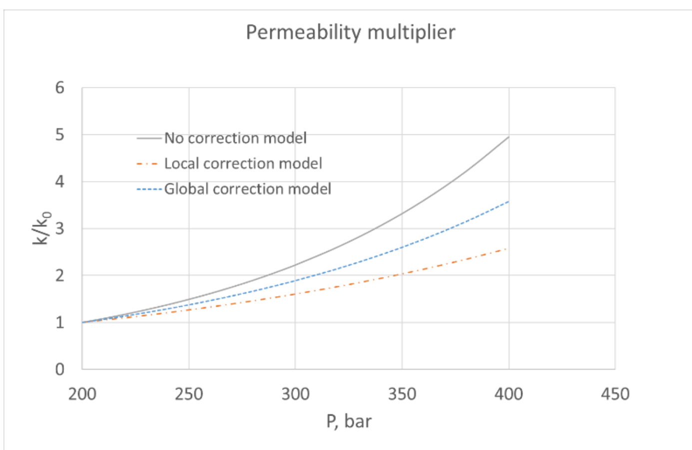


*Figure 3.26 Permeability multiplier, $k_0$ is the matrix permeability at initial pressure.*

As shown in Figure 3.26, the model not correcting for mean total stress change overestimates the permeability compared to the models including geomechanical considerations, i.e. change of mean total stress.

By varying Poisson's ratio, $\nu$, the local correction model gives the highest effective stress for all pressures, whilst the no correction model gives the lowest effective stress for all values of $\nu$, see Figure 3.27 a) through c). This would result in the lowest and the highest permeability for the local correction model and the non-correction model respectively.

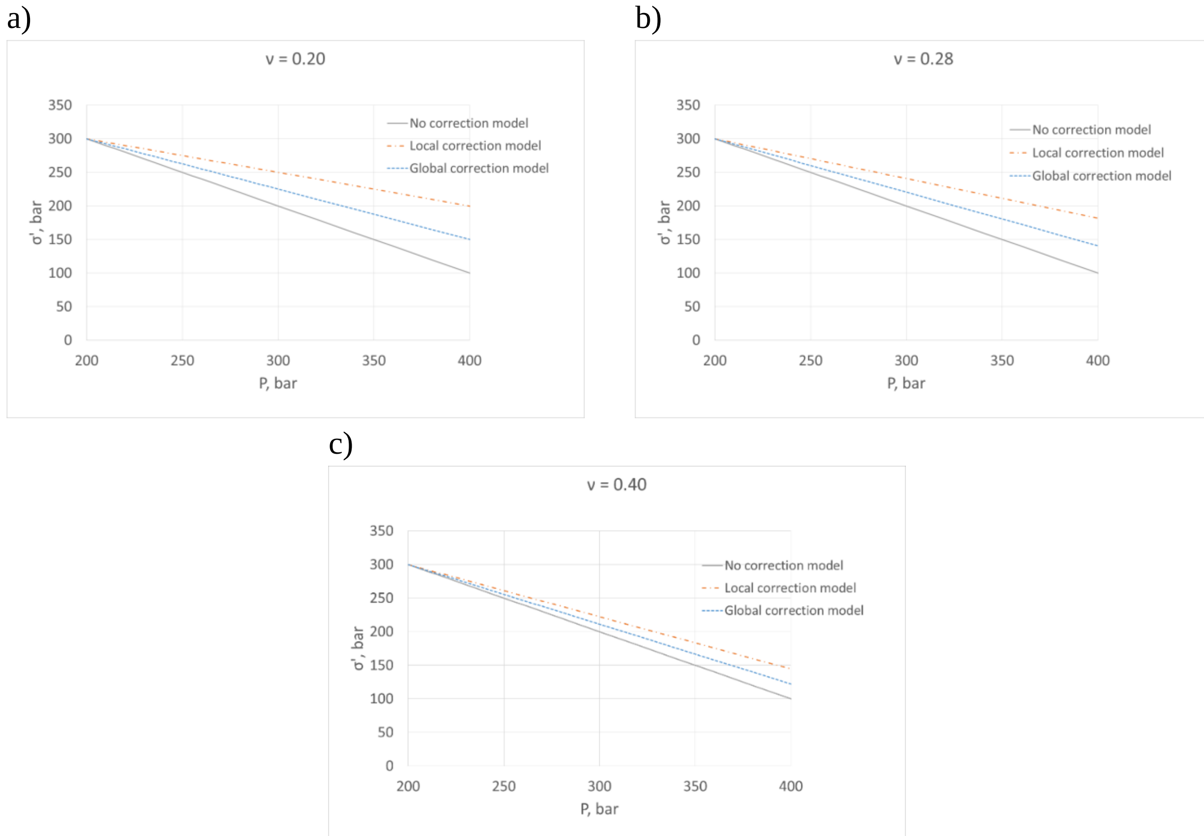


*Figure 3.27 Effect of varying $\nu$ on $\sigma'$. a) low $\nu$, b) medium $\nu$, c) high $\nu$*

### *3.2.6 Uncertainty*

Uncertainty governs all reservoir simulation. Uncertainty in input data, such as initial stress, geomechanical parameters, permeability tensor etc. makes is virtually impossible to work with reservoir simulation deterministically for projecting reservoir behaviour. One must, therefore, work with these uncertainties to consider the most likely behaviour. Considering fault reactivation, which is the main reason this thesis is written; This process is most likely governed by changes in global stress state, i.e. function of global pressure change. This cannot be directly tested in Eclipse, because of average reservoir pressure being a driver for stress and permeability change. Limitations in the current software make us unable to test this approximation without having to couple reservoir flow to a geomechanical simulator. However as shown in Figure 3.26 and Figure 3.27, the global correction model always calculates reservoir stress and permeabilities between that of the two models available for testing without geomechanical coupling.

Using a reservoir containing a single dynamic fault as an example; If one does not require knowing the exact fault behaviour, the non-correction and the local correction models can be run and the global correction model response should be somewhere in between the other two, see Figure 3.28 below:

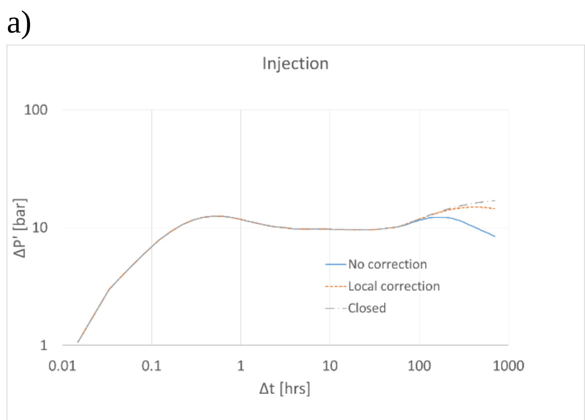


*Figure 3.28 Dynamic fault behaviour, no- and local correction models compared to closed static fault behaviour. a) Injection response, b) falloff response*

A closer look at the derivative response of the fault shows the area where the derivative response of the dynamic fault would be located. Note that the hatched area is where the pressure derivative of the global-correction stress model is expected.

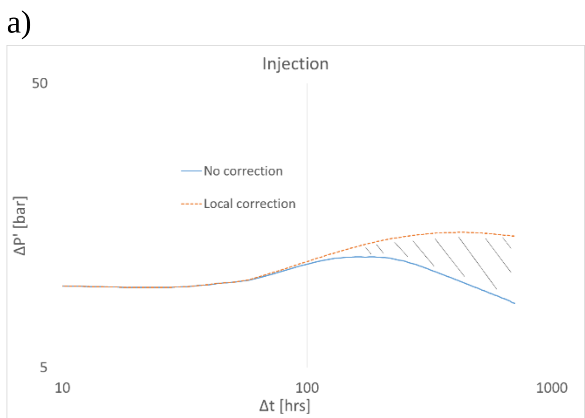


*Figure 3.29 Dynamic fault response, no-, local- and global correction models. a) Injection response, b) falloff response*

The transmissibility multipliers used to generate the response of Figure 3.28 and Figure 3.29 are given in Figure 3.30. The fault blocks initially have an x- and y-permeability of $10^{-5}$ mD.

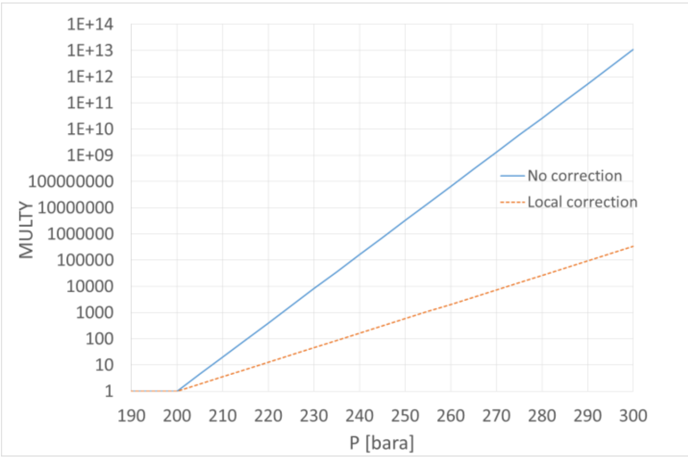


*Figure 3.30 Transmissibility multipliers, No- and local correction model.*

As reservoir stress dictates fault stability, i.e. stress acting on the fault plane, the development of the stress regarding pressure change is key to avoid fault slippage and reactivation. The concept of dynamic faults is further investigated in Chapter 4.

# 4 Dynamic Fault Reservoir Simulation

This section focuses on fault reactivation through pressure change. Firstly, the case of a single closed fault located 100m east of an injection well is analysed. A numerical model is generated in Eclipse, with reservoir parameters stated in **Table 4.1**. This numerical model is compared with analytical results generated using Kappa Saphir. The effect of grid block size on the numerical dispersion of the pressure transient is also looked at by varying grid block size.

Secondly, the case of a dynamic fault, i.e. reactivating fault with an increase in pressure, is investigated. The fault is located 100m east of an injection well as before. The reservoir parameters are the same as for the closed fault case, given in **Table 4.1**. The transmissibility between fault blocks increases exponentially with increasing pressure above the pressure defined as "Threshold pressure":

The Threshold pressure is the pore pressure at which the fault change for a sealing fault to an increasingly leaking fault with increasing pressure. At pressures lower than the Threshold pressure, the fault is sealing, i.e. $T_x = T_y = 0\ mD.m$.

Both the cases of closed and dynamic fault are subjected to 720 hours of water injection, followed by 720 hours of shut-in well, known as the falloff period, see Section 2.2.2. This is done to monitor dynamic fault behaviour and try to find a diagnostic response of the dynamic fault using pressure transient analysis for cases of both injection and falloff. All models are 2D, single phase water injection into a saline aquifer.

## 4.1 Closed fault

***Table 4.1 Properties of the model reservoir***

| Property | Value | Unit |
|---|---|---|
| Wellbore radius | 0.1 | m |
| Wellbore skin factor | 0 | |
| Injection rate | 1000 | $Sm^3/day$ |
| Height | 100 | m |
| Porosity | 0.3 | |
| Matrix permeability | 10 | mD |
| Formation compressibility | 3.0E-6 | $1/bar^{-1}$ |
| Distance to fault | 100 | m |
| Initial reservoir pressure | 200 | bara |
| Water viscosity | 1 | cP |
| Water density | 1013 | $kg/m^3$ |
| Water compressibility | 4.0E-5 | $1/bar^{-1}$ |
| Formation volume factor | 1 | $Rm^3/Sm^3$ |
| Injection period | 720 | hrs |
| Falloff period | 720 | hrs |

The case of a single closed fault is the subject of this investigation. Models created in the numerical reservoir flow simulator Eclipse E100 is compared with analytical results generated by Kappa Saphir for verification of the numerical model. The properties of the reservoir model are defined in **Table 4.1**.

The resulting model in Eclipse is shown in Figure 4.1. The fault is marked in blue, east of the injection well, INJ1

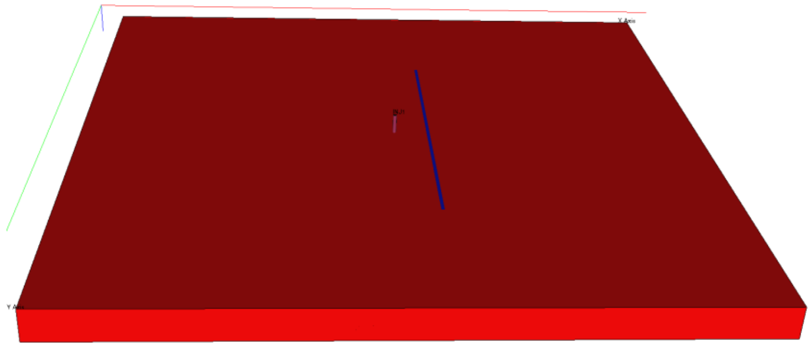

*Figure 4.1 Eclipse model*

Challenges may arise from using numerical reservoir simulation tools, like numerical dispersion and grid block storage. Simulating a continuous phenomenon, such as a water injection, in a numerical simulator which relies on discrete grid blocks, may lead to errors. Physically, in water injection, the fluid/pressure front advances forward for every time step. Numerical flow simulators are unable to distribute pressure and saturations within one single grid cell, which may lead to a premature response of any reservoir feature, like boundaries or discontinuities.

### *4.1.1 Comparing analytical and numerical models*

To evaluate the ability of the numerical simulator, Eclipse, to simulate a well test compared to analytical models in Saphir, the wellbore pressure and pressure derivative response of Eclipse is plotted and compared to that of Saphir in Figure 4.2 a) and b) for the injection and falloff periods respectively.

a) b)

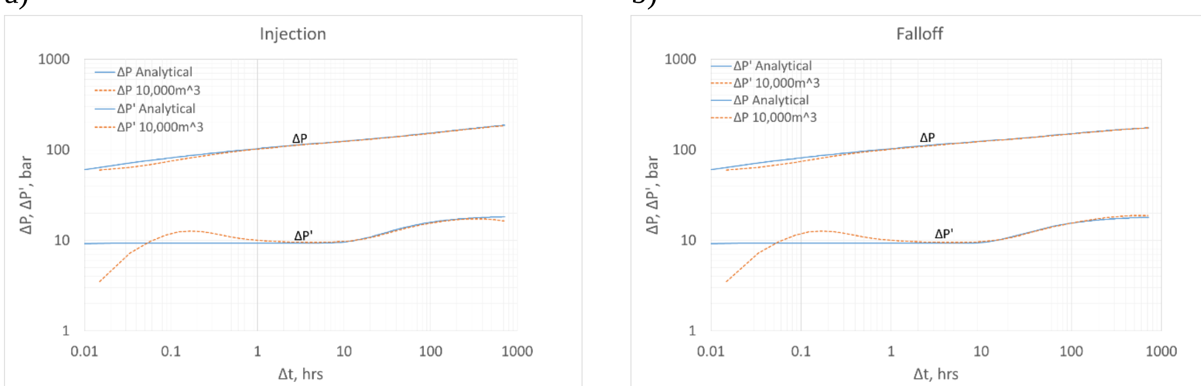


*Figure 4.2 Wellbore pressure and pressure derivative of closed fault response. Analytical vs. numerical model. a) Injection, b) falloff*

At early times, $\Delta t < 0.1\ hrs$, the numerical synthetic pressure derivative results exhibit behaviour like that of a transition between wellbore storage, log-log unit slope, and infinite acting radial flow. This response could be because of grid block storage effects. Later, the response of the closed fault, increase in pressure derivative, is seen. The numerical results show a slightly premature response of the closed fault compared to the analytical model, which can be because of numerical dispersion. To verify that the two mentioned effects, grid block storage and numerical dispersion, is the source of the discrepancy between the wellbore pressure and pressure derivative response, the grid block volume is varied to see if this influences the early time and the closed fault responses. The grid blocks are varied between 2500m$^3$, 10,000m$^3$ and 40,000m$^3$. The pressure derivative responses for both injection and falloff periods are shown in Figure 4.3 a) and b) respectively.

a) b)

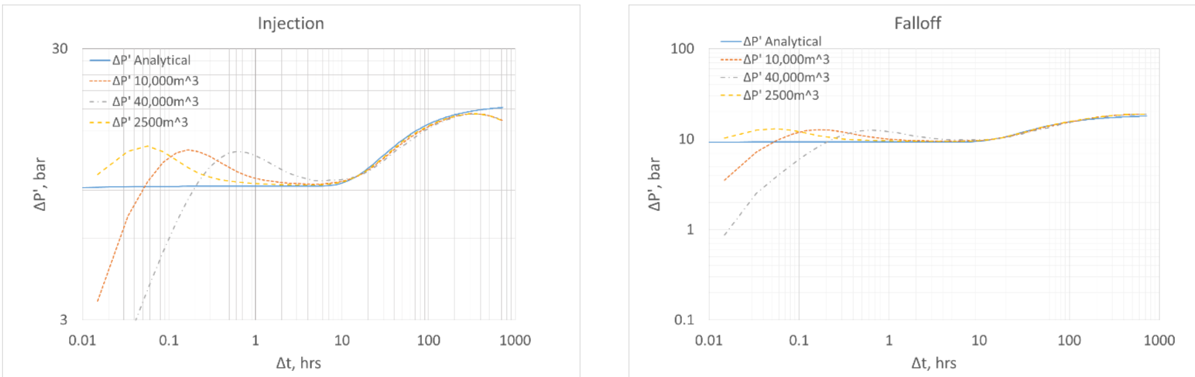


*Figure 4.3 Sensitivity of grid block volume on grid block storage and numerical dispersion.*

As shown in Figure 4.3, the wellbore pressure derivative from the model with the smallest grid blocks, 2500m$^3$, most closely resembles the pressure derivative response of the analytical model. Both coarser models display grid block storage effects somewhat disturbing the response of the closed fault, whilst the transition period between grid block storage and the IARF period ends long before the synthetic derivative response of the fault in the case of the smallest grid blocks. The advantages of running a finely gridded model is a more physical model and better representation of actual, physical flow. The fine grid comes with some disadvantages, as it leads to longer simulation times, especially for large and complex models.

## 4.2 Dynamic fault behaviour

Because of the higher variability in Eclipse to model pressure-dependent transmissibility in multiple directions, it was decided to be the main flow simulator used in this thesis. An Eclipse model, containing a fault with pressure dependent properties, porosity and inter-block transmissibility, was created with the same reservoir parameters as defined for the closed fault case, see **Table 4.1**. The use of the ROCKTAB keyword for pressure dependent transmissibility is discussed in Section 4.2.1 below.

This section concerns fault reactivation by pressure increase. The dynamic fault is located 100m east of the well and is 1000m long. Transmissibility between the fault grid blocks along the fault direction increases exponentially, by using the transmissibility multiplier option in ROCKTAB, defined for the fault grid blocks. Values generated by the permeability modulus formulation was directly inputted into the transmissibility multiplier since constant fault grid block size results in the transmissibility multiplier equalling a permeability multiplier. This is shown in

Section 4.2.2. For the case of an initially conductive fault, with transmissibility increasing with pressure, the fault transmissibility in the y-direction is equal to the matrix transmissibility multiplied the appropriate transmissibility multiplier, whilst the cross-fault transmissibility multiplier is unity for all pressures above initial reservoir pressure.

The permeability (transmissibility) multipliers are calculated by using the concept of permeability modulus as defined in Equation (2.18). Three values of permeability modulus are used: $0.040, 0.160\ and\ 0.280\ bar^{-1}$. For the case of fault reactivation at some pressure, in this case, either 225 or 245 bara, $T_x$ and $T_y$ is zero at pressures lower than what is defined as the "Threshold pressure" in Section 4.

### 4.2.1 Dynamic fault simulation

For dynamic reservoir simulation in Eclipse, the ROCKTAB keyword is used in combination with the RKTRMDIR keyword to allow for a pore volume multiplier and transmissibility multipliers in all three directions for different pressure of defined grid blocks.

To control the transmissibility across grid blocks, an in-effect permeability of the grid blocks, the ROCKTAB keyword contains availability of transmissibility multipliers in three dimensions. The input values of the transmissibility multipliers are included in the transmissibility calculations in the x-, y- and z-directions, depicted in Figure 4.4 below and given by Equations (4.1) and (4.2) (Schlumberger, 2014, p. 962).

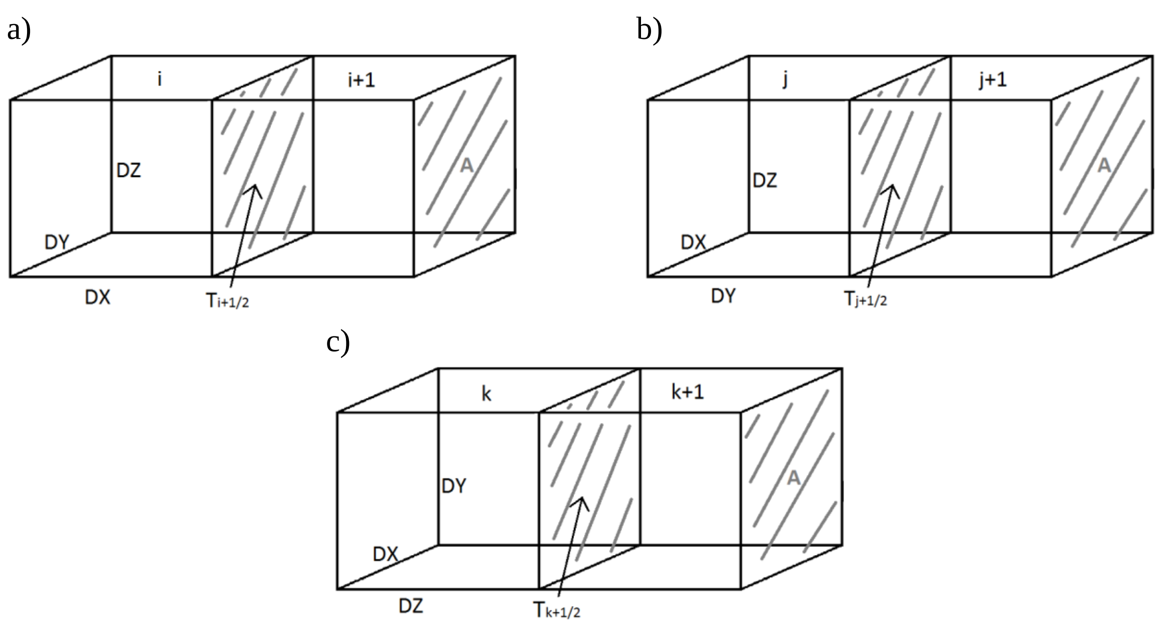


*Figure 4.4 Transmissibility in a)x-direction, b) y-direction, c) z-direction.*

$$T_{i+\frac{1}{2}} = \frac{2 * A}{\frac{DX_i}{PERMX_i} + \frac{DX_{i+1}}{PERMX_{i+1}}} = TRANX \tag{4.1}$$

Or with the transmissibility multiplier option:

$$T_{i+\frac{1}{2}} = \frac{2 * MULTX * A}{\frac{DX_i}{PERMX_i} + \frac{DX_{i+1}}{PERMX_{i+1}}} = MULTX * TRANX \tag{4.2}$$

Note that these equations can also be applied in y- and z-direction, by changing the appropriate variables; $PERMX, DX, TRANX$ and $MULTX$.

Then, defining a closed fault through transmissibility in Eclipse, by using the transmissibility multiplier option, well placement compared to the fault blocks is crucial. If the well is placed at a grid block opposite the closed boundary from the grid block controlling the transmissibility multiplier, these grid blocks are unaffected by the increase of pressure on the left side of the closed block boundary in Figure 4.5.

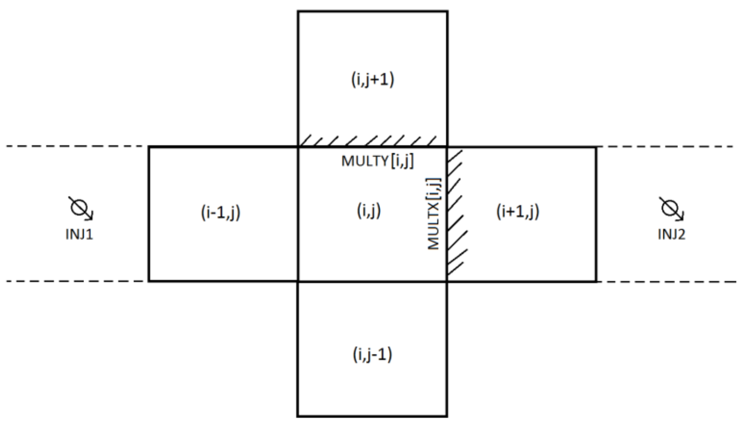


*Figure 4.5 Reservoir grid blocks containing transmissibility multipliers.*

Note that, as the ROCKTAB keyword is defined for the cell (i,j), $MULTX$ and $MULTY$ controls the transmissibility over the boundary (i,j) to (i+1,j) and (i,j) to (i,j+1) or $TRANX$ and $TRANY$ respectively (Schlumberger, 2014). Thereby, if the well is located at (i>i+1,j>j+1) it has no impact on the pressure of the cell (i,j) if the transmissibility multiplier is zero at some initial pressure, i.e. closed fault at the initial pressure. Pressure increase through injection in well 'INJ2' in Figure 4.5 would not increase the pressure in the cell (i,j).

### *4.2.2 Sensitivity of fault block permeability*

To check what value of fault permeability which gives no change in pressure derivative response, the fault block permeabilities are varied, i.e. static fault with different constant permeability of the fault grid blocks for each run. The wellbore pressure derivative response of the different fault permeabilities are given in Figure 4.6 below:

a) b)

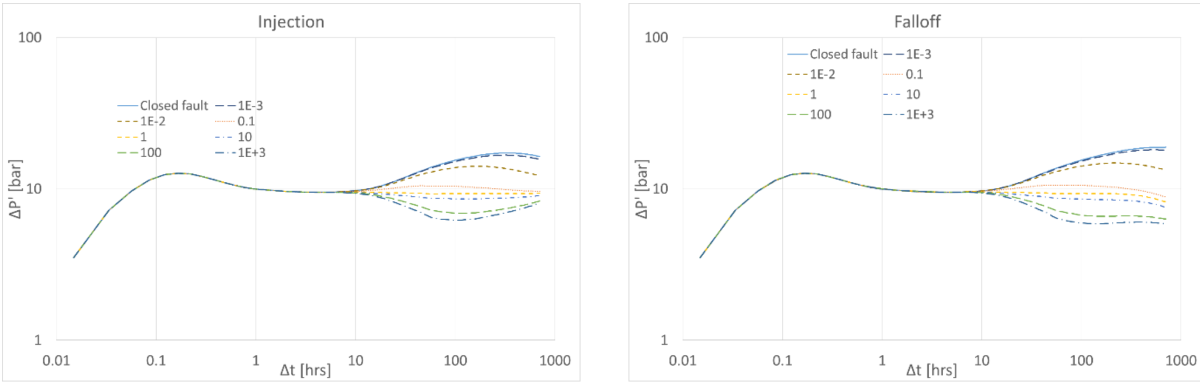


*Figure 4.6 Pressure transient response of different fault block permeability multiplier, $k_{fault}/k_{matrix}$ a) Injection pressure derivative response, b) falloff pressure derivative response*

A closer look at these pressure derivative responses of the fault shows that the pressure derivative does not change at values of fault permeability multiplier > $10^4$, i.e. increasing the fault permeability above $10^5$ mD gives no difference in the pressure derivative response. Also, permeability multipliers < $10^{-4}$ result in pressure derivative response equal to that of the closed fault. This is true for derivative responses of both injection and falloff testing, see Figure 4.7 a) and b) below:

a) b)

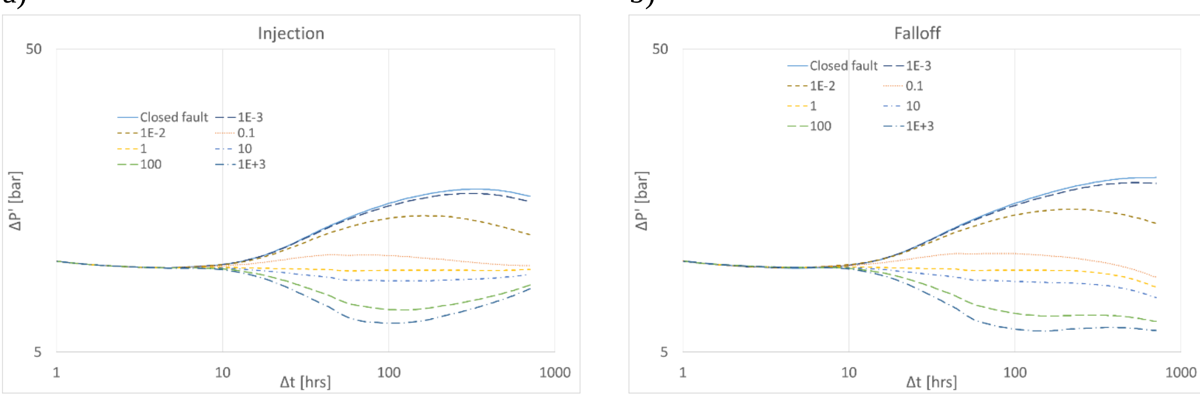


*Figure 4.7 Pressure transient response of different fault block permeability multiplier, $k_{fault}/k_{matrix}$. a) Injection pressure derivative response, b) falloff pressure derivative response*

Because Eclipse does not allow for a permeability multiplier in ROCKTAB, the equivalent value of the transmissibility multipliers, $MULTX$ and $MULTY$, is calculated for x- and y-permeability of $10^5$ mD. The transmissibility between the fault and matrix grid blocks is:

$$T_{[matrix \to fault]} = \frac{2 * A}{\dfrac{DX_{fault}}{PERMX_{fault}} + \dfrac{DX_{matrix}}{PERMX_{matrix}}} \tag{4.3}$$

Where subscripts fault and matrix denotes the appropriate value of the parameter on either side of grid block boundary between the fault and matrix block. Note that the expression of the y- and z-transmissibility, $T_{j+\frac{1}{2}}$ and $T_{k+\frac{1}{2}}$ respectively, is completely analogous to Equation (4.3), with an alteration of X to Y or Z.

The size of the fault grid blocks is 0.64m in the x-direction and 10m in the y-direction, whilst the neighbouring grid blocks are 0.65m in the x-direction and 10m in the y-direction, see Appendix D. The necessary transmissibility, to obtain a permeability of $10^5$ mD of the fault blocks, is:

$$T_{[matrix \to fault]} = \frac{2 * A}{\frac{DX_{matrix}}{PERMX_{matrix}} + \frac{DX_{fault}}{PERMX_{fault}}} = \frac{2 * 10 * 100m^2}{\frac{0.65m}{10mD} + \frac{0.64m}{10^5 mD}} = 3.08 * 10^4 mD.m \tag{4.4}$$

Likewise, for y-direction

$$T_{fault} = \frac{2 * A}{\frac{DY_{fault}}{PERMY_{fault}} + \frac{DY_{fault}}{PERMY_{fault}}} = \frac{2 * 0.64 * 100m^2}{\frac{10m}{10^5 mD} + \frac{10m}{10^5 mD}} = 6.40 * 10^5 mD.m \tag{4.5}$$

Calculating the y-transmissibility of the fault blocks, but with a permeability of 10 mD, gives transmissibility of 64mD.m, i.e. at a transmissibility multiplier of $10^4$ the further increase of $MULTY$, makes no difference in the pressure derivative response. Notice that the x-transmissibility multiplier equals a permeability multiplier if $DX$ and cross-sectional area, $A$, are the same for both matrix and fault grid blocks in the x-direction. The same is true for the y-direction if the fault grid block dimensions are constant for the entire fault.

Based on these observations, three values of the permeability modulus were chosen to represent the cases of fault y-direction transmissibility:

i) Rapidly exceeding this threshold multiplier
ii) Slowly exceeding this threshold multiplier
iii) Never exceeding this threshold multiplier

### 4.2.3 *Transmissibility multipliers:*

The three permeability moduli were chosen to be $\gamma = 0.040, \gamma = 0.160, \gamma = 0.280\ bar^{-1}$, which give a fault transmissibility multiplier respectively never, slowly and rapidly exceeding the threshold multiplier. Three cases of fault reactivation were run with these three permeability moduli, threshold pressure of 200, 225 and 245 bara. Below each respective threshold pressure for each of the cases the x- and y-transmissibility of the fault blocks are 0. Above the threshold pressure, the y-transmissibility multiplier, $MULTY$, is shown in Figure 4.8 below for each threshold pressure and permeability moduli.

a)

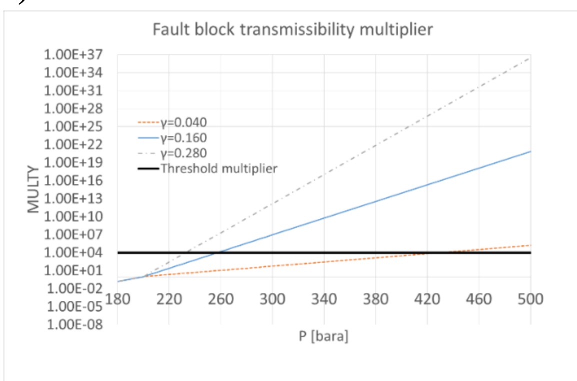


b)

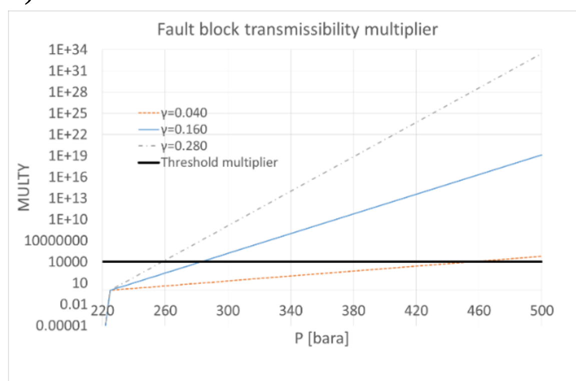


c)

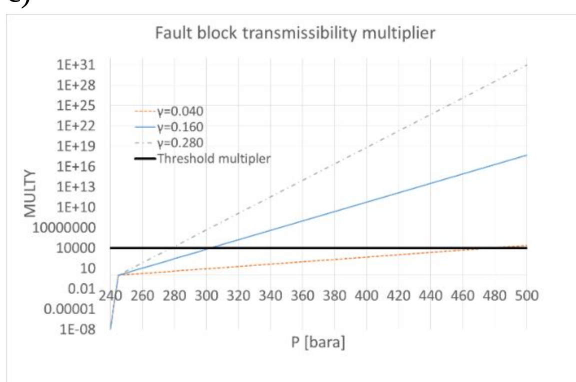


*Figure 4.8 Transmissibility multiplier, MULTY, with threshold pressure of a) 200 bara, b) 225 bara and c) 245 bara.*

### *4.2.4 Threshold pressure of 200 bara*

The transmissibility multiplier given in Figure 4.8 a) is used for transmissibility increase between the fault blocks along the fault direction. The resulting synthetic pressure derivative response is given below in Figure 4.9.

a) b)

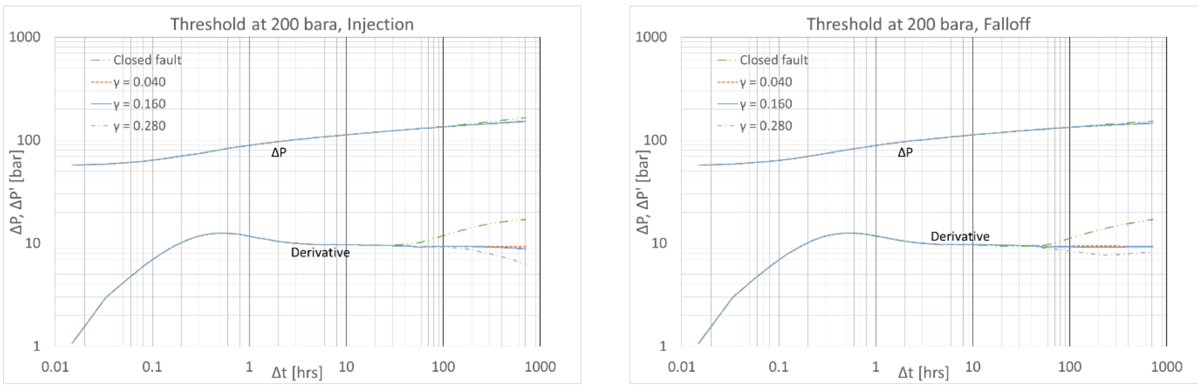


*Figure 4.9 Wellbore pressure and pressure derivative response of closed and dynamic fault. a) injection period, b) falloff period. Threshold pressure 200 bara*

As is shown in the derivative plot, the largest transmissibility change, i.e. $\gamma = 0.280\ bar^{-1}$, deviates from the "Closed fault" curve at a higher rate, [bar/hr], than the other two models. This can resemble the pressure derivative response of a high conductivity zone. The other two models exhibit the same behaviour, but decrease at a slower rate than the case mentioned before. The case of closed fault exhibits the expected behaviour, i.e. increasing pressure derivative.

### *4.2.5 Threshold pressure of 225 bara*

The synthetic wellbore pressure and pressure derivative responses for both the injection and the falloff periods are shown in Figure 4.10 below.

a) b)

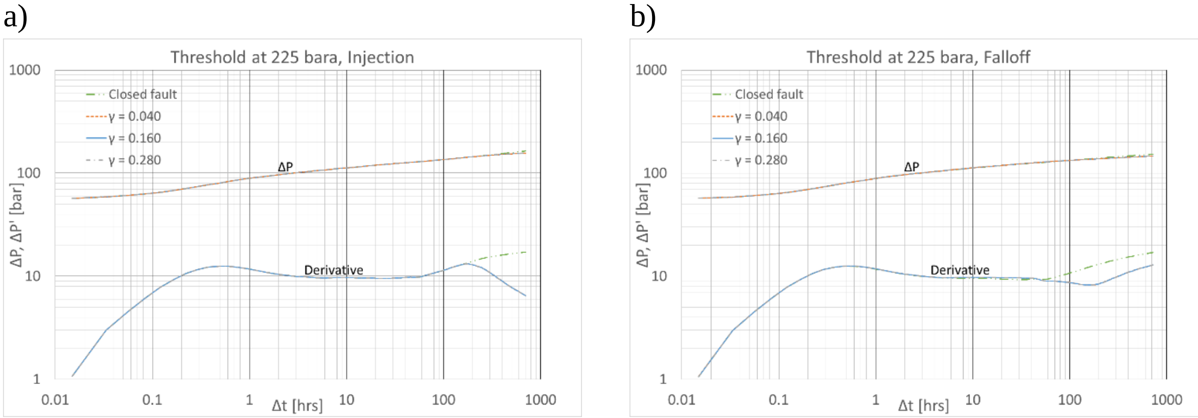


*Figure 4.10 Wellbore pressure and pressure derivative response of closed and dynamic fault. a) injection period, b) falloff period. Threshold pressure 225 bara*

The pressure derivatives of the reactivating fault cases show no significant noticeable differences. Their difference is in the scale of $10^{-2}$ to $10^{-4}$ bar. This is the case for both the injection and the falloff periods. The $\Delta P$ responses exhibit the expected behaviour of both injection and falloff transients.

### *4.2.6 Threshold pressure of 245 bar*

The synthetic wellbore $\Delta P$ and pressure derivative for all cases of permeability moduli for both injection and falloff periods are given in Figure 4.11 below.

a) b)

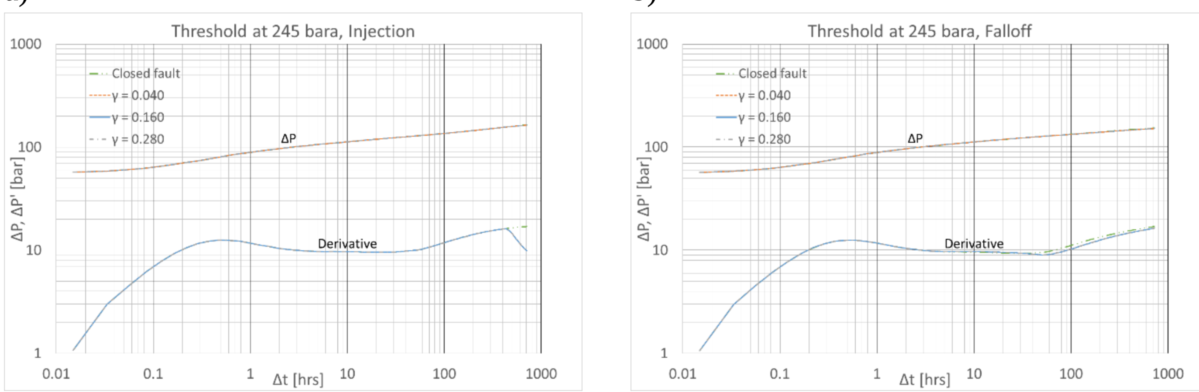


*Figure 4.11 Wellbore pressure and pressure derivative response of closed and dynamic fault. a) injection period, b) falloff period. Threshold pressure 245 bara*

The derivatives for the reactivating fault cases follow the same path as for the closed fault until the threshold pressure is reached. From that point onwards, the derivatives decrease as expected. During the injection period, all cases of reactivating fault with different y-transmissibility show the same values, with differences in the range of only $10^{-4}$ to $10^{-8}$ bar, see Figure 4.11 a). The difference in pressure derivative between the closed fault and the reactivating fault cases during the falloff period is in the range of 0.5 to 1.0 bar, Figure 4.11 b).

### *4.2.7 Injection and Falloff comparison*

To confirm dynamic fault behaviour, it is useful to compare wellbore pressure and -pressure derivative responses for injection and falloff periods (Shchipanov et al., 2011), shown in Figure 4.12.

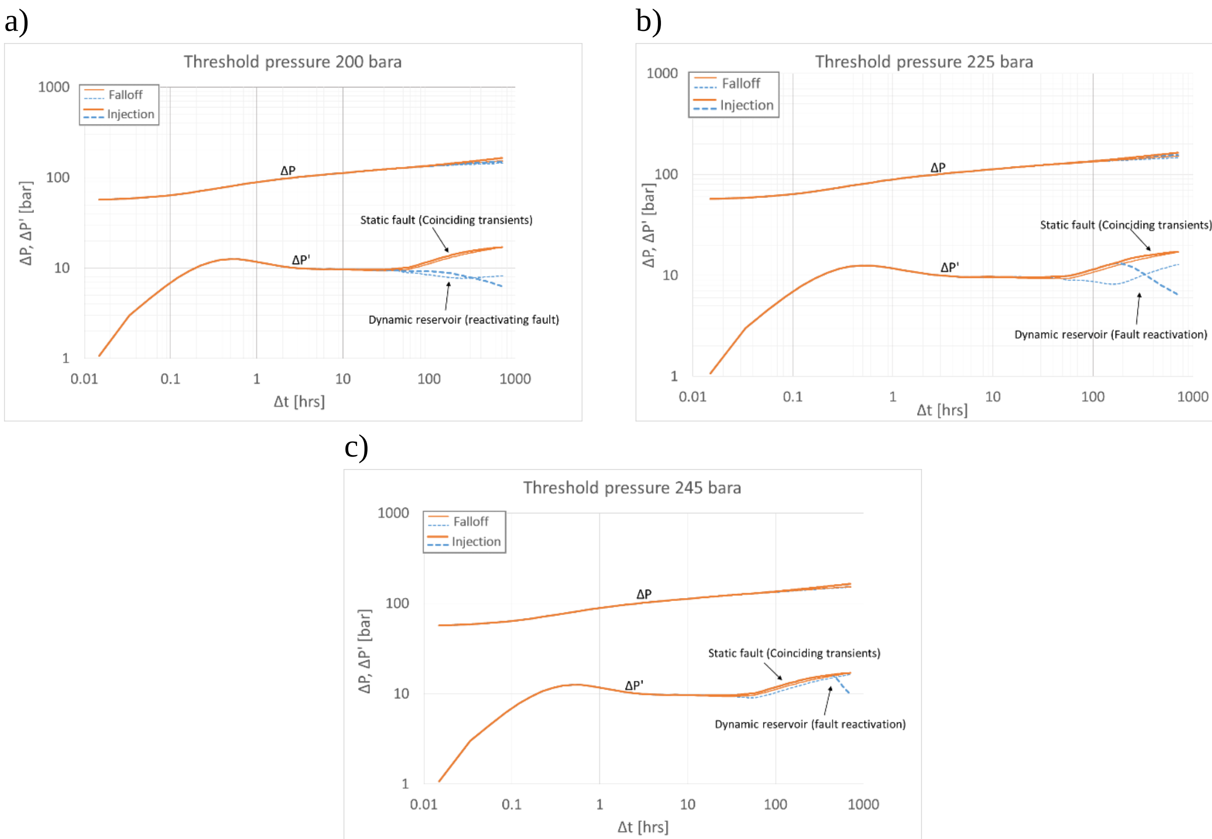


*Figure 4.12 Comparison of falloff and injection pressure transient response. a) Threshold pressure of 200 bara, b) – of 225 bara and c) – of 245 bara. Note that dotted lines are generated by the dynamic fault case.*

For the cases of a static fault, the pressure transients from the injection and the falloff periods coincide after some time, which is evidence of non-dynamic reservoir properties, i.e. a closed fault. In the case of dynamic fault behaviour, i.e. fault reactivation, the transients move in different directions, see Figure 4.12. This behaviour confirms the presence of a dynamic fault.

# 5 Discussion

This chapter is divided into two parts. The first part discusses findings and observations from Chapter 3. Part two takes a closer look into findings from Chapter 4 and aims to explain pressure transient behaviour in the faulted reservoir.

## 5.1 Stress-dependent matrix

Creating a simplified reservoir flow simulator in MS Excel VBA made it possible to test pressure-stress models not available for testing in Eclipse. This model included average pressure, together with changing local (grid block) pressure, as the driver for stress change, which in turn affected permeability which was considered stress-dependent. To include this pressure-stress model in Eclipse would require coupling with a geomechanical simulator.

Assuming uniaxial deformation, looking at the two models of pressure-stress available for testing in Eclipse, i.e. Models (1) and (2). As these models give respectively the upper and lower boundary of effective stress with pressure, see Figure 3.27 a) through c), it can be argued that they can help cover the entire uncertainty range for effects related to geomechanics at under the assumptions mentioned.

As stress affects fault stability, how reservoir stress develops is key to understand fault reactivation potential. A review by Rutqvist (2012) showed that injection of a small fluid plume changed reservoir stress far beyond the extent of the injected plume. Because of this, the inclusion of only local pressure changes in stress formulations may lead to discrepancies. The inclusion of reservoir stress as a function of average reservoir pressure is a huge advantage when considering stress-dependent media.

## 5.2 Dynamic fault behaviour

This thesis showed that for the case of an initially conductive fault, Figure 4.9, the intensity of transmissibility increase was visible in the wellbore pressure derivative response. For the cases of initially closed fault, with a threshold reactivation pressure above initial reservoir pressure, see Figure 4.10 and Figure 4.11, the intensity of the transmissibility increase, or the “slope” of the transmissibility multiplier with pressure gave no visible difference in the wellbore pressure derivative response. This leads us to believe that at least one of the controlling factors are the difference between injection pressure and fault reactivation pressure, at least for this case of fault location and orientation

The literature on the subject of dynamic fault behaviour and Pressure Transient Analysis is limited. Shchipanov et al. (2011) stated that by comparing injection and falloff pressure transient responses, dynamic fault behaviour can be easily observed. This observation was also made in the current thesis, which can be helpful for distinguishing dynamic fault behaviour from static, high conductivity features.

# 6 Conclusions

Part one of this study was aimed at investigating the effects of geomechanics on stress and stress-dependent permeability, under the assumption of uniaxial deformation. We studied a radial reservoir model with stress-dependent permeability and the impact on permeability intensity. Results showed that under the assumption of uniaxial deformation, the models available for testing in the commercial software give the upper and lower stress limits of stress and permeability forecast and it can, therefore, be argued that the two models cover the entire uncertainty range of effective stress and stress-sensitive permeability.

Part two of the study was aimed at investigating dynamic fault behaviour using Pressure Transient Analysis. It involved fault reactivation through pressure increase by water injection into a saline aquifer. One case of an initially conductive fault, with transmissibility increase with pressure increase, and two cases of initially closed fault with transmissibility increase above some threshold pressure, were studied. The main conclusions drawn from this study are:

- Magnitude of transmissibility increase along fault direction seems to not influence pressure derivative response in the case of a threshold pressure above initial reservoir pressure
- An indication of dynamic fault behaviour is easily visible from injection pressure transient monitoring
- Confirmation of dynamic fault behaviour can be found by comparing injection and falloff pressure transient derivative responses. This is especially important for the case of an initially conductive fault, where the wellbore pressure derivative response resembles that of a static high conductivity zone
- It seems like the magnitude between injection pressure and threshold pressure may be the controlling factor for observing the difference between permeability intensity along the fault direction, at least for this case of fault orientation

# 7 Future work

The author has some suggestions on what can be done to expand the knowledge regarding topics of this thesis.

Regarding pressure diffusivity in stress-dependent media, containing stress models by Settari et al. (2005), a suggestion is to study the effect of other boundary conditions than those investigated is this thesis. Another suggestion is to expand the model to include other geomechanical models or possibly couple the radial Eclipse model with a geomechanical model to verify which of the approximations is the most realistic.

Regarding the models developed in Eclipse for fault reactivation, a suggestion is to investigate the effect of hydraulically fractured wells on pressure transient analysis of fault reactivation and cross-fault permeability increase, as fractured wells is a common stimulation technique and may occur during fluid injection. By expanding to $CO_2$ injection, the results can also be used to design well tests for Geological Carbon Storage projects.

It should be noted that this work was inspired by the ongoing studies of $CO_2$ injection carried out at IRIS within the ENOS project[1].

[1] ENOS (Enabling Onshore $CO_2$ storage) The project is funded by the European Union's Horizon 2020 research and innovation programme under grant agreement No. 653718. www.enos-project.eu

# 8 Nomenclature

| **Abbreviation** | **Description** | **Unit** |
|---|---|---|
| DHST | Downhole Shut-in Tool | |
| $DX, DY, DZ$ | Size of grid block in x-, y-, and z-direction | m |
| GCS | Geological Carbon Storage | |
| MULTX | Transmissibility multiplier in x-direction | |
| $MULTY$ | Transmissibility multiplier in y-direction | |
| $MULTZ$ | Transmissibility multiplier in z-direction | |
| $PERMX$ | Permeability in x-direction | mD |
| $PERMY$ | Permeability in y-direction | mD |
| $PERMZ$ | Permeability in z-direction | mD |
| PTA | Pressure Transient Analysis | |
| $TRANX$ | Transmissibility in x-direction | mD.m |
| $TRANY$ | Transmissibility in y-direction | mD.m |
| $TRANZ$ | Transmissibility in z-direction | mD.m |

| **Symbol** | **Description** | **Unit** |
|---|---|---|
| $A$ | Cross-sectional area | $m^2$ |
| $B$ | Formation volume factor | $m^3/Sm^3$ |
| $C$ | Cohesion | bara |
| $c_l$ | Compressibility of fluid | $bar^{-1}$ |
| $c_r$ | Compressibility of formation | $bar^{-1}$ |
| $h$ | Height | m |
| $k$ | Permeability | mD |
| $k(P)$ | Effective permeability | mD |
| $k_0$ | Initial permeability | mD |
| $m(P)$ | Pseudo-pressure | bar/Pa.s |
| $n_r$ | Number of radial grid cells | |
| $P$ | Pressure | bara |
| $q$ | Volume rate | $m^3/s$ |
| $R$ | Arbitrary point | |
| $r$ | Radius | m |
| $S$ | Skin factor | |
| $t$ | Time | hrs |
| $T$ | Transmissibility | mD.m |
| $V_{b,i}$ | Bulk volume of grid block i | $m^3$ |
| $\Delta P'$ | Pressure derivative | bara |

| Greek letter | Description | Unit |
|---|---|---|
| $\alpha$ | Biot constant | |
| $\gamma$ | Permeability modulus | $bar^{-1}$ |
| $\theta$ | Angle | rad |
| $\mu$ | Viscosity | Pa.s |
| $\mu(P)$ | Effective viscosity | Pa.s |
| $\mu_f$ | Coefficient of friction | |
| $\nu$ | Poisson's ratio | |
| $\rho(P)$ | Effective fluid density | $kg/m^3$ |
| $\sigma$ | Stress | bara |
| $\sigma^0$ | Initial stress | bara |
| $\sigma_n$ | Stress normal to fault plane | bara |
| $\tau$ | Shear stress | bara |
| $\varphi$ | Porosity | |
| $\varphi(P)$ | Effective rock porosity | |

| Sub- and Superscripts | Description | Unit |
|---|---|---|
| 0 | Initial | |
| 10 | Base-10 logarithm | |
| avg | Average | |
| bound,i | Inner boundary condition | |
| bound,o | Outer boundary condition | |
| c | Capillary | |
| const | Constant | |
| crit | Critical | |
| H | Maximum horizontal | |
| h | Minimum horizontal | |
| l | Liquid | |
| m | Mean | |
| matrix | Matrix | |
| n | Normal | |
| Out | Rate, outer boundary | |
| pore | Pore | |
| t | Total | |
| V | Vertical | |
| w | Well | |
| x | x-direction | |
| y | y-direction | |
| z | z-direction | |

# 9 References


Abou-Kassem, J. H., Farouq Ali, S. M., & Islam, M. R. (2006). *Petroleum Reservoir Simulation : a Basic Approach*. Houston, Tex: Gulf Publ. Co.

Adams, B. H. (1983). *Stress-Sensitive Permeability in a High-Permeability Sandstone Reservoir-The Kuparuk Field*. Paper presented at the SPE California Regional Meeting, Ventura, California.

Aziz, K., & Settari, A. (1979). *Petroleum reservoir simulation*. London: Applied Science Pub.

Bagheri, M., & Settari, A. (2005). *Modeling of Geomechanics in Naturally Fractured Reservoirs*. Paper presented at the SPE Reservoir Symposium, The Woodlands, Texas.

Bagheri, M., & Settari, A. (2008). *Modeling Coupled Fluid Flow and Deformation of Fractured Reservoirs Using Full Tensor Permeability*. Paper presented at the Europec/EAGE Conference and Exhibition, Rome, Italy.

Bourdarot, G. (1998). *Well testing: Interpretation methods*: Paris: Editions Technip.

Bourdet, D. (2002). *Well test analysis : the use of advanced interpretation models* (Vol. 3). Amsterdam: Elsevier.

Chaudhry, A. (2004). *Oil Well Testing Handbook*: Elsevier.

Choi, J., Skurtveit, E., Bohloli, B., & Grande, L. (2015). *Geomechanical Assessment of Flow Barriers Observed from 4D Time-lapse Survey for CO2 Storage in Snøhvit Field.* Paper presented at the Fourth International Conference on Fault and Top Seals.

Committee on Fracture Characterization and Fluid Flow. (1996). *Rock Fractures and Fluid Flow: Contemporary Understanding and Applications*: National Academies Press.

Ertekin, T., Abou-Kassem, J. H., & King, G. R. (2000). *Basic Applied Reservoir Simulation* (Vol. v.7). Richardson: Society of Petroleum Engineers.

Faulkner, D. R., Jackson, C. A. L., Lunn, R. J., Schlische, R. W., Shipton, Z. K., Wibberley, C. A. J., & Withjack, M. O. (2010). A review of recent developments concerning the structure, mechanics and fluid flow properties of fault zones. *Journal of Structural Geology, 32*(11), 1557-1575. doi:http://dx.doi.org/10.1016/j.jsg.2010.06.009

Fjær, E., Holt, R. M., Raaen, A., Risnes, R., & Horsrud, P. (2008). *Petroleum Related Rock Mechanics* (2nd ed. Vol. 53): Elsevier.

Gan, Q., & Elsworth, D. (2014). Analysis of fluid injection-induced fault reactivation and seismic slip in geothermal reservoirs. *Journal of Geophysical Research: Solid Earth, 119*(4), 3340-3353.

Horne, R. N. (1995). *Modern Well Test Analysis : a Computer-aided Approach* (2nd ed.). Palo Alto, Calif: Petroway.

Johnson, C. R., Greenkorn, R. A., & Woods, E. G. (1966). Pulse-Testing: A New Method for Describing Reservoir Flow Properties Between Wells. doi:10.2118/1517-PA

Kim, W.-Y. (2013). Induced seismicity associated with fluid injection into a deep well in Youngstown, Ohio. *Journal of Geophysical Research: Solid Earth, 118*(7), 3506-3518. doi:10.1002/jgrb.50247

Knipe, R. J., Jones, G., & Fisher, Q. (1998). Faulting, fault sealing and fluid flow in hydrocarbon reservoirs: an introduction. *Geological Society, London, Special Publications, 147*(1), vii-xxi.

Kuchuk, F., Biryukov, D., & Fitzpatrick, T. (2015). Fractured-reservoir modeling and interpretation. *SPE Journal, 20*(05), 983-981,004.

Kulikowski, D., Amrouch, K., & Cooke, D. (2016). Geomechanical modelling of fault reactivation in the Cooper Basin, Australia. *Australian Journal of Earth Sciences, 63*(3), 295-314. doi:10.1080/08120099.2016.1212925

Lee, W. (2011). Tridiagonal matrices: Thomas algorithm. *MS6021, Scientific Computation, University of Limerick*.

Majer, E. L., Baria, R., Stark, M., Oates, S., Bommer, J., Smith, B., & Asanuma, H. (2007). Induced seismicity associated with Enhanced Geothermal Systems. *Geothermics, 36*(3), 185-222. doi:https://doi.org/10.1016/j.geothermics.2007.03.003

Mazzoldi, A., Rinaldi, A. P., Borgia, A., & Rutqvist, J. (2012). Induced seismicity within geological carbon sequestration projects: Maximum earthquake magnitude and leakage potential from undetected faults. *International Journal of Greenhouse Gas Control, 10*, 434-442. doi:http://dx.doi.org/10.1016/j.ijggc.2012.07.012

Nacht, P. K., De Oliveira, M., Roehla, D., & Costa, A. (2010). Investigation of geological fault reactivation and opening. *Association Argentina de Mecanica Computacional, Eduardo Dvorkin, Marcela Goldschmit, Mario Storti (Eds.), Buenos Aires, Aergentina, 29*.

Ostensen, R. W. (1986). The Effect of Stress-Dependent Permeability on Gas Production and Well Testing. doi:10.2118/11220-PA

Pedrosa, O. A., Jr. (1986). *Pressure Transient Response in Stress-Sensitive Formations*.

Pei, Y., Paton, D. A., Knipe, R. J., & Wu, K. (2015). A review of fault sealing behaviour and its evaluation in siliciclastic rocks. *Earth-Science Reviews*, *150*, 121-138.

Pinzon, C. L., Chen, H.-Y., & Teufel, L. W. (2000). *Complexity of Well Testing Analysis of Naturally-Fractured Gas-Condensate Wells in Colombia*.

Pinzon, C. L., Chen, H.-Y., & Teufel, L. W. (2001). *Numerical Well Test Analysis of Stress-Sensitive Reservoirs*.

Raghavan, R., Scorer, J. D. T., & Miller, F. G. (1972). An Investigation by Numerical Methods of the Effect of Pressure-Dependent Rock and Fluid Properties on Well Flow Tests. doi:10.2118/2617-PA

Rutqvist, J. (2012). The Geomechanics of CO2 Storage in Deep Sedimentary Formations. *Geotechnical and Geological Engineering, 30*(3), 525-551. doi:10.1007/s10706-011-9491-0

Rutqvist, J., Birkholzer, J., Cappa, F., & Tsang, C. F. (2007). Estimating maximum sustainable injection pressure during geological sequestration of CO2 using coupled fluid flow and geomechanical fault-slip analysis. *Energy Conversion and Management, 48*(6), 1798-1807. doi:http://dx.doi.org/10.1016/j.enconman.2007.01.021

Rutqvist, J., Cappa, F., Rinaldi, A. P., & Godano, M. (2014a). Dynamic modeling of injection-induced fault reactivation and ground motion and impact on surface structures and human perception. *Energy Procedia, 63*, 3379-3389. doi:http://dx.doi.org/10.1016/j.egypro.2014.11.367

Rutqvist, J., Cappa, F., Rinaldi, A. P., & Godano, M. (2014b). Modeling of induced seismicity and ground vibrations associated with geologic CO2 storage, and assessing their effects on surface structures and human perception. *International Journal of Greenhouse Gas Control, 24*, 64-77. doi:http://dx.doi.org/10.1016/j.ijggc.2014.02.017

Rutqvist, J., Rinaldi, A. P., Cappa, F., & Moridis, G. J. (2013). Modeling of fault reactivation and induced seismicity during hydraulic fracturing of shale-gas reservoirs. *Journal of Petroleum Science and Engineering, 107*, 31-44. doi:http://dx.doi.org/10.1016/j.petrol.2013.04.023

Samaniego, F., & Cinco-Ley, H. (1989). *On the Determination of the Pressure-Dependent Characteristics of a Reservoir Through Transient Pressure Testing*.

Samaniego V, F., Brigham, W. E., & Miller, F. G. (1977). An Investigation of Transient Flow of Reservoir Fluids Considering Pressure-Dependent Rock and Fluid Properties. doi:10.2118/5593-PA

Samaniego, V. F., & Villalobos, L. H. (2003). Transient pressure analysis of pressure-dependent naturally fractured reservoirs. *Journal of Petroleum Science and Engineering, 39*(1–2), 45-56. doi:http://dx.doi.org/10.1016/S0920-4105(03)00039-1

Schlumberger. (2014). Eclipse Technical Description.

Settari, A. T., Bachman, R. C., & Walters, D. A. (2005). *How To Approximate Effects of Geomechanics in Conventional Reservoir Simulation*. Paper presented at the SPE Annual Technical Conference and Exhibition, Dallas, Texas.

Shchipanov, A. (2017). [Personal communication].

Shchipanov, A., Kollbotn, L., Berenblyum, R., & Surguchev, L. (2011). *How to Account for Dynamic Fracture Behaviour in Reservoir Simulation.* Paper presented at the EAGE Workshop on Naturally and Hydraulically Induced Fractured Reservoirs–From NanoDarcies to Darcies.

Shchipanov, A., Kollbotn, L., Surguchev, L. M., & Thomas, K. O. (2010). *A New Approach to Deformable Fractured Reservoir: Case Study of the Ekofisk Field*. Paper presented at the SPE EUROPEC/EAGE Annual Conference and Exhibition, Barcelone, Spain.

Shipton, Z. K., Soden, A. M., Kirkpatrick, J. D., Bright, A. M., & Lunn, R. J. (2006). How thick is a fault? Fault displacement-thickness scaling revisited. *Earthquakes: Radiated energy and the physics of faulting*, 193-198.

Skinner, B. J., Porter, S. C., & Park, J. (2004). *The dynamic earth : an introduction to physical geology* (5th ed. ed.). New York: Wiley.

Thomas, L. H. (1949). Elliptic problems in linear difference equations over a network. *Watson Sci. Comput. Lab. Rept., Columbia University, New York, 1*.

Vairogs, J., Hearn, C. L., Dareing, D. W., & Rhoades, V. W. (1971). Effect of Rock Stress on Gas Production From Low-Permeability Reservoirs. doi:10.2118/3001-PA

Vairogs, J., & Rhoades, V. W. (1973). Pressure Transient Tests in Formations Having Stress-Sensitive Permeability. doi:10.2118/4050-PA

Yilmaz, O., Nur, A., & Nolen-Hoeksema, R. (1991). Pore Pressure Profiles in Fractured and Compliant Rooks: Society of Petroleum Engineers.

Zhang, M. Y., & Ambastha, A. K. (1994). *New Insights in Pressure-Transient Analysis for Stress-Sensitive Reservoirs*.

Zoback, M. D., & Zinke, J. C. (2002). Production-induced Normal Faulting in the Valhall and Ekofisk Oil Fields. *pure and applied geophysics, 159*(1), 403-420. doi:10.1007/pl00001258

# 10 Appendix

## Appendix A – Implicit pressure solver

Below is the scheme template used for simulating radial flow in this thesis discussed in Section 3.2

**Radial geometry**

Considering Darcy's law:

$$q = A\frac{k}{\mu}\frac{\partial P}{\partial r} \tag{A.1a}$$

Which results in the following:

$$q = \frac{2\pi\beta_c kh(P_w - P_e)}{\mu B\left(log_e\left(\frac{r_w}{r_e}\right) + S\right)} \tag{A.1b}$$

Where

- $\beta_c$ = unit conversion factor
- q = volume rate
- k = permeability
- h = pay thickness
- P = pressure
- μ = phase viscosity
- B = formation volume factor
- r = radius
- S = skin factor
- Subscripts w and e refer to well and external respectively

Then considering a control volume:

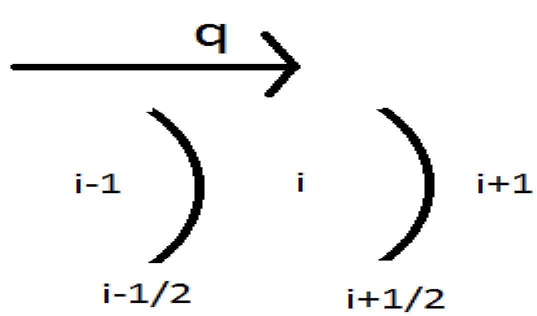


*Figure A. 1 Control volume*

Here the volume rate amount to:

$$q_{i+\frac{1}{2}} = \frac{2\pi\beta_c (kh)_{i+\frac{1}{2}}(P_i - P_{i+1})}{\mu B\left(log_e\left(\frac{r_i}{r_{i+1}}\right)\right)} \tag{A.2}$$

Subscripts i-1, i-1/2, i, i + ½, i+1 refer to where the respective parameter i.e. pressure, radius, permeability etc., should be evaluated.

Since permeability and height are evaluated at the interface i+½ there is a need to average the permeability-thickness product at this interface. This product is averaged harmonically by the following formulae

$$(kh)_{1+\frac{1}{2}} = \frac{1}{\frac{log_e\left(\frac{r_{i+\frac{1}{2}}}{r_i}\right)}{(kh)_i} + \frac{log_e\left(\frac{r_{i+1}}{r_{i+\frac{1}{2}}}\right)}{(kh)_{i+1}}} \tag{A.3}$$

Defining the transmissibility at this interface:

$$T_{i+\frac{1}{2}} = \frac{G_{i+1/2}}{\mu B} \tag{A.4}$$

Where $T_{i+1/2}$ is the transmissibility and $G_{i+1/2}$ is the geometrical factor at the interface $r_{i+1/2}$ defined by Abou-Kassem et al. (2006) as

$$G_{i+\frac{1}{2}} = \frac{2\pi\beta_c}{(kh)_{i+\frac{1}{2}}} \tag{A.5}$$

This gives Darcy's law, on finite difference formulation, as:

$$q_{i+\frac{1}{2}} = T_{i+\frac{1}{2}}(P_i - P_{i+1}) \tag{A.6a}$$

Likewise, for inflow;

$$q_{i-\frac{1}{2}} = T_{i-\frac{1}{2}}(P_{i-1} - P_i) \tag{A.6b}$$

Where

$$T_{i-\frac{1}{2}} = \frac{2\pi\beta_c}{\mu B\left[\frac{log_e\left(\frac{r_i}{r_{i-\frac{1}{2}}}\right)}{(kh)_i} + \frac{log_e\left(\frac{r_{i-\frac{1}{2}}}{r_{i-1}}\right)}{(kh)_{i-1}}\right]} \tag{A.7}$$

$r_{i\pm1/2}$ is logarithmically averaged by using the following formulae:

$$r_{i+\frac{1}{2}} = \frac{r_{i+1} - r_i}{log_e\left(\frac{r_{i+1}}{r_i}\right)} \, and \, r_{i-\frac{1}{2}} = \frac{r_i - r_{i-1}}{log_e\left(\frac{r_i}{r_{i-1}}\right)} \tag{A.8}$$

In cases of either damaged or stimulated wells, resulting in a respectively positive or negative skin factor, the effective wellbore radius formulation is used as:

$$r_{w,eff} = r_w e^{-S} \tag{A.9}$$

Points representing gridblocks are spaced such that the pressure drop within the grid block is equal for all blocks. The block-centre radii is then given by Ertekin, Abou-Kassem, & King (2000)

$$r_1 = [\alpha_{lg} \log_e \alpha_{lg} / (\alpha_{lg} - 1)] r_w \quad \text{(A.10a)}$$

And subsequent

$$r_i = r_{i-1}\alpha_{lg}, i = 2, 3, \ldots, n_r \quad \text{(A.10b)}$$

Where $\alpha_{lg} = \left(\frac{r_e}{r_w}\right)^{\frac{1}{n_r}}$

Where $n_r$ is the number or grid blocks.

For complete derivations of $r_1$, $r_i$ and $\alpha_{lg}$ please see the book by Ertekin et al. (2000)

Now consider a discretized reservoir, divided into $n_r$ number of grid blocks, each of volume

$$V_{b,i} = \pi h \left(r^2_{i+\frac{1}{2}} - r^2_{i-\frac{1}{2}}\right)$$

Where $V_{b,i}$ is the bulk volume of grid block i

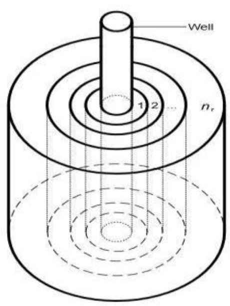


*Figure A. 2 Discretized reservoir model*

To evaluate the flow problem in full, initial and boundary conditions need to be defined. Different combinations of inner and outer boundary conditions are shown in Section 3.2.

*Initial condition:*

$$P(r, t = 0) = P_{init} \quad \text{(A.12a)}$$

*Boundary conditions:*

$$q(r_w, t) = Q_{const}, constant\ rate\ inner\ boundary \quad \text{(A.12b)}$$

$$q(r_e, t) = 0, closed\ outer\ boundary \quad \text{(A.12c)}$$

$$P(r = r_w, t) = P_{Bound,i}, constant\ pressure\ inner\ boundary \quad \text{(A.12d)}$$

$$P(r = r_e, t) = P_{Bound,o}, constant\ pressure\ outer\ boundary \quad \text{(A.12e)}$$

The flow equations derived above changes somewhat when considering the case of constant pressure boundaries. Considering Darcy's law

$$q = \frac{2\pi\beta_c kh(P_b - P_{bB})}{\mu B \, log_e\left(\frac{r_b}{r_{bB}}\right)} = T_{b,bB}(P_b - P_{bB}) \tag{A.13}$$

Where

- $T_{b,bB} = \frac{2\pi\beta_c}{\mu B \frac{log_e\left(\frac{r_w}{r_{bB}}\right)}{k_{bB}h_{bB}}}$ is the transmissibility between the reservoir boundary and the point representing the boundary block centre. For derivation, see Abou-Kassem et al. (2006, pg.78-79)
- Subscripts b and bB are related to the boundary and the centre of the boundary grid block respectively

**Scheme formulation:**

To avoid issues regarding instability because of time step restriction, the scheme is fully implicit, i.e. all pressures, except in $\frac{\partial P}{\partial t}$ are evaluated at time step n+1.

***Inner grid blocks,*** $\mathrm{i} = 2, 3, \dots, \mathrm{n_r} - 1$

The mass balance problem for the inner grid blocks are shown in Figure A. 3 below.

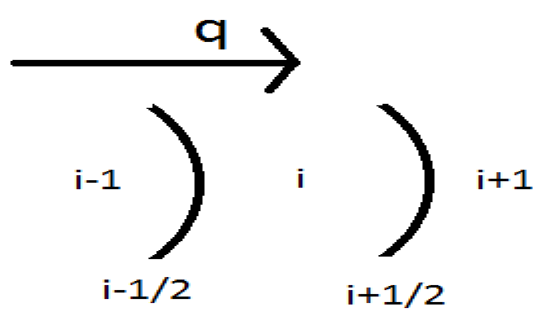


*Figure A. 3 Control volume, inner bridblocks*

$$mass\ in - mass\ out = accumulation \tag{A.14a}$$

$$(q\rho)_{i-1/2}^{n+1} - (q\rho)_{i+\frac{1}{2}}^{n+1} = \frac{(\varphi\rho)_i^{n+1} - (\varphi\rho)_i^n}{\Delta t} V_{b,i} \tag{A.14b}$$

Flow equations, Darcy's law at inflow and outflow interfaces:

$$q_{i+\frac{1}{2}}^{n+1} = T_{i+\frac{1}{2}}\left(P_i^{n+1} - P_{i+1}^{n+1}\right) \tag{A.15a}$$

$$q_{i-\frac{1}{2}}^{n+1} = T_{i-\frac{1}{2}}\left(P_{i-1}^{n+1} - P_i^{n+1}\right) \tag{A.15b}$$

RHS of B14b) then becomes:

$$\rho T^n_{i-\frac{1}{2}}\left(P^{n+1}_{i-1} - P^{n+1}_i\right) - \rho T^n_{i+\frac{1}{2}}\left(P^{n+1}_i - P^{n+1}_{i+1}\right) \tag{A.16}$$

As $\Delta t \rightarrow 0$, LHS can be approximated to the derivative: $\frac{\mathrm{d}(\varphi\rho)}{\mathrm{dt}}$

By using the definitions of compressibility

$$c_l = \frac{1}{\rho}\frac{d\rho}{dP} = \frac{1}{\rho}\frac{d\rho}{dt}\frac{dt}{dP} \rightarrow \frac{d\rho}{dt} = c_l\rho\frac{dP}{dt} \tag{A.17a}$$

$$c_r = \frac{1}{\varphi}\frac{d\varphi}{dP} = \frac{1}{\varphi}\frac{d\varphi}{dt}\frac{dt}{dP} \rightarrow \frac{d\varphi}{dt} = c_r\varphi\frac{dP}{dt} \tag{A.17b}$$

- $c_r$ and $c_l$ = compressibility of rock and fluid respectively
- $\varphi$ and $\rho$ are the rock porosity and fluid density respectively

By using the chain rule:

$$\frac{d(\varphi\rho)}{dt} = \varphi\frac{d\rho}{dt} + \rho\frac{d\varphi}{dt} \tag{A.17c}$$

And finally, using the definitions of compressibility:

$$\frac{d(\varphi\rho)}{dt} = \varphi c_l\rho\frac{dP}{dt} + \rho c_r\varphi\frac{dP}{dt} = \varphi\rho(c_l + c_r)\frac{dP}{dt} \tag{A.17d}$$

Combining LHS and RHS gives:

$$\rho T^n_{i-\frac{1}{2}}\left(P^{n+1}_{i-1} - P^{n+1}_i\right) - \rho T^n_{i+\frac{1}{2}}\left(P^{n+1}_i - P^{n+1}_{i+1}\right) = \frac{\varphi\rho(c_l + c_r)(P^{n+1}_i - P^n_i)}{\Delta t}V_{b,i} \tag{A.18a}$$

Which gives:

$$T^n_{i-\frac{1}{2}}P^{n+1}_{i-1} - P^{n+1}_i\left(T^n_{i-\frac{1}{2}} + T^n_{i+\frac{1}{2}} + \frac{\varphi(c_l + c_r)V_{b,i}}{\Delta t}\right) + T^n_{i+\frac{1}{2}}P^{n+1}_{i+1} = -\frac{\varphi(c_l + c_r)V_{b,i}}{\Delta t}P^n_i \tag{A.18b}$$

***Inner boundary,*** $\mathrm{i} = 1$

*Constant rate*

The inner boundary condition, as given in equation B12b) is a constant rate condition, as shown in Figure A. 4:

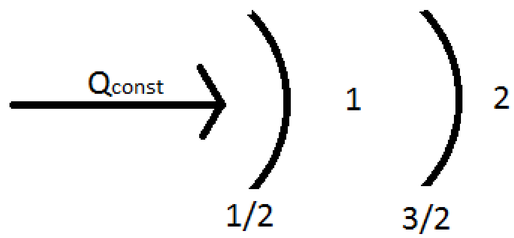


*Figure A. 4 Control volume, inner constant rate condition*

$$mass\ in - mass\ out = accumulation \tag{A.14a}$$

$$(\rho q)^{n+1}_{\frac{1}{2}} - (\rho q)^{n+1}_{\frac{3}{2}} = \frac{(\rho\varphi)^{n+1}_{1} - (\rho\varphi)^{n}_{1}}{\Delta t} V_{b,1} \tag{A.19}$$

By using the same equations that gave A18b), A19) becomes:

$$Q_{const} - T^{n}_{\frac{3}{2}}(P^{n+1}_{1} - P^{n+1}_{2}) = \frac{P^{n+1}_{1} - P^{n}_{1}}{\Delta t}\varphi(c_l + c_r)V_{b,1} \tag{A.20a}$$

$$-P^{n+1}_{1}\left(T^{n}_{\frac{3}{2}} + \frac{\varphi(c_l + c_r)V_{b,1}}{\Delta t}\right) + T^{n}_{\frac{3}{2}}P^{n+1}_{2} = -\left(Q_{const} + \frac{\varphi(c_l + c_r)V_{b,1}}{\Delta t}P^{n}_{1}\right) \tag{A.20b}$$

*Constant pressure*

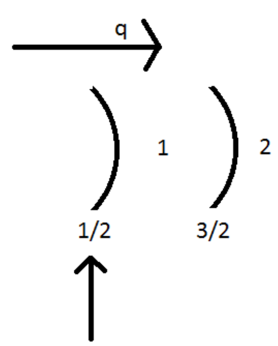


*Figure A. 5 Control volume, constant inner pressure boundary*

$$mass\ in - mass\ out = accumulation \tag{A.14a}$$

$$(q\rho)^{n+1}_{\frac{1}{2}} - (q\rho)^{n+1}_{\frac{3}{2}} = \frac{\varphi\rho^{n+1}_{2} - \varphi\rho^{n}_{2}}{\Delta t} V_{b,1} \tag{A.21}$$

By using the equation that gave A.18a) and 20a), (A.21) becomes:

$$T^n_{\frac{1}{2}}\left(P_{Bound,i} - P_1^{n+1}\right) - T^n_{\frac{3}{2}}\left(P_1^{n+1} - P_2^{n+1}\right) = \frac{\varphi(c_l + c_r)V_{b,1}}{\Delta t}\left(P_1^{n+1} - P_1^n\right) \qquad \text{(A.22a)}$$

$$P_1^{n+1}\left[-\left(T^n_{\frac{1}{2}} + T^n_{\frac{3}{2}} + \frac{\varphi(c_l + c_r)V_{b,1}}{\Delta t}\right)\right] + T^n_{\frac{3}{2}}P_2^{n+1} = -[T^n_{\frac{1}{2}}P_{Bound,i} + \frac{\varphi(c_l + c_r)V_{b,1}}{\Delta t}P_1^n \qquad \text{(A.22b)}$$

Where $T_{\frac{1}{2}} = T_{b,bB}$ at boundary $i = \frac{1}{2}$and $P_{Bound,i}$is the internal constant boundary pressure

***Outer boundary, i=$n_r$***

*Constant rate outer boundary*

Considering a constant rate outer boundary:

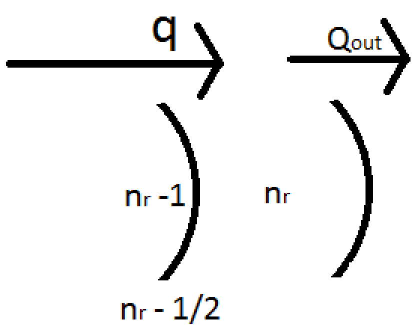


*Figure A. 6 Control volume, constant outer boundary rate*

$$mass\ in - mass\ out = accumulation \qquad \text{(A.14a)}$$

$$(\rho q)^{n+1}_{n_r - \frac{1}{2}} - (\rho Q_{out})^{n+1}_{n_r + \frac{1}{2}} = \frac{(\varphi\rho)^{n+1}_{n_r} - (\varphi\rho)^n_{n_r}}{\Delta t}V_{b,n_r} \qquad \text{(A.23)}$$

By using the same equations that gave A.18a), 20a) and 22a), A.23) becomes

$$T^n_{n_r - \frac{1}{2}}\left(P^{n+1}_{n_r - 1} - P^{n+1}_{n_r}\right) - Q_{out} = \frac{\varphi(c_l + c_r)V_{b,n_r}}{\Delta t}\left(P^{n+1}_{n_r} - P^n_{n_r}\right) \qquad \text{(A.24a)}$$

$$T^n_{n_r - \frac{1}{2}}P^{n+1}_{n_r - 1} + P^{n+1}_{n_r}\left[-\left(T^n_{n_r - \frac{1}{2}} + \frac{\varphi(c_l + c_r)V_{b,n_r}}{\Delta t}\right)\right] = -\frac{\varphi(c_l + c_r)V_{b,n_r}}{\Delta t}P^n_{n_r} + Q_{out} \qquad \text{(A.24b)}$$

Note that a closed outer boundary corresponds to $Q_{out} = 0$

*Constant pressure outer boundary*

Considering a constant pressure outer boundary:

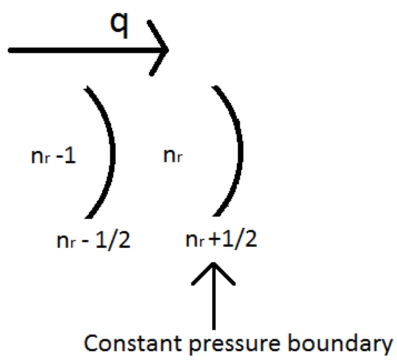


*Figure A. 7 Control volume, constant outer boundary pressure*

$$mass\ in - mass\ out = accumulation \tag{A.14a}$$

$$(\rho q)^{n+1}_{n_r-\frac{1}{2}} - (\rho q)^{n+1}_{n_r+\frac{1}{2}} = \frac{(\varphi\rho)^{n+1}_{n_r} - (\varphi\rho)^{n}_{n_r}}{\Delta t} V_{b,n_r} \tag{A.25}$$

By using the same equations that gave A.18a), 20a), 22a) and 24a) A.25) becomes

$$T^{n}_{n_r-\frac{1}{2}}\left(P^{n+1}_{n_r-1} - P^{n+1}_{n_r}\right) - T^{n}_{n_r+\frac{1}{2}}\left(P^{n+1}_{n_r} - P_{Bound,o}\right) = \frac{\varphi(c_l + c_r)V_{b,n_r}}{\Delta t}\left(P^{n+1}_{n_r} - P^{n}_{n_r}\right) \tag{A.26a}$$

$$\begin{aligned} T^{n}_{n_r-\frac{1}{2}} P^{n+1}_{n_r-1} + P^{n+1}_{n_r}\left[-\left(T^{n}_{n_r-\frac{1}{2}} + T^{n}_{n_r+\frac{1}{2}} + \frac{\varphi(c_l + c_r)V_{b,n_r}}{\Delta t}\right)\right] \\ = -\frac{\varphi(c_l + c_r)V_{b,n_r}}{\Delta t} P^{n}_{n_r} - T_{n_r+\frac{1}{2}}{}^{n} P_{Bound,o} \end{aligned} \tag{A.26b}$$

Where $T_{n_r+\frac{1}{2}} = T_{b,bB}$ at boundary $i = n_r + \frac{1}{2}$ and $P_{Bound,o}$ is the external constant boundary pressure

**Matrix formulation**

The different combinations of boundary conditions are given in separate sections below.

As a general case, picture the matrix A.27a)

$$\begin{bmatrix} b_1 & c_1 & & & & 0 \\ & \ddots & \ddots & & & \\ & a_i & b_i & c_i & \ddots & \\ & & & \ddots & \ddots & c_{n_r-1} \\ 0 & & & & a_{n_r} & b_{n_r} \end{bmatrix} \begin{bmatrix} P^{n+1}_1 \\ \vdots \\ P^{n+1}_i \\ \vdots \\ P^{n+1}_{n_r} \end{bmatrix} = \begin{bmatrix} d_1 \\ \vdots \\ d_i \\ \vdots \\ d_{n_r} \end{bmatrix} \tag{A.27a}$$

Clearly, this is a matrix on the form

$$[A] \cdot \vec{P} = \vec{d} \quad \text{(A.27b)}$$

The method used for solving tri-diagonal matrices is Thomas algorithm (Aziz & Settari, 1979; Thomas, 1949)

The Thomas algorithm is a form of LU decomposition which relies on backwards elimination (Aziz & Settari, 1979; Ertekin et al., 2000; Lee, 2011). This algorithm yields coefficients $c_i'$ and $d_i'$ that are used for evaluating vector $\vec{P}$ and are given in equations A.28a) and b)

$$c_i' = \begin{Bmatrix} \dfrac{c_i}{b_i}; i = 1 \\ \dfrac{c_i}{b_i - a_i c'_{i-1}}; i = 2, 3, \dots, n_r - 1 \end{Bmatrix} \quad \text{(A.28a)}$$

$$d_i' = \begin{Bmatrix} \dfrac{d_i}{b_i}; i = 1 \\ \dfrac{d_i - a_i d_{i-1}'}{b_i - a_i c_{i-1}'}; i = 2,3,..,n_r \end{Bmatrix} \quad \text{(A.28b)}$$

The vector $\vec{P}$, i.e. $P_i^{n+1}$ is then obtained by back substitution, and given by:

$$P_{n_r}^{n+1} = d_{n_r}' \quad \text{(A.29a)}$$

$$P_i^{n+1} = d_i' - c'_i P_{i+1}^{n+1}\ ; i = n_r - 1, n_r - 2, \dots\dots, 1 \quad \text{(A.29b)}$$

This method is used for solving the matrix in all the cases below, given different boundary conditions.

***Constant rate inner boundary, constant rate outer boundary***

By combining equation derived in the previous section for the given boundary conditions, i.e. A.20b) and A.24b) the matrix solution takes the following form

$$\begin{bmatrix} -\left(T_{\frac{3}{2}}^n + \dfrac{\varphi(c_l + c_r)V_{b,1}}{\Delta t}\right) & T_{\frac{3}{2}}^n & & & 0 \\ & \ddots & \ddots & & \\ & T_{i-\frac{1}{2}}^n & -\left(T_{i-\frac{1}{2}}^n + T_{i+\frac{1}{2}}^n + \dfrac{\varphi(c_l + c_r)V_{b,i}}{\Delta t}\right) & T_{i+\frac{1}{2}}^n & \ddots & \\ & & \ddots & \ddots & \dfrac{G_{n_r-\frac{1}{2}}^n}{\mu B} \\ 0 & & & T_{n_r-\frac{1}{2}}^n & -\left(T_{n_r-\frac{1}{2}}^n + \dfrac{\varphi(c_l + c_r)V_{b,n_r}}{\Delta t}\right) \end{bmatrix} \begin{bmatrix} P_1 \\ \vdots \\ P_i \\ \vdots \\ P_{n_r} \end{bmatrix}^{n+1} = \begin{bmatrix} -(Q_{const} + \dfrac{\varphi(c_l + c_r)V_{b,1}}{\Delta t} P_1^n \\ \vdots \\ -\dfrac{\varphi(c_l + c_r)V_{b,i}}{\Delta t} P_i^n \\ \vdots \\ -\dfrac{\varphi(c_l + c_r)V_{b,n_r}}{\Delta t} P_{n_r}^n + Q_{out} \end{bmatrix} \quad \text{(A.30)}$$

For ease of calculation, this matrix may be written as:

$$\begin{bmatrix} b_1 & c_1 & & & & 0 \\ & \ddots & \ddots & & & \\ & a_i & b_i & c_i & \ddots & \\ & & & \ddots & \ddots & c_{n_r-1} \\ 0 & & & & a_{n_r} & b_{n_r} \end{bmatrix} \begin{bmatrix} P_1^{n+1} \\ \vdots \\ P_i^{n+1} \\ \vdots \\ P_{n_r}^{n+1} \end{bmatrix} = \begin{bmatrix} d_1 \\ \vdots \\ d_i \\ \vdots \\ d_{n_r} \end{bmatrix} \tag{A.27a}$$

And Thomas algorithm coefficients, c'i and d'i are given by:

$$c_i' = \begin{Bmatrix} \dfrac{c_i}{b_i}; i = 1 \\ \dfrac{c_i}{b_i - a_i c'_{i-1}}; i = 2, 3, \ldots, n_r - 1 \end{Bmatrix} \tag{A.31a}$$

$$d_i' = \begin{Bmatrix} \dfrac{d_i}{b_i}; i = 1 \\ \dfrac{d_i - a_i d'_{i-1}}{b_i - a_i c'_{i-1}}; i = 2,3,\ldots, n_r \end{Bmatrix} \tag{A.31b}$$

The vector $\vec{\mathrm{P}}$, i.e. $\mathrm{P}_\mathrm{i}^{\mathrm{n+1}}$ is then obtained by back substitution, and given by:

$$P_{n_r}^{n+1} = d'_{n_r} \tag{A.32a}$$

$$P_i^{n+1} = d'_i - c'_i P_{i+1}^{n+1} ; i = n_r - 1, n_r - 2, \ldots\ldots, 1 \tag{A.32b}$$

***Constant rate inner boundary, constant pressure outer boundary***

By combination of the giver boundary conditions, i.e. equations A.20b) and A.26b), the matrix takes the following form:

$$\begin{bmatrix} -\left(T^n_{\frac{3}{2}} + \dfrac{\varphi(c_l + c_r)V_{b,1}}{\Delta t}\right) & T^n_{\frac{3}{2}} & & & & 0 \\ & \ddots & \ddots & & & \\ & T^n_{i-\frac{1}{2}} & -\left(T^n_{i-\frac{1}{2}} + T^n_{i+\frac{1}{2}} + \dfrac{\varphi(c_l + c_r)V_{b,i}}{\Delta t}\right) & T^n_{i+\frac{1}{2}} & \ddots & \\ & & & \ddots & \ddots & T^n_{n_r-\frac{3}{2}} \\ 0 & & & & T^n_{n_r-\frac{1}{2}} & -\left(T^n_{n_r-\frac{1}{2}} + T^n_{n_r+\frac{1}{2}} + \dfrac{\varphi(c_l + c_r)V_{b,n_r}}{\Delta t}\right) \end{bmatrix} \begin{bmatrix} P_1 \\ \vdots \\ P_i \\ \vdots \\ P_{n_r} \end{bmatrix}^{n+1} = \begin{bmatrix} -\left(Q_{const} + \dfrac{\varphi(c_l + c_r)V_{b,1}}{\Delta t} P_1^n\right) \\ \vdots \\ -\dfrac{\varphi(c_l + c_r)V_{b,i}}{\Delta t} P_i^n \\ \vdots \\ -\dfrac{\varphi(c_l + c_r)V_{b,n_r}}{\Delta t} P_{n_r}^n - T^n_{n_r+\frac{1}{2}} P_{Bound,o} \end{bmatrix} \tag{A.33}$$

For ease of calculation, this matrix may be written on the form:

$$\begin{bmatrix} b_1 & c_1 & & & & 0 \\ & \ddots & \ddots & & & \\ & a_i & b_i & c_i & \ddots & \\ & & & \ddots & \ddots & c_{n_r-1} \\ 0 & & & & a_{n_r} & b_{n_r} \end{bmatrix} \begin{bmatrix} P_1^{n+1} \\ \vdots \\ P_i^{n+1} \\ \vdots \\ P_{n_r}^{n+1} \end{bmatrix} = \begin{bmatrix} d_1 \\ \vdots \\ d_i \\ \vdots \\ d_{n_r} \end{bmatrix} \tag{A.27a}$$

And Thomas algorithm coefficients, c'ᵢ and d'ᵢ are given by

$$c_i' = \begin{Bmatrix} \frac{c_i}{b_i}; i = 1 \\ \frac{c_i}{b_i - a_i c'_{i-1}}; i = 2, 3, \dots, n_r - 1 \end{Bmatrix} \tag{A.34a}$$

$$d_i' = \begin{Bmatrix} \frac{d_i}{b_i}; i = 1 \\ \frac{d_i - a_i d'_{i-1}}{b_i - a_i c'_{i-1}}; i = 2,3,..,n_r \end{Bmatrix} \tag{A.34b}$$

The vector $\vec{P}$, i.e. $P_i^{n+1}$ is then obtained by back substitution, and given by:

$$P_{n_r}^{n+1} = d'_{n_r} \tag{A.35a}$$

$$P_i^{n+1} = d_i' - c'_i P_{i+1}^{n+1}\ ; i = n_r - 2, n_r - 3, \dots\dots, 1 \tag{A.35b}$$

***Constant pressure inner boundary, constant pressure outer boundary Module3***

By combining the given boundary conditions, i.e. A.22b) and A.26b), the matrix takes the following form

$$\begin{bmatrix} -\left(T_{\frac{1}{2}}^n + T_{\frac{3}{2}}^n + \frac{\varphi(c_l + c_r)V_{b,1}}{\Delta t}\right) & T_{\frac{3}{2}}^n & & & & 0 \\ & \ddots & \ddots & & & \\ & T_{i-\frac{1}{2}}^n & -\left(T_{i-\frac{1}{2}}^n + T_{i+\frac{1}{2}}^n + \frac{\varphi(c_l + c_r)V_{b,i}}{\Delta t}\right) & T_{i+\frac{1}{2}}^n & \ddots & \\ & & & \ddots & \ddots & T_{n_r-\frac{3}{2}}^n \\ 0 & & & & T_{n_r-\frac{1}{2}}^n & -\left(T_{n_r-\frac{1}{2}}^n + T_{n_r+\frac{1}{2}}^n + \frac{\varphi(c_l + c_r)V_{b,n_r}}{\Delta t}\right) \end{bmatrix} \begin{bmatrix} P_1 \\ \vdots \\ P_i \\ \vdots \\ P_{n_r} \end{bmatrix}^{n+1} = \begin{bmatrix} -\left(T_{\frac{1}{2}}^n P_{Bound,i} + \frac{\varphi(c_l + c_r)V_{b,1}}{\Delta t} P_1^n\right) \\ \vdots \\ -\frac{\varphi(c_l + c_r)V_{b,i}}{\Delta t} P_i^n \\ \vdots \\ -\frac{\varphi(c_l + c_r)V_{b,n_r}}{\Delta t} P_{n_r}^n - T_{n_r+\frac{1}{2}}^n P_{Bound,o} \end{bmatrix} \tag{A.36}$$

For ease of calculation, this matrix may be written on the form:

$$\begin{bmatrix} b_1 & c_1 & & & & 0 \\ & \ddots & \ddots & & & \\ & a_i & b_i & c_i & \ddots & \\ & & & \ddots & \ddots & c_{n_r-1} \\ 0 & & & & a_{n_r} & b_{n_r} \end{bmatrix} \begin{bmatrix} P_1^{n+1} \\ \vdots \\ P_i^{n+1} \\ \vdots \\ P_{n_r}^{n+1} \end{bmatrix} = \begin{bmatrix} d_1 \\ \vdots \\ d_i \\ \vdots \\ d_{n_r} \end{bmatrix} \tag{A.27a}$$

And Thomas algorithm coefficients, c'ᵢ and d'ᵢ are given by

$$c_i' = \begin{Bmatrix} \frac{c_i}{b_i}; i = 1 \\ \frac{c_i}{b_i - a_i c'_{i-1}}; i = 2, 3, \dots, n_r - 1 \end{Bmatrix} \tag{A.37a}$$

$$d_i' = \begin{Bmatrix} \dfrac{d_i}{b_i}; i = 1 \\ \dfrac{d_i - a_i d_{i-1}'}{b_i - a_i c_{i-1}'}; i = 2, 3, .., n_r \end{Bmatrix} \tag{A.37b}$$

The vector $\vec{P}$, i.e. $P_i^{n+1}$ is then obtained by back substitution, and given by:

$$P_{n_r}^{n+1} = d_{n_r}' \tag{A.38a}$$

$$P_i^{n+1} = d_i' - c'_i P_{i+1}^{n+1} \; ; i = n_r - 1, n_r - 3, \ldots\ldots, 1 \tag{A.38b}$$

***Constant pressure inner boundary, constant rate outer boundary***

By combining the given boundary conditions, i.e. equations B21b) and B23b), the matrix takes the following form:

$$\begin{bmatrix} -\left(T_{\frac{1}{2}}^n + T_{\frac{3}{2}}^n + \dfrac{\varphi(c_l + c_r)V_{b,1}}{\Delta t}\right) & T_{\frac{3}{2}}^n & & & & 0 \\ \ddots & & \ddots & & & \\ T_{i-\frac{1}{2}}^n & -\left(T_{i-\frac{1}{2}}^n + T_{i+\frac{1}{2}}^n + \dfrac{\varphi(c_l + c_r)V_{b,i}}{\Delta t}\right) & T_{i+\frac{1}{2}}^n & \ddots & & \\ & & \ddots & \ddots & T_{n_r-\frac{3}{2}}^n & \\ 0 & & & T_{n_r-\frac{1}{2}}^n & -\left(T_{n_r-\frac{1}{2}}^n + \dfrac{\varphi(c_l + c_r)V_{b,n_r}}{\Delta t}\right) \end{bmatrix} \begin{bmatrix} P_1 \\ \vdots \\ P_i \\ \vdots \\ P_{n_r} \end{bmatrix}^{n+1}$$
$$= \begin{bmatrix} -\left(T_{\frac{1}{2}}^n P_{Bound,i} + \dfrac{\varphi(c_l + c_r)V_{b,1}}{\Delta t} P_1^n\right) \\ \vdots \\ -\dfrac{\varphi(c_l + c_r)V_{b,i}}{\Delta t} P_i^n \\ \vdots \\ -\dfrac{\varphi(c_l + c_r)V_{b,n_r}}{\Delta t} P_{n_r}^n + Q_{out} \end{bmatrix} \tag{A.39a}$$

For ease of calculation, this matrix may be written on the form:

$$\begin{bmatrix} b_2 & c_2 & & & & 0 \\ & \ddots & \ddots & & & \\ & a_i & b_i & c_i & \ddots & \\ & & & \ddots & \ddots & c_{n_r-1} \\ 0 & & & & a_{n_r} & b_{n_r} \end{bmatrix} \begin{bmatrix} P_2^{n+1} \\ \vdots \\ P_i^{n+1} \\ \vdots \\ P_{n_r}^{n+1} \end{bmatrix} = \begin{bmatrix} d_2 \\ \vdots \\ d_i \\ \vdots \\ d_{n_r} \end{bmatrix} \tag{A.27a}$$

And Thomas algorithm coefficients, $c'_i$ and $d'_i$ are given by

$$c_i' = \begin{Bmatrix} \dfrac{c_i}{b_i}; i = 1 \\ \dfrac{c_i}{b_i - a_i c'_{i-1}}; i = 2, 3, \ldots, n_r - 1 \end{Bmatrix} \tag{A.40a}$$

$$d_i' = \begin{Bmatrix} \dfrac{d_i}{b_i}; i = 1 \\ \dfrac{d_i - a_i d_{i-1}'}{b_i - a_i c_{i-1}'}; i = 2, 3, .., n_r \end{Bmatrix} \tag{A.40b}$$

The vector $\vec{P}$, i.e. $P_i^{n+1}$ is then obtained by back substitution, and given by:

$$P_{n_r}^{n+1} = d'_{n_r} \tag{A.41a}$$

$$P_i^{n+1} = d'_i - c'_i P_{i+1}^{n+1} \; ; i = n_r - 1, n_r - 2, \ldots\ldots, 1 \tag{A.41b}$$

An Excel macro was written for the 4 cases above. These are shown in Appendix C. The solution of $P_{\frac{1}{2}} = P_{Bound,i}$ and $P_{n_r+\frac{1}{2}} = P_{Bound,o}$ maintains a second order correct finite-difference flow equation (Abou-Kassem et al., 2006).

## Appendix B – Radial flow Excel macro

Below is the Excel macro written for the Settari et al. models of pressure-stress-permeability. The macro contains the required formulae for permeability models discussed in Section 2.7.2 and the radial model developed in Appendix A. The macro allows for several input boundary conditions, as discussed in Appendix A. As well, Excel sheet which is the basis of the macro allows for P(r,t) plots for pre-determined excel cells, as well as wellbore pressure derivative calculations. The part of the macro that changes between the different boundary conditions is noted as:

```
''''''''''''''''''''''''''''''''''''''''''''''''''''''''''''''''
''''''''''''''Thomas Algorithm''''''''''''''''''''
''''''''''''''''''''''''''''''''''''''''''''''''''''''''''''''''
```

Where parameters b(1), c(1), d(1), a(n_r), b(n_r) d(n_r) and d_mark(n_r) changes with changing boundary conditions. These parameters for the different combinations of boundary conditions are shown at the end of the Appendix.

```
Option Explicit 'require declaration of all variables

'Constant rate inner boundary, constant rate outer boundary


''''''''''''''''''''''''''''''''''''''''''''''''''''''''''''''''''''''''''''''''''''''''''''''''''''''''''''''
''''''''''''Parameter, vector, range, and counter variable definition''''''
''''''''''''''''''''''''''''''''''''''''''''''''''''''''''''''''''''''''''''''''''''''''''''''''''''''''''''''


Dim r_e As Double 'external radius
Dim r_w As Double 'well radius
Dim kunload As Double 'permeability
Public Const n_r As Double = 10 'number of grid blocks
Dim alphalg As Double ' for grid size calculations
Dim h As Double 'pay thickness in metres
Dim FVF As Double 'formation volume factor RV/SV
Dim PV_tot As Double ' total pore volume
Dim S As Double ' skin factor


Dim Qconst As Double 'constant rate inner condition
Dim Pinit As Double 'initial pressure
Dim P_avg As Double ' average pressure calculations
Dim P_avg0 As Double 'initial average pressure
Dim sig0 As Double 'initial stress
Dim sig_eff0 As Double ' initial effective stress
Dim Pobound As Double ' outer constant pressure boundary
Dim Pibound As Double ' inner constant pressure boundary
Dim Qout as Double ' outer constant rate boundary
```

```
Dim my_w As Double 'viscosity of water
Dim phi As Double 'porosity
Dim c_f As Double  'fluid compressibility
Dim c_r As Double 'rock compressibility
Dim c_t As Double 'total compressibility, as defined by scheme
Public Const Pi As Double = 3.14159265358979 'Pi


Dim total_t As Double 'total time, s
Dim Ntime As Double 'number of time steps
Dim dt As Double 'size of time step, delta t

Dim beta_c As Double 'for geometric factor calculations
Dim gamma As Double 'perm modulus
Dim eta As Double 'for permeability calculations, Poisson's ratio
Dim alphak As Double 'for permeability calculations, Biot constant

'defining dimensions of the vectors to be used; radii, pressure, permeability, G

Dim r(1 To n_r) As Double 'block centre radius
Dim r_minhalf(1 To n_r) As Double 'r_i-1/2
Dim r_plushalf(1 To n_r) As Double 'r_i+1/2
Dim P(1 To n_r) As Double 'Pressure
Dim k_old(1 To n_r) As Double 'permeability of prev. time step
Dim k(1 To n_r) As Double 'permeability at current time step
Dim P_old(1 To n_r) As Double 'Pressure at prev. time step
Dim V_b(1 To n_r) As Double 'Bulk volume of grid block
Dim G_minhalf(1 To n_r) As Double 'geometric factor at r_i-1/2
Dim G_plushalf(1 To n_r) As Double 'geometric factor at r_1+1/2
Dim sigeff_old(1 To n_r) As Double 'effective mean stress

'a, b, c, c_mark, d and d_mark for Thomas Algorithm calculations

Dim a(2 To n_r) As Double 'a(i)
Dim b(1 To n_r) As Double 'b(i)
Dim c(1 To n_r - 1) As Double 'c(i)
Dim c_mark(1 To n_r - 1) As Double 'c'(i)
Dim d(1 To n_r) As Double 'd(i)
Dim d_mark(1 To n_r) As Double 'd'(i)

'variables for loops
Dim i As Integer
Dim j As Integer
Dim m As Integer


Sub PressCalc()

Worksheets("BasicData").Activate

''''''''''''''''''''''''''''''''''''''''''''''''''''''''''''''''''''''''''''''''''''''''''''''''''''''''''''''''''''''''''''
''''''''''''''''''Input parameters from worksheet''''''''''''''''''''''''''''''''''''''''''''''''
''''''''''''''''''''''''''''''''''''''''''''''''''''''''''''''''''''''''''''''''''''''''''''''''''''''''''''''''''''''''''''
```

```
r_e = Range("C13").Value
r_w = Range("C4").Value
r_w = r_w * Exp(-S) 'effective wellbore radius because of skin
S = Range("C5").Value
kunload = Range("C14").Value * 0.987 * 10 ^ -15 ' permeability in mD*conversiton to m^2
alphalg = (r_e / r_w) ^ (1 / n_r)
h = Range("C15").Value
my_w = Range("C8").Value
phi = Range("C16").Value ' porosity
c_f = Range("C9").Value * 10 ^ -5 'compressibility in 1/bar * conversion to 1/Pa
c_r = Range("C17").Value * 10 ^ -5 '-------------||-------------------------------
c_t = Range("C18").Value * 10 ^ -5 '-------------||-------------------------------
total_t = Range("C22").Value * 86400 'conversion from day to sec
Ntime = Range("C23").Value
dt = Range("C24").Value * 84600 'conversion from day to sec
beta_c = 1
gamma = Range("C28").Value * 10 ^ -5 'conversion to 1/Pa
eta = Range("C29").Value
alphak = Range("C30").Value
Qconst = Range("C37").Value / 86400 'conversion to m^3/sec
Pinit = Range("C19").Value * 10 ^ 5 'conversion to Pa
sig0 = Range("C31").Value * 10 ^ 5 ' conversion to Pa
FVF = Range("C10").Value
Pobound = Range("C34").Value * 10 ^ 5 'conversion to Pa
Pibound = Range("C35").Value * 10 ^ 5 'conversion to Pa
P_avg0 = Pinit ' initial average pressure equal to reservoir pressure
Qout = Range("C36").Value / 86400 ' conversion to m3/D
PV_tot = (r_e ^ 2 - r_w ^ 2) * Pi * h * phi ' pore volume


''''''''''''''''''''''''''''''''''''''''''''''''''''''''''''''
'''''''''radius calculations''''''''''''
''''''''''''''''''''''''''''''''''''''''''''''''''''''''''''''

r(1) = (alphalg * Log(alphalg) / (alphalg - 1)) * r_w ' middle radius of block 1,
r_minhalf(1) = r_w 'r_i-1/2 i=1

For i = 2 To n_r
   r(i) = alphalg * r(i - 1) ' r_i
   r_minhalf(i) = (r(i) - r(i - 1)) / (Log(r(i) / r(i - 1))) 'r_i-1/2, log as natural log
Next i



For i = 1 To n_r – 1
   r_plushalf(i) = (r(i + 1) - r(i)) / Log(r(i + 1) / r(i)) 'r_i+1/2

Next i
   r_plushalf(n_r) = r_e 'last r_i+1/2 equals r_e


''''''''''''''''''''''''''''''''''''''''''''''''''''''''''''''''''''
''''''Bulk volume calculations''''''''''''
''''''''''''''''''''''''''''''''''''''''''''''''''''''''''''''''''''
```

```
    For i = 1 To n_r
      V_b(i) = (r_plushalf(i) ^ 2 - r_minhalf(i) ^ 2) * Pi * h
    Next i


    'to initially calculate pressure in all cells

    For i = 1 To n_r
          P_old(i) = Pinit
    Next i

P_avg = Pinit 'to specify initial average pressure = initial pressure


For j = 1 To Ntime


    ''''''''''''''''''''''''''''''''''''''''''''''''''''''''''''''''''''''''''''''''''''''''
    ''''''''Stress and permeability calculations/updates''''''''
    ''''''''''''''''''''''''''''''''''''''''''''''''''''''''''''''''''''''''''''''''''''''''

      For i = 1 To n_r

      'k_old(i) = kunload ' in case of not k(p)
      sigeff_old(i) = sig0 - alphak * P_old(i) 'ignoring stress change
      'sigeff_old(i) = sig0 + (2 / 3) * eta * ( P_old(i) - Pinit) - alphak * P_old(i) 'local model
      'sigeff_old(i) = sig0 + (2 / 3) * eta * (P_avg - P_avg0) - alphak * P_old(i) 'global model
      k_old(i) = kunload * Exp(-gamma * (sigeff_old(i) - (sig0 - Pinit))) 'in case of stress dependent permeability

    Next i
''''''''''''''''''''''''''''''''''''''''''''''''''''''''''''''''''''''''''''''''''''''''
''''''Interblock Geometric factor, transmissibility''''''''
''''''''''''''''''''''''''''''''''''''''''''''''''''''''''''''''''''''''''''''''''''''''

G_plushalf(1) = (beta_c * 2 * Pi) / (Log(r_plushalf(1) / r(1)) / (h * k_old(1)) + Log(r(2) / r_plushalf(1)) / (h * k_old(2)))
G_minhalf(1) = (beta_c * 2 * Pi) / (Log(r_w) / r(1)) ‘Geometric factor for inner pressure boundary

For i = 2 To n_r – 1
    G_minhalf(i) = (beta_c * 2 * Pi) / (Log(r(i) / r_minhalf(i)) / (h * k_old(i)) + Log(r_minhalf(i) / r(i - 1)) / (h * k_old(i - 1)))
    G_plushalf(i) = (beta_c * 2 * Pi) / (Log(r_plushalf(i) / r(i)) / (h * k_old(i)) + Log(r(i + 1) / r_plushalf(i)) / (h * k_old(i + 1)))

Next i
G_minhalf(n_r) = G_plushalf(n_r - 1)
G_plushalf(n_r) = (beta_c * 2 * Pi) / (Log(r(n_r) / r_e)) ‘Geometric factor for outer pressure boundary


Worksheets("Pressure calculations").Activate
```

```
''''''''''''''''''''''''''''''''''''''''''''''''''''''''''''''''''''''''''
''''''''''''''Thomas Algorithm''''''''''''''''''''''''
''''''''''''''''''''''''''''''''''''''''''''''''''''''''''''''''''''''''''

'Quantities of the matrix, A.P = d

   b(1) = -(G_plushalf(1) / (my_w * FVF) + (phi * c_t * V_b(1) / dt))
   c(1) = G_plushalf(1) / (my_w * FVF)
   d(1) = -(Qconst + ((phi * c_t * V_b(1)) / dt) * P_old(1))
   c_mark(1) = c(1) / b(1)
   d_mark(1) = d(1) / b(1)

   For i = 2 To n_r – 1
      a(i) = G_minhalf(i) / (my_w * FVF)
      b(i) = -(G_minhalf(i) / (my_w * FVF) + G_plushalf(i) / (my_w * FVF) + (phi * c_t * V_b(i)) / dt)
      c(i) = G_plushalf(i) / (my_w * FVF)
      d(i) = -(phi * c_t * V_b(i) * P_old(i)) / dt
      c_mark(i) = c(i) / (b(i) - a(i) * c_mark(i - 1))
      d_mark(i) = (d(i) - a(i) * d_mark(i - 1)) / (b(i) - a(i) * c_mark(i - 1))

   Next i

   a(n_r) = G_minhalf(n_r) / (my_w * FVF)
   b(n_r) = -(G_minhalf(n_r) / (my_w * FVF) + (phi * c_t * V_b(n_r)) / dt)
   d(n_r) = -(phi * c_t * V_b(n_r) * P_old(n_r)) / dt + Qout
   d_mark(n_r) = (d(n_r) - a(n_r) * d_mark(n_r - 1)) / (b(n_r) - a(n_r) * c_mark(n_r - 1))

   P(n_r) = d_mark(n_r)
   For i = n_r - 1 To 1 Step -1
         P(i) = d_mark(i) - c_mark(i) * P(i + 1)
   Next i

      Cells(1, 3 + j) = j * dt / 86400 ' writes time to excel sheet, in days

   For m = 1 To n_r
      Cells(2 + m, 3 + j) = P(m) / (100000) ' writes P in bar

   Next m
''''''''''''''''''''''''''''''''''''''''''''''''''''''''''''''''
'''''Average pressure calculation'''''''
''''''''''''''''''''''''''''''''''''''''''''''''''''''''''''''''

   P_avg = Application.WorksheetFunction.SumProduct(P, V_b) / Application.WorksheetFunction.Sum(V_b)

''''''''''''''''''''''''''''''''''''''''''''''''''''''''''''''''''''''''''''''''''''''''''''''''''''''''''
''''''''''''''BLOCK PERMEABILITY CALCULATION''''''''''''''''''''''
''''''''''''''''''''''''''''''''''''''''''''''''''''''''''''''''''''''''''''''''''''''''''''''''''''''''''

Worksheets("Permeability calculations").Activate
```

```
   For m = 1 To n_r
      Cells(3 + m, 2 + j) = k_old(m) / (0.987 * 10 ^ -15) ' Writes block permeability to sheet "Permeability calculation" in mD

   Next m
   Cells(1, 3 + j) = j * dt / 86400 ' writes time to excel sheet, in days


   ' Update P

      For i = 1 To n_r
         P_old(i) = P(i)
      Next i


Next j


'Reset P to initial pressure at the end of the simulation


For i = 1 To n_r
   P_old(i) = Pinit
Next i


Charts("Pwf").Activate


End Sub
```

***Other boundary conditions***

*'Constant rate inner boundary, constant pressure outer boundary*

```
   b(1) = -(G_plushalf(1) / (my_w * FVF) + (phi * c_t * V_b(1) / dt))
   c(1) = G_plushalf(1) / (my_w * FVF)
   d(1) = -(Qconst + ((phi * c_t * V_b(1)) / dt) * P_old(1))
   c_mark(1) = c(1) / b(1)
   d_mark(1) = d(1) / b(1)


   For i = 2 To n_r – 1
      a(i) = G_minhalf(i) / (my_w * FVF)
      b(i) = -(G_minhalf(i) / (my_w * FVF) + G_plushalf(i) / (my_w * FVF) + (phi * c_t * V_b(i)) / dt)
      c(i) = G_plushalf(i) / (my_w * FVF)
      d(i) = -(phi * c_t * V_b(i) * P_old(i)) / dt
      c_mark(i) = c(i) / (b(i) - a(i) * c_mark(i - 1))
```

```
    d_mark(i) = (d(i) - a(i) * d_mark(i - 1)) / (b(i) - a(i) * c_mark(i - 1))
  Next i


  a(n_r) = G_minhalf(n_r) / (my_w * FVF)
  b(n_r) = -(G_minhalf(n_r) / (my_w * FVF) + G_plushalf(n_r) / (my_w * FVF) + (phi * c_t * V_b(n_r)) / dt)
  d(n_r) = -(phi * c_t * V_b(n_r) * P_old(n_r)) / dt - G_plushalf(n_r) * Pobound / (my_w * FVF)
  d_mark(n_r) = (d(n_r) - a(n_r) * d_mark(n_r - 1)) / (b(n_r) - a(n_r) * c_mark(n_r - 1))


'Constant pressure inner boundary, constant pressure outer boundary

  b(1) = -(G_minhalf(1) / (my_w * FVF) + G_plushalf(1) / (my_w * FVF) + (phi * c_t * V_b(1) / dt))
  c(1) = G_plushalf(1) / (my_w * FVF)
  d(1) = -(G_minhalf(1) * Pibound / (my_w * FVF) + ((phi * c_t * V_b(1)) / dt) * P_old(1))
  c_mark(1) = c(1) / b(1)
  d_mark(1) = d(1) / b(1)


  For i = 2 To n_r – 1
    a(i) = G_minhalf(i) / (my_w * FVF)
    b(i) = -(G_minhalf(i) / (my_w * FVF) + G_plushalf(i) / (my_w * FVF) + (phi * c_t * V_b(i)) / dt)
    c(i) = G_plushalf(i) / (my_w * FVF)
    d(i) = -(phi * c_t * V_b(i) * P_old(i)) / dt
    c_mark(i) = c(i) / (b(i) - a(i) * c_mark(i - 1))
    d_mark(i) = (d(i) - a(i) * d_mark(i - 1)) / (b(i) - a(i) * c_mark(i - 1))
  Next i


  a(n_r) = G_minhalf(n_r) / (my_w * FVF)
  b(n_r) = -(G_minhalf(n_r) / (my_w * FVF) + G_plushalf(n_r) / (my_w * FVF) + (phi * c_t * V_b(n_r)) / dt)
  d(n_r) = -(phi * c_t * V_b(n_r) * P_old(n_r)) / dt - G_plushalf(n_r) * Pobound / (my_w * FVF)
  d_mark(n_r) = (d(n_r) - a(n_r) * d_mark(n_r - 1)) / (b(n_r) - a(n_r) * c_mark(n_r - 1))


'Constant pressure inner boundary, Constant rate outer boundary

  b(1) = -(G_minhalf(1) / (my_w * FVF) + G_plushalf(1) / (my_w * FVF) + (phi * c_t * V_b(1) / dt))
  c(1) = G_plushalf(1) / (my_w * FVF)
  d(1) = -(G_minhalf(1) * Pibound / (my_w * FVF) + ((phi * c_t * V_b(1)) / dt) * P_old(1))
  c_mark(1) = c(1) / b(1)
  d_mark(1) = d(1) / b(1)


  For i = 2 To n_r – 1
    a(i) = G_minhalf(i) / (my_w * FVF)
    b(i) = -(G_minhalf(i) / (my_w * FVF) + G_plushalf(i) / (my_w * FVF) + (phi * c_t * V_b(i)) / dt)
    c(i) = G_plushalf(i) / (my_w * FVF)
    d(i) = -(phi * c_t * V_b(i) * P_old(i)) / dt
    c_mark(i) = c(i) / (b(i) - a(i) * c_mark(i - 1))
    d_mark(i) = (d(i) - a(i) * d_mark(i - 1)) / (b(i) - a(i) * c_mark(i - 1))
  Next i
```

```
a(n_r) = G_minhalf(n_r) / (my_w * FVF)
b(n_r) = -(G_minhalf(n_r) / (my_w * FVF) + (phi * c_t * V_b(n_r)) / dt)
d(n_r) = -(phi * c_t * V_b(n_r) * P_old(n_r)) / dt + Qout
d_mark(n_r) = (d(n_r) - a(n_r) * d_mark(n_r - 1)) / (b(n_r) - a(n_r) * c_mark(n_r - 1))
```

## Appendix C – Eclipse verification model

The Eclipse model code below was provided by Anton Shchipanov , and edited by Eirik Brødremoen Lund for verification of the Implicit pressure solver made in this thesis. Pressure dependent permeability and constant pressure outer boundary options are added.

```
RUNSPEC

TITLE

Radial block model, Pressure dependent permeability


DIMENS
 10 1 1 /


RADIAL

METRIC

WATER


EQLDIMS
    1  100   20    1    1 /


TABDIMS
    1   1  40  40  1  40 /


WELLDIMS
    1   2    1    1 /


--In case of pressure dependent permeability
ROCKCOMP
  'REVERS' 2 /


START
   1 'JAN' 2017  /

UNIFOUT
UNIFIN
FMTOUT

GRID     ==============================================================

GRIDFILE
 2 /

INIT
```

```
OLDTRAN


-- RADIAL GRID DEFINED USING INRAD AND OUTRAD

--r_w = 0.1 m
INRAD
  0.1 /

--r_e = 100 m
OUTRAD
  100.0 /

DTHETAV
 1*360.0 /

DZ
 10*100/

TOPS
 10*1000.0 /

--perm 300 mD

PERMR
 10*300 /

PORO
 10*0.3  /

PERMZ
 10*300 /

EQUALS
  MULTPV
    1E+10 10 10 1 1 1 1 /
/

PROPS    ==============================================================

PVTW
-- Water PVT Properties
         200         1    2E-04       1         1*
/

DENSITY
-- Fluid Densities at Surface Conditions
         1*      1000         1*
/

--ROCK
----To be excluded when using ROCKTAB keyword
-- 200 3E-06
--/

REGIONS ==============================================================

--Which table to be used for pressure dependent permeability
```

```
ROCKNUM

10*1 /
--Table 1, Ignoring stress change

--10*2 /
--Table 2, local model

SOLUTION ==============================================================


PRESSURE
10*200

/

SUMMARY ===============================================================


RUNSUM

SEPARATE

FWIR

FWIT

FPR


WMCTL
 /
WBHP
 /
WBP9
 /
WPI
 /
WWIR
 /
WWIT
 /

BPR
1 1 1  /
/

SCHEDULE ==============================================================

RPTSCHED
 'RESTART=3' 'WELLS=5' 'SUMMARY=1'  'WELSPECS'   /

RPTRST
'BASIC=2' 'ALLPROPS'  'FLOWS=1'  /

-- WELL SPECIFICATION DATA
```

```
WELSPECS
 'INJ'  I  1  1  1*  'WATER'  /
/

COMPDAT
 'INJ'  1  1  1  1 'OPEN'  2*  0.2  1*   1* /
  /

WCONINJE
 'INJ' 'WATER' 'OPEN'  'RATE'  500 1* /
--in case of constant pressure inner boundary
-- 'INJ' 'WATER' 'OPEN'  'BHP' 2* 260 /
 /

----------------------------------------------

TSTEP
80*0.1125
/
```

## Appendix D – Dynamic fault simulation model

The Eclipse model below represents the simulation cases discussed in Chapter 4. This is the base case model for both closed faulted reservoir and the dynamic fault. Modifications were made to implement dynamic fault capabilities.

```
RUNSPEC     ======================

TITLE
   Dynamic fault model

DIMENS
    201    201    1  /

TABDIMS
    1   1  40  40  1  40 /

WATER

METRIC

WELLDIMS
    2    8    2   4 /

UNIFOUT

--in case of pressure dependent permeability

ROCKCOMP
 'REVERS' 2 /

START
   1 'MAR' 2017  /

GRID        ======================

INIT

DX
40401*10  /

--in case of dynamic fault:

DXV
--grid*size
  110*10 5.16 2.58 1.29 0.65 0.64 0.65 1.29 2.58 5.16 82*10 /

DY
  40401*10   /

DZ
  40401*100   /

PERMX
--blocks*perm mD
  40401*10 /

PERMY
  40401*10 /

PERMZ
  40401*10 /
```

```
PORO
  40401*0.3 /

TOPS
  40401*2000 /

--Introduce constant pressure boundary (MULTPV)

EQUALS
   MULTPV
     1E+10 1 1 1 201 1 1 /
/

RPTGRID
  /

PROPS    =========================

PVTW
--Pref  Bw      Cw   my_w
  200  1.00   4.0E-5   1 /

ROCK
--Pref  Cr
  200    3.0E-6   /

--to be deactivated when using ROCKTAB

DENSITY
--oil water gas
  1*  1013   1*  /

REGIONS    ===========================

--Dynamic fault permeability 100m east of injection, ROCKTAB table2

BOX
  114 115 51 151 1 1 /

ROCKNUM
202*2 /

SOLUTION    =============================

PRESSURE
40401*200
/

RPTSOL
  'RESTART=2' /

SUMMARY      ============================

EXCEL

FWPR

FWIR

FWCT
```

```
FGOR

FWPT

WBHP
'INJ1' /

SCHEDULE     ============================

RPTSCHED
 'RESTART=2' /

WELSPECS
 'INJ1'  I   101 101 1*  'WATER' /
  /

COMPDAT
  'INJ1'  0  0  1  1  'OPEN'  2*  0.2  /
  /

WCONINJE
  'INJ1' 'WATER' 'OPEN' 'RATE' 1000 /
  /

TSTEP
0.000622329 0.000774586 0.000964093 0.001199966
0.001493545 0.001858952 0.002313757 0.002879834
0.003584406 0.004461356 0.005552858 0.006911404
0.008602328 0.010706947 0.013326477 0.016586893
0.020644993 0.025695935 0.031982626 0.0398074 0.050029
35*0.05 0.1 20*0.3 90*0.1 39*0.1 180*0.05/

--log-increasing early time, and small time steps towards the end

WELSPECS
-- name group I J N/A Phase
 'INJ1'  I   101 101 1*  'WATER' /
  /

COMPDAT
  'INJ1'  0  0  1  1  'OPEN'  2*  0.2  /
  /
WCONINJE
  'INJ1' 'WATER' 'OPEN' 'RATE' 0 /
  /
TSTEP
0.000622329 0.000774586 0.000964093 0.001199966
0.001493545 0.001858952 0.002313757 0.002879834
0.003584406 0.004461356 0.005552858 0.006911404
0.008602328 0.010706947 0.013326477 0.016586893
0.020644993 0.025695935 0.031982626 0.0398074 0.050029
35*0.05 0.1 93*0.3 /


END
```